AN EXPERIMENTAL INVESTIGATION OF THE STRUCTURE OF REFLECTING, IONIZING SHOCKS IN XENON

Thesis by

Jerome Allan Smith

In Partial Fulfillment of the Requirements

For the Degree of

Doctor of Philosophy

California Institute of Technology

Pasadena, California

1967

(Submitted April 17, 1967)

ACKNOWLEDGMENTS

The author wishes to express his sincere appreciation to Professor Anatol Roshko for his guidance and encouragement during the course of this investigation. Dr. Donald Baganoff deserves special gratitude for his patient instruction in the construction and use of the pressure gauge employed in this investigation. The discussions with Professors H. W. Liepmann, B. Sturtevant, and D. Coles, particularly concerning the design of the GALCIT 6" shock tube, aided in the completion of this work, and their assistance is gratefully acknowledged.

Special thanks go to Mr. William Robinson for his aid in operating the shock tube and for his helpful suggestions made in the course of preparing the manuscript. Thanks also go to Mr. Lewis Balthasar for his help in the construction of the shock tube.

It is a pleasure to thank Mrs. Geraldine Krentler for typing the manuscript.

The author is indebted to the California Institute of Technology and the National Science Foundation for their financial assistance. The work in the GALCIT 6" shock tube was supported by the National Aeronautics and Space Administration.

ABSTRACT

The results of an experimental investigation of the reflection of strong shocks in xenon from the end wall of the GALCIT 6" shock tube are presented. The reflection of the incident shock structure, consisting of a frozen shock front, a region of relatively uniform frozen flow, and an ionization front, was observed with a fast-rise (0.3 μ sec) pressure gauge mounted in the shock tube end wall. The interaction between the reflecting shock and the ionizing gas in the incident shock structure was of particular interest. This interaction produces a complicated series of shock and rarefaction waves; those waves that propagate back to the end wall were observed with the pressure gauge. The incident shock Mach number was varied from 11 to 20, and the initial pressure was varied from 0.1 to 1.5 mm Hg.

A simple model which includes the gross features of the shock reflection process is used to calculate end wall pressures. The calculated pressures agree well with the experimental observations. In addition, ionization relaxation times for xenon behind the incident and reflected shocks are determined from this simple model and the measured pressure histories. The relaxation time data yield a better understanding of the ionization relaxation process in monatomic gases and provide an estimate for the electron-atom, inelastic excitation cross section for xenon.

TABLE OF CONTENTS

TABLE OF CONTENTS (contd.)

TABLE OF CONTENTS (contd.)

LIST OF FIGURES

LIST OF FIGURES (cont.)

I. INTRODUCTION

The ionization of a monatomic gas, uncomplicated by other internal degrees of freedom, represents one of the simplest reactions that one can observe and analyze in a shock tube. Previous investigators (Refs. 1, 2, 3, 4) have observed the ionization relaxation process behind the incident shock in order to better understand the ionization mechanism. Petschek and Byron (Ref. 1), using probes to measure the diffusion potential and photomultipliers to measure radiation intensity, and Wong and Bershader (Ref. 2), using an interferometer to measure electron and mass density profiles, have given a fairly complete understanding of the ionization relaxation process behind the incident shock in argon. The work reported in references 3, 4, and 5 involves a study of the initial phase of the relaxation process behind strong shocks in argon, krypton, and xenon. Other investigators (Refs. 6, 7, 8) have measured heat transfer to the end wall from ionized monatomic gases in the region behind the reflected shock.

In the present investigation a fast-rise pressure gauge similar to the one developed by Baganoff (Refs. 9, 10) is used to measure the time history of the <u>pressure</u> on the end wall behind reflected shocks in xenon. The shocks considered are of sufficient strength to produce relatively high equilibrium degrees of ionization ($\alpha \gtrsim .07$) behind

both the incident and reflected shocks. Of particular interest is the manner in which the reflected shock interacts with the ionizing gas behind the incident shock. This interaction produces a complicated wave pattern (a series of shocks and rarefaction waves); those waves which propagate to the end wall can be observed with the pressure gauge.

In this paper the term shock or shock structure denotes the transition region between one equilibrium state and another, i.e., including the region in which the internal degrees of freedom equilibrate. Later it will be useful to consider separately the part of the shock structure in which only the translational degrees of freedom are excited. This region is denoted by the term frozen shock front.

Before discussing the shock reflection process in ionizing monatomic gases (xenon in particular), it is useful to discuss briefly the shock reflection process in general. Schematic x-t (distance versus time) diagrams for the shock reflection process for different types of incident shock structure are shown in figure 1. The profile depicted on each x-t diagram corresponds, qualitatively, to the density variation for each type of shock structure. Figure 1a represents the simple x-t diagram for a shock propagating into an ideal, nonreacting gas. The incident and reflected shocks are idealized by discontinuities. If the initial

density (region 1) is decreased sufficiently, the thickness of the incident and reflected shocks is increased to the point where the shock structure can be observed experimentally. This case is depicted in figure 1b. Except for a distance of a few shock thicknesses in the vicinity of the end wall, the reflected shock propagates with constant velocity into a uniform gas, and the flow is described by the steady flow, shock jump equations for an ideal gas.

The density profile for the incident shock structure in figure 1c is typical of profiles observed for vibrationally relaxing polyatomic gases. (See the interferograms in reference 11, for example). The initial, discontinuous, density increase corresponds to that for a calorically perfect gas in which only the translational and rotational degrees of freedom are excited. The equilibration of the vibrational degrees of freedom produces the gradual or continuous density increase which follows. With respect to the mean free path in the undisturbed gas, the structure of this shock may be hundreds or thousands of mean free paths thick; whereas the frozen shock front, in which the translational and rotational degrees of freedom are excited, is only a few mean free paths thick. The shock reflection process is now much more complicated because the frozen reflected shock front must propagate into a nonuniform, chemically nonequilibrium gas. Since the gas properties

ahead of the reflected shock are changing in a continuous manner, this interaction between the reflected shock and the relaxing gas into which it propagates does not produce any discontinuous waves. (See, for example, the end wall pressure histories for vibrationally relaxing carbon-dioxide observed by Baganoff (Ref. 12).) In other words, the interaction proceeds smoothly and the reflected shock attains a constant velocity after a time that is of the order τ_{2vib}.

The density profile depicted in figure 1d corresponds to what one observes for strong shocks in monatomic gases such as argon and xenon. The interferometer measurements of Wong and Bershader (Ref. 2) show that the ionization relaxation part of the incident shock structure is characterized by a region of practically frozen flow (the properties of which are given by the equations for an ideal gas, $\gamma = 5/3$, since relatively little of the atoms' translational energy is expended in ion production) followed by a relatively thin region in which the gas goes quickly to equilibrium*. The latter region is denoted by the term ionization front**. The density profile in figure 1d is

* This behavior can also be inferred from the radiation measurements made by earlier investigators (Refs. 1, 13, 14), but it is most clearly shown by the measurements in reference 2.

** Camac and Feinberg (Ref. 7) were the first to use the term ionization front in their discussion of heat transfer measurements in argon.

shown as it appears in the experimental results of reference 2. Later it will be useful to treat this ionization front as a discontinuity.

The shock reflection process in this case (Fig. 1d) is quite different because the interaction between the reflected shock and the ionization front produces a series of finite amplitude waves, some of which propagate back to the end wall and can be observed by the pressure gauge. These waves are shown schematically in figure 1d and are labeled interaction waves. For incident shock Mach numbers greater than 13 in xenon, the density increases more across the ionization front than it does across the frozen shock front. To anticipate the nature of these interaction waves, we can see qualitatively that if the density increase across the ionization front were infinitely large, a shock would be reflected back toward the end wall. It then follows (e.g., from a pressure-velocity diagram) that a shock must be transmitted into the equilibrium gas in region 2e. These qualitative arguments appear very similar to those used in shock-shock interaction theory, but it will be shown later that the ionization front should not be treated as a shock front; it is simply part of the shock structure.

Although it is not indicated on the x-t diagram in figure 1d, this complicated interaction process must eventually decay. In other words, when viewed from infinity

(time), the shock reflection process in figure 1d must look qualitatively like the shock reflection depicted in figure 1b. Later, in section VII, it is shown that the interaction process is, for all practical purposes, complete at a time $\simeq 2\tau_{2ion}$ after the incident frozen shock reflection. In this respect the shock reflection processes in figures 1b, c, and d are similar in that, except for a distance of a few shock thicknesses in the vicinity of the end wall, the flow is described by the steady flow, shock jump equations. However, the relevant shock thickness is τ_{2vib} in figure 1c and τ_{2ion} in figure 1d.

This investigation does not represent the first attempt to describe the shock reflection process in ionizing monatomic gases. In their end wall measurements of heat transfer rates in argon, Camac and Feinberg (Refs. 6, 7) observed a second sharp increase in heat transfer after the one due to the frozen incident shock reflection. This second heat transfer increase occurred at a time approximately equal to τ_{2ion} (Fig. 1d). They postulated that the interaction between the reflected shock and the ionization front behind the incident shock creates a disturbance, probably a shock, which propagates back to the end wall with approximately the same velocity as the incident shock. However, they were not able to give any more details about the x-t diagram for the shock reflection process, nor were they able to assess from their measurements the strength of

the wave which produced the second heat transfer rate increase.

The end wall pressure gauge, on the other hand, can be used to measure the strength of the shock which results from the interaction. In addition, other waves which propagate to the end wall are observed with the pressure gauge, and the resulting pressure changes and arrival times (at the end wall) lead to a more complete understanding of the shock reflection process in highly ionized monatomic gases.

In the next two sections a description of the experimental technique (Sec. II) and some of the experimental results (Sec. III) appear. In the discussion of the experimental results it may be helpful to refer to the x-t diagram of the shock reflection process in figure 8. This x-t diagram has been deduced from the measured end wall pressure histories. The considerations involved in the construction of this x-t diagram are presented in sections IV and V.

II. DESCRIPTION OF THE EXPERIMENTAL TECHNIQUE

2.1 A Brief Description of the Shock Tube

A more complete description of this facility is contained in Appendix A. The features pertinent to this experiment are discussed here. The GALCIT 6" shock tube consists of a 6.02" I.D., stainless steel low pressure section, 37' in length, and a 6.5' long, 6.50" I.D., stainless steel driver section. Room temperature hydrogen was used as a driver gas to produce incident shock Mach numbers ranging from 10.9 to 20.5 in the xenon test gas. The initial pressure, P_1, of xenon was varied from 0.1 to 1.5 mm Hg; however the bulk of the experimental data was obtained at an initial pressure of 0.5 mm Hg.

In the course of a run, the driver was evacuated to 5 μ Hg with a Welch, Model 1397B, mechanical vacuum pump. The driven section was evacuated to approximately 5 μ Hg using either the Welch pump or a Kinney, Model KC46, pump. A liquid nitrogen cold trapped, oil diffusion pump was then used to evacuate the driven section to a pressure of 0.03 μ Hg. Normal procedure was to diffusion pump for half an hour. The initial combined leak rate and out-gassing rate after this amount of pumping was less than 3.0 μ Hg per hour. In order to minimize contamination, the test gas was introduced within seconds after the diffusion pump was closed off, and the run was completed a few minutes later.

2.2 Measurement of the Incident Shock Mach Number

The incident shock velocity was determined by observing the response of two platinum thin film heat transfer gauges. The platinum films, deposited on Pyrex plugs, were mounted flush with the shock tube wall at distances of 67.8 and 17.8 cm from the end wall. The port 17.8 cm from the end wall is shown in figure 3. The conventional method using a microsecond counter to measure the time interval for shock passage over the 50 cm distance was unsatisfactory because the gauge response was affected by the ionized gas behind the shock and the familiar precursor signal (Ref. 15) ahead of the shock. (The response of thin film gauges under conditions similar to those encountered in this investigation is described in detail in reference 16.)

Because of the uncertain triggering time, the output of these gauges was recorded with a Tektronix, Model 555, dual beam oscilloscope. One beam of the oscilloscope was triggered by the precursor signal from the upstream thin film gauge (67.8 cm from the end wall), the response of this gauge being recorded on this same beam. Triggering of the first beam activated a delay circuit in the oscilloscope; after the delay time had elapsed, the second beam, which recorded the output from the downstream gauge, was triggered. The delay time was carefully measured on a ten-megacycle counter before each run. Knowing the delay time,

the time interval for shock passage could be determined from the oscillograms. A conservative estimate of the error in determining the incident shock Mach number in this manner is $\pm$ 1%.

This uncertainty in the Mach number makes the comparison between some of the measured and predicted pressure levels more difficult since a 1% variation in Mach number produces a 2 to 3% variation in the predicted pressure levels.

2.3 Measurement of Initial Pressure P_1

Two calibrated volumes were used to fill the shock tube with the desired amount of xenon. One of these volumes is 0.005 times the volume of the shock tube. It was filled with xenon to a pressure 200 times greater than the desired initial pressure P_1. This larger pressure was read on a 0-50 mm Hg, bellows type Wallace and Tiernan gauge which had been calibrated with a McLeod gauge. For initial pressures of 0.5 mm Hg or more, a second volume 0.035 times the volume of the shock tube was used in the same manner. The error in determining the initial pressure was less than 1% for each run. This produces a 1% uncertainty in the end wall pressure measurements.

2.4 Description of the Pressure Gauge

The pressure gauge used to measure the pressure history on the end wall of the shock tube was a modified version of the type originally developed by Baganoff (Ref. 9). The principle of operation of the modified gauge is the same, but its performance is much better than Baganoff's original gauge. Basically the gauge consists of a capacitor which is placed on the front surface of a cylindrical elastic rod of Lucite. The dielectric material for the capacitor is usually Lexan, a polycarbonate plastic, which is similar to Lucite, but it has better high voltage characteristics and a lower modulus of elasticity, thus increasing its sensitivity over Lucite. (Refer to reference 9 for the theory of operation of the gauge.)

The modifications from which the present gauge resulted were made by Baganoff, while he was still at Caltech, with the author's assistance. The design of the gauge is depicted schematically in figure 2. The important feature to note is the three-electrode design which gives two capacitors in parallel and thus doubles the sensitivity of the gauge over the original two-electrode design (plate areas and spacing being equal). The plates of the capacitive sensing elements are made by grinding down a one inch diameter deposit of conducting epoxy to approximately one-half mil thickness. The conducting epoxy leads from the

outer two plates to ground are not shown in figure 2. The Lucite backing rod is 5 3/8" in diameter and when mounted in its stainless steel housing (Fig. 3) forms the end wall of the 6" shock tube.

It was found necessary to protect the capacitive sensing element of the gauge from small diaphragm particles which were released in the diaphragm bursting process. Occasionally these particles would penetrate the outer ground electrode and short out the capacitor. A .011 to .012" thick layer of Lexan cemented to the outer surface of the pressure gauge served to protect the gauge very well. Even though this protector plate was pitted and scarred in many places after 250 runs, the gauge continued to perform satisfactorily. (The pressure gauge had been used for 230 runs when the calibration oscillogram shown in figure 4 was obtained, and this oscillogram is exactly the same as one obtained just after the gauge was constructed.)

2.5 Calibration of the Pressure Gauge

The rise time and the sensitivity of the pressure gauge are determined by using a relatively high initial pressure, low Mach number run with nitrogen as the test gas. The pressure jump is assumed to be given by the Rankine-Hugoniot jump conditions. In this way a pressure-voltage conversion factor is obtained. Baganoff showed that this factor was a constant for various pressure jumps and various values of initial voltage on the gauge capacitor. This is also true for the present gauge. The shock wave at this condition is so thin (e.g., the incident shock front passes by a stationary observer in approximately 20 n sec) that it approximates a Heaviside function input to the gauge and cathode follower circuit. (This circuitry is discussed in more detail in Appendix B.) A typical response from such a run is shown in figure 4. The sensitivity of the gauge determined from this and other runs is 30.0 microvolts per mm Hg pressure jump for each kilovolt of charging voltage. A maximum of 6.5 kilovolts was used with the present gauge design, resulting in a maximum sensitivity of almost 0.2 millivolts per mm Hg.

The rise time of the gauge and circuit can also be found from figure 4. The rise time for this gauge is approximately 0.3 μ sec (0 to 95%). The notch in the trace behind the initial jump is associated with an acoustic

impedance mismatch between the protector plate and the outer ground electrode.

In the upper trace of figure 4, the end wall pressure history is undistorted for approximately 24 μ sec. This period is called the dwell time of the gauge. The disturbance which begins after 24 μ sec is due to stress waves propagating in from the radial boundary of the Lucite backing rod causing the gauge to "ring" (Ref. 9).

III. EXPERIMENTAL RESULTS

3.1 The Effect of the Ionized Gas on the Pressure Gauge

The ionized gas near the end wall had an effect on the response of the pressure gauge. An extreme example of this so-called "electrical effect" is shown in figure 5. The top and bottom curves are reproductions of oscillograms obtained from two runs with identical initial conditions and incident shock Mach numbers. The only difference between these two cases is that the pressure gauge charging voltage was negative for the upper curve (producing a positive voltage output) and positive for the lower curve. If the ionized gas had no effect on the pressure gauge, the lowest curve would simply be the mirror image about the time axis of the top curve.

Since the time to reach equilibrium behind the reflected shock is very long ($\geq$ 100 μ sec) compared to the time shown, no pressure variation due to ionization relaxation should be observed. However, there are electrons and ions present in relatively small quantities behind the frozen reflected shock front ($n_e \simeq 10^{10}$ cm^{-3}). If one assumes that the upper trace is the sum of two functions of time P(t) + E(t) (where P(t) represents the pressure and E(t) represents the "electrical effect") and the lower trace is -P(t) + E(t), subtracting the lower trace from the upper trace and dividing the result by two should yield the "net"

pressure history.

The "net" pressure history obtained in this manner is also shown in figure 5. For this condition the reflecting shock has an observable thickness of approximately 1 μ sec. This is followed by a slow rise in the end wall pressure due to the decay of the negative pressure perturbation resulting from heat transfer to the end wall. The latter effect has been discussed in detail in references 12 and 17. After a period of approximately ten shock thicknesses, the pressure approaches the asymptotic value which is equal to the Rankine-Hugoniot jump for an ideal gas ($\gamma = 5/3$), within the experimental accuracy. Thus, the assumption that the "electrical effect" can be considered as a linear combination with the pressure history is justified.

This is an extreme example because the "electrical effect" perturbed the actual pressure history by 40%. For the higher shock Mach numbers and higher initial pressures used in this investigation, the "electrical effect" perturbed the wall pressure history by approximately 10%. No appreciable variation of the absolute magnitude of the "electrical effect" perturbation was observed when the incident shock Mach number or the magnitude of the charging voltage was varied.

This procedure, requiring two runs with opposite charging voltage polarity for each condition was followed throughout. An alternative would have been to design a

gauge with two separate capacitive sensing elements. With each capacitor charged with a voltage of equal magnitude but of opposite polarity, a difference amplifier would give the "net" pressure history directly. Rather than undertake this extensive pressure gauge modification, it was decided to rely upon the repeatability of the shock tube. The repeatability of the incident shock Mach number was well within allowable limits, but the ionization relaxation time τ_2 behind the incident shock varied from run to run (at most $\pm$ 20%). It will be shown later that while this relaxation time is most important in determining the scale of the shock reflection process, its variation does not change the magnitude of any of the end wall pressures measured.

3.2 Typical Pressure History

The end wall pressure histories resulting from a pair of runs in xenon with an incident shock Mach number $M_s = 15.1$ and initial pressure $P_1 = 0.5$ mm Hg are shown in figure 6. The sweep speed in both oscillograms is the same, and time increases from left to right. The bright spots on the traces are 3.00 μ sec apart*. On the upper oscillogram, which corresponds to a negative charging voltage, various time intervals of interest are noted. These time intervals are discussed later in this and succeeding sections. On the lower oscillogram, which corresponds to a positive charging voltage, various pressure levels of interest are noted. On the upper oscillogram a pressure increase is upward and on the lower oscillogram increasing pressure is downward. (The "net" pressure history constructed from these two oscillograms appears next to the x-t diagram for the shock reflection process in figure 8.)

The first pressure rise is due to the frozen incident shock front reflecting from the end wall. It is followed by a slight pressure increase resulting from the decay of the heat transfer perturbation. Before an asymptote for this initial pressure rise (P_{5f}) can be reached, the

---

* See Appendix B for details regarding the technique of putting the timing marks on the oscillograms.

pressure begins to decrease slightly. This decrease is due to the ionization relaxation process behind the reflected shock. A minimum pressure (P_{5e}) is reached. (This is more apparent on the lower oscillogram since the "electrical effect" tends to mask this change in the upper one.) The time between the beginning of the frozen incident shock reflection and the minimum pressure point is defined as the ionization relaxation time τ_5' for xenon behind the reflected shock*. Other definitions might be appropriate, such as midway between the maximum of the first pressure rise (P_{5f}) and the minimum pressure point (P_{5e}), but none would define a point as easy to determine experimentally as with the definition chosen. (Choosing the mid-point would reduce the measured values of τ_5' by 10 to 30% over the range of conditions used in this investigation.) The minimum pressure point is also less easily distorted by the "electrical effect" than other defined points. Moreover, the minimum pressure point corresponds to the time at which the relaxation process is complete.

Following the relaxation to equilibrium behind the reflected shock, the pressure remains almost constant, increasing only slightly, for a time that is approximately two times τ_5'. Then, there is an abrupt pressure increase

* The relationship between the value of τ_5' observed on the end wall and the relaxation time τ_5 in the flow outside of the thermal layer is discussed in section 6.4.

($P_{5e} \rightarrow P_{6f}$) that is approximately twice the initial jump ($P_{5f} - P_1$). This pressure increase is the most interesting part of the end wall pressure history. Both the steepness and the magnitude of this pressure rise are remarkable. It arises from the interaction between the reflecting shock and the ionization front behind the frozen incident shock front (Fig. 1d). This interaction produces a weak shock that propagates back to the end wall. (This shock is weak in the sense that the pressure ratio P_{6f}/P_{5e} is approximately three.) Thus, the time τ_2' is related to the ionization relaxation time τ_2 behind the frozen incident shock front (Fig. 1d). τ_2' is defined as the time between the beginning of the first pressure rise and the mid-point of the second pressure rise.

Following the maximum pressure point (P_{6f}), the pressure decreases slightly to a constant level (P_{6e}). This is terminated by a sharper (though small) pressure decrease.

The other times τ_6' and t_1 on the upper oscillogram are explained in the next section.

3.3 A Series of Pressure Histories for P_1=const.=0.5 mm Hg

The results from a series of runs in which the initial conditions (pressure, temperature, and density) were kept constant while the Mach number was varied are shown in figure 7. All of these oscillograms have the same sweep speed and all correspond to a negative charging voltage on the pressure gauge. It is instructive to examine this series because the dependence on initial density in the relaxation phenomena has been removed. This means that the time scale changes on the complicated shock reflection process are due only to changes in temperature.

Various time intervals have been indicated on the oscillograms in figure 7. The first two time intervals marked (τ_5' and τ_2') correspond to the "relaxation times" discussed in the preceding section. As expected, these two time intervals decrease with increasing temperature (Mach number). A discussion of the relaxation time results appears in section 6.2. The third time indicated, τ_6', denotes the slight pressure decrease ($P_{6f} \rightarrow P_{6e}$) behind the maximum pressure point. The similarity between this pressure decrease and that due to the ionization relaxation behind the frozen reflected shock front ($P_{5f} \rightarrow P_{5e}$) implies that this may also be associated with a relaxation process. In the theoretical discussion that follows, the steep increase in pressure to the maximum pressure point (P_{6f})

is considered to be due to a shock wave reflecting from the end wall followed by an ionization relaxation process ($P_{6f} \rightarrow P_{6e}$). Thus τ_6' is considered to be a measure of the relaxation time behind this second reflecting shock; it can be observed to decrease as the Mach number increases. The fourth time interval, denoted by t_1, (visible on the lower three oscillograms only) indicates the arrival of a weak rarefaction pattern at the end wall. The values of t_1 and τ_2' taken from the oscillograms are used to construct the x-t diagram for the shock reflection process which is discussed in the next section.

IV. THE SHOCK REFLECTION PROCESS

Shock fronts in reacting gases are different from the ordinary gas dynamic shocks encountered in an ideal gas. In the first place, these shocks may be hundreds or thousands of mean free paths thick, as contrasted with shocks in ideal gases which are only a few mean free paths thick. The x-t diagram must describe, in effect, the reflection of a very thick shock from the end wall. Secondly, these shocks have an internal structure which consists of a relatively thin region in which the effects of viscosity and heat conduction are important (the frozen shock front) followed by a relatively thick region in which these effects may be neglected. The latter is where the internal degrees of freedom equilibrate with the translational and rotational degrees of freedom. Entropy is produced throughout the shock, first by heat conduction and viscous dissipation and then by the transfer of translational and rotational energy to the internal degrees of freedom.

The analysis of the shock reflection process is complicated by the fact that the reflected shock structure interacts with the relaxing gas behind the incident shock. Determining the changes in gas properties across the reflected shock is difficult because the flow is usually unsteady with respect to an observer stationed on the shock. Also the gas ahead of the shock is not in a state of

chemical equilibrium.

On the other hand, the peculiar nature of the ionization relaxation process in a monatomic gas like xenon creates an incident shock structure that can be thought of as being composed of two discontinuous fronts, a frozen shock front and an ionization front, with a density profile similar to that shown in figure 1d. With this simple model of the incident shock structure, it becomes possible to describe some of the details of the reflection process, which is not smoothly continuous as in the case of vibrationally relaxing structures (Fig. 1c). The method of analysis is similar to that used in shock-shock interaction theory. The purpose of the analysis is to determine the gross features of the shock reflection process and, in particular, to determine the pressures on the end wall in order to compare them with the experimental results.

4.1 The Structure of Strongly Ionizing Shocks in Monatomic Gases

The experimental results from Wong and Bershader's (Ref. 2) study in argon were discussed qualitatively in section I. Their interferometer measurements show that the ionization relaxation process has essentially two time scales. They also found that conditions immediately behind the frozen incident shock front are given by the shock jump equations for an ideal gas, $\gamma = 5/3$, (this is why we have called it a frozen shock front) and that the initial phase

of the relaxation process progresses very slowly toward equilibrium. During the first 75 to 80% of the total relaxation time, the electron number density increases to only 20% of its equilibrium value. This is accompanied by a proportional change in the measured mass density. Thus 80% of the change between the frozen conditions and the equilibrium conditions occurs during the remaining 20 to 25% of the total relaxation time. (The latter region, characterized by relatively steep gradients in gas properties, is denoted by the term ionization front (Refs. 6,7).)

As is the case for the experiments in reference 2, in the present investigation the incident shock is always of sufficient strength to produce a high equilibrium degree of ionization in the xenon test gas ($\alpha \geq .07$). Since the measured end wall pressure histories show a second large pressure increase ($P_{5e} \rightarrow P_{6f}$) after the one due to the frozen shock reflection, we conclude that an ionization front exists behind the incident shock for all cases of interest in the present investigation*, and that the

---

* This means that the ionization relaxation process is qualitatively the same in xenon as it is in argon. This similarity has been observed during the initial, atom-atom, collisional phase of the relaxation process (Refs. 3, 4). Furthermore, the similarity in the shock reflection process can be deduced from the qualitatively similar end wall heat transfer histories in argon (Refs. 6, 7) and xenon (Ref. 8).

interaction between this ionization front and the reflected shock produces the large pressure increase.

Thus, the model for the incident shock structure consists mainly of two simple elements, the frozen shock front and an ionization front, separated by a region of uniform frozen flow. This simplification is justified by the experimental results for argon (Ref. 2) and by a numerical analysis of the relaxing gas within the incident shock structure in xenon. The numerical analysis was made in connection with some of the relaxation times measured in this investigation. A full discussion of the relaxation time data and the numerical calculation appear later.

4.2 The Nature of an Ionization Front

The pressure is approximately constant, the density and particle velocity increase, and the atoms' and ions' translational energy decrease across the ionization front. Since the pressure is approximately constant across it, one might be tempted to treat the ionization front behind the incident frozen shock front as a contact discontinuity. But this is ruled out by the fact that the particle velocities are not the same on both sides and because it is stationary with respect to an observer on the frozen shock front. On the other hand, because the density and the particle velocity (momentum) increase across this front, one may be tempted to treat it as a strange type of shock wave in which there is a temperature decrease across the wave. If this were truly a wave, however, it would overtake the frozen shock front. It is, in fact, just part of the incident shock structure. However, it is useful to consider the ionization front as a discontinuity (Fig. 1d) for the purpose of analyzing the shock reflection process.

4.3 An x-t Diagram for the Shock Reflection Process in an Ionizing Monatomic Gas

Part of the x-t diagram for the shock reflection process in a highly ionized monatomic gas is shown qualitatively on the next page. From the considerations discussed at the end of section 4.1, the gas in region 2f is assumed to be completely frozen, and the gas in region 2e is assumed to be in equilibrium.

Initially, the frozen reflected shock front leaves the wall with the velocity $U_{R_{5f}}$, corresponding to that for an ideal gas. However, the lagging internal degrees of freedom of the gas act like a series of heat sinks distributed in the vicinity of the reflected shock ionization front. This heat sink distribution creates a rarefaction pattern*

---

* In Camac and Feinberg's papers (Refs. 6 and 7) reference is made to some unpublished work in which the reflected shock ionization front was assumed to be discontinuous. A simplified wave pattern, consisting of a centered expansion fan emanating from the end wall at $t = \tau_5$, was assumed to represent the wave pattern resulting from the ionization relaxation process. According to this model, deceleration of the frozen reflected shock front begins when the leading edge of the expansion fan overtakes the frozen shock front. If this model is used to calculate the earliest possible deceleration point for the conditions in the present investigation, this point is found to be further from the wall than the interaction point for the highest shock Mach numbers. (The interaction point lies within the dashed circle on the x-t diagram on the next page. Also, see figure 8.) In other words, our results imply that the deceleration occurs earlier than can be accounted for by a centered expansion fan emanating from the end wall at $t = \tau_5$. The procedure for determining the interaction point from the end wall pressure measurements is described later in this section and in section 3 of Appendix C.

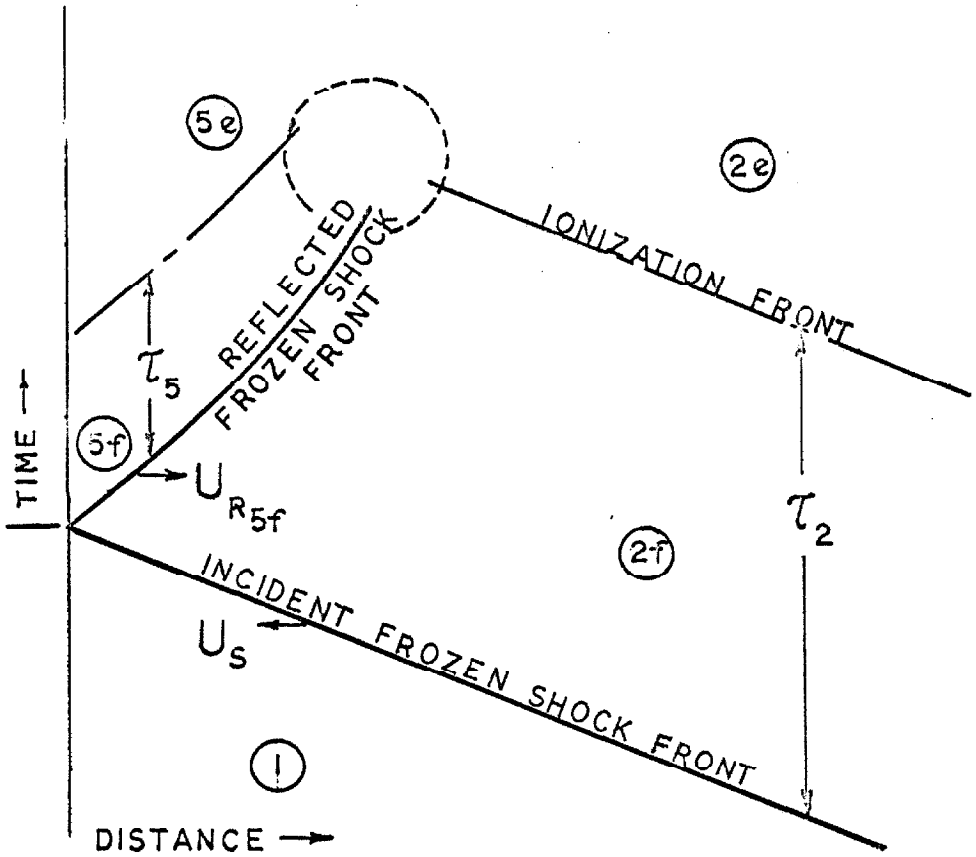

which overtakes the frozen reflected shock front, telling it to decelerate, and it reduces the pressure on the end wall ($P_{5f} \rightarrow P_{5e}$). This effect is not unlike that of the cold wall, except that in this case, the heat sink distribution extends out into the gas away from the end wall.

Thus, even though the gas behind the reflected shock ionization front is in chemical equilibrium, it is in a nonuniform region due to the fact that the gas has passed through a shock of varying strength. However, the degree of nonuniformity can not be too severe since the end wall

pressure histories show that the pressure is almost constant (for $\tau_5' < t < \tau_2'$), and the equilibrium temperature is a very weak function of the reflected shock velocity (e.g., the value of T_{5e} increases by only 25% when the frozen reflected shock speed, $U_{R_{5f}}$, is increased from 0.9 to 1.8 mm/μsec corresponding to a change in incident shock Mach number from 10 to 20). Therefore, in our simplified model, it is assumed that the gas behind the reflected shock ionization front is in a uniform condition. The largest error in this assumption is that the reflected shock structure does not attain its equilibrium velocity $U_{R_{5e}}$ until just before ($t \leqslant \tau_2$) it interacts with the incident shock ionization front. Nevertheless, for the reasons just given, the gas properties behind the reflected shock ionization front are given approximately by the equations listed in the next section (Eqs. (2)) corresponding to a reflected shock velocity $U_{R_{5e}}$.

The steep pressure rise to the maximum pressure point ($P_{5e} \rightarrow P_{6f}$) noted on the oscillograms in figures 6 and 7 implies that the interaction between the reflected shock and the incident shock ionization front produces a shock wave which propagates back to the end wall and reflects from it.

A complete x-t diagram for this process with the corresponding end wall pressure history is shown in figure 8. This corresponds to the experimental conditions used to

obtain the oscillograms in figure 6. In figure 8 the ionization fronts I_{2f-2e} and I_{5f-5e} and the interaction shock S_{5e-4e}* are depicted as discontinuities when, in fact, they are not. It is not possible to tell whether the finite width of the steep pressure rise in the experimental data is due to the thickness of the weak shock S_{5e-4e}**, the finite thickness of I_{2f-2e}, or a combination of the two. The oscillograms in figure 7 do show that the thickness of the steep pressure rise decreases as the incident shock Mach number is increased, but increasing Mach number should have the effect of reducing the thickness of both S_{5e-4e} and I_{2f-2e} so that no conclusion can be made.

The interaction occurring between the reflected shock structure S_{2f-5e} and the ionization front I_{2f-2e} is shown as occurring at a point (the interaction point) on figure 8; however, the ionization front and the reflected shock structure both have a significant thickness so that the interaction point is actually a diffuse interaction region

---

* In this and the discussion that follows, the symbols I and S denote an ionization front and a shock front, respectively. The subscripts refer to the regions ahead and behind the front. For example, I_{2f-2e} is the symbol for the incident shock ionization front, S_{1-2f} denotes the frozen incident shock front, and S_{2f-5e} is the symbol for the reflected shock structure which encompasses the frozen reflected shock front and the ionization front that follows.

** This shock is weak in the sense that the pressure ratio $P_{4e}/P_{5e} \lesssim 2.0$.

(the region indicated by the dashed circle in the x-t diagram on page 30). The interaction shock S_{5e-4e} and the transmitted shock S_{2e-3e} are assumed to emerge from this interaction region and propagate into regions 5e and 2e, respectively. For the purpose of determining the gross features of the shock reflection process, particularly for determining the pressures on the end wall, the details of this interaction are not important. Also, the details of this interaction can not be determined from the measured end wall pressure histories. (In figure 8 the ionization front behind the reflected frozen shock front is depicted as terminating on the line representing the trajectory of the shock S_{5e-4e}. This is just a schematic representation of what is actually taken to be part of the interaction region.)

Due to the fact that the temperature and electron number densities are high ahead of the shocks S_{5e-4e} and S_{2e-3e}, the gas in regions 3e and 4e is assumed to be in a uniform, equilibrium condition. There may be a small frozen region as part of the structure of these shocks, but for reasons which are discussed in section 6.7, the relaxation times must be very short ($\sim 0.1\ \mu$ sec).

The arrival time ($t = \tau_2'$) of the interaction shock S_{5e-4e} at the end wall is determined experimentally. Similarly, the measured pressure history gives the arrival

time ($t = \tau_2' + t_1$) of the leading edge of the rarefaction R_{6e-7}. Furthermore, these two times τ_2' and t_1, can not be derived from the simple theory developed in the following section, even if the velocities U_I, U_{IR}, u_{4e}, and a_{6e} can be calculated, because the simple theory does not give the trajectory of the reflected shock structure. Therefore, in order to construct the x-t diagram in figure 8 and determine the interaction point, it was necessary to use the experimentally determined values of τ_2' and t_1*.

One should also note that there are two different times τ_5' and τ_5 shown in figure 8. The time τ_5' is determined from the end wall pressure histories and denotes the beginning of the minimum pressure level P_{5e}; it is not the same as the "free stream" relaxation time τ_5. The presence of the end wall thermal layer has the effect of increasing the "relaxation times" observed on the end wall. τ_5 is the relaxation time for the gas outside of the thermal layer. The discussion of this effect on the measured values of τ_5' is taken up in section 6.4.

---

* In figure 6 one can see that τ_2' varied from run to run for the same initial conditions. This variation in τ_2' is discussed in section 6.3 in connection with the effect of impurities on the measured relaxation times. The scale of the entire x-t diagram for the shock reflection process (figure 8) is heavily dependent upon the magnitude of τ_2, but variations in τ_2 do not alter the magnitude of pressures observed on the end wall. The value τ_2' on the x-t diagram in figure 8 was chosen arbitrarily from the upper trace in figure 6.

The "relaxation time" τ_6' is also not the same as the "free stream" relaxation time τ_6 (not indicated in figure 8), but the relationship between these two times is difficult to determine since the nature of the thermal layer behind the shock S_{4e-6e} is not known.

V. A THEORETICAL MODEL

5.1 Calculating Conditions in Regions 2e, 3e, 4e, 5e, and 6e

Since the flow across the incident shock front can be assumed steady with respect to an observer stationed on the shock, the conditions in regions 2f and 2e may be obtained from the following equations in terms of the measured incident shock Mach number M_s (Ref. 18):

$$\frac{P_2}{P_1} = 1 + \gamma_1 M_s^2 \,(1 - 1/\eta) \qquad \text{a)}$$

$$\frac{h_2}{h_1} = 1 + \frac{(\gamma_1 - 1)}{2} M_s^2 \,(1 - 1/\eta^2) \qquad \text{b)} \qquad (1)$$

$$\frac{u_2}{a_1} = M_s \,(1 - 1/\eta) \qquad \text{c)}$$

$$\text{equation of state} \qquad \text{d)}$$

where P_1, h, u, γ_1, a_1 η are respectively the pressure, enthalpy, particle velocity, ratio of specific heats in region 1 (5/3), speed of sound in region 1, and the density ratio ρ_2/ρ_1. The conditions in region 2f, denoted by the subscript 2f, are given by equations (1) using the familiar equation of state for a perfect gas. Conditions in region 2e are given by equations (1) using the equation of state for the partially ionized, equilibrium gas (in the form of a Mollier diagram). Conditions for region 2f are tabulated in reference 19, and conditions in region 2e are

tabulated in reference 20.

Since the frozen reflected shock front is assumed to propagate initially with a constant velocity $U_{R_{5f}}$, conditions in region 5f may be determined from the ideal gas, steady flow, shock jump equations. In order to calculate conditions in region 5e, we have assumed that the reflected shock front attains its equilibrium velocity $U_{R_{5e}}$ before it interacts with the ionization front I_{2f-2e}. Region 5e can not, in fact, extend to the wall, but for the reasons outlined in the preceding section, it may be assumed to do so with relatively little resulting error in the predicted pressure and equilibrium temperature. With these assumptions the conditions in regions 5f and 5e can be determined from the following set of equations written as a function of the incident shock Mach number M_s (Ref. 18):

$$\frac{P_5}{P_1} = 1 + \gamma_1 M_s^2 \frac{(\eta_{2f} - 1)(\xi - 1)}{(\xi - \eta_{2f})} \qquad a)$$

$$\frac{h_5}{h_1} = 1 + (\gamma_1 - 1) M_s^2 \frac{(\eta_{2f} + 1)(\xi - 1)}{\eta_{2f}(\xi - \eta_{2f})} \qquad b) \qquad (2)$$

$$\frac{U_R}{a_1} = M_s \left(\frac{\eta_{2f} - 1}{\xi - \eta_{2f}}\right) \qquad c)$$

equation of state $\qquad d)$

where U_R, η_{2f}, and ξ are the reflected shock velocity, the density ratio ρ_{2f}/ρ_1, and the density ratio ρ_{5f}/ρ_1 or ρ_{5e}/ρ_1 (as the case may be) for the gas behind the reflected shock front. The equation of state for an ideal gas is used to compute P_{5f}, h_{5f}, $U_{R_{5f}}$, and ξ_{5f}. The equilibrium conditions P_{5e}, h_{5e}, ξ_{5e}, $U_{R_{5e}}$, etc., are found using a Mollier diagram* for equation (2d).

The procedure for calculating the conditions in regions 3e and 4e (refer to the x-t diagram in figure 8) is straightforward albeit tedious. A unique solution is supplied by the fact that the pressures and flow velocities on either side of the contact surface C_{3e-4e} are equal. The simplest way to describe this is to consider the pressure-velocity diagram shown in figure 9. The line labeled S_{5e-4e} represents the locus of all shocks propagating into region 5e with equilibrium conditions behind the shock. The line labeled S_{2e-3e} represents the locus for shocks propagating into region 2e. The point where these locii intersect determines the pressure and velocity in regions 3e and 4e. These locii may be computed from

* The Mollier diagram in reference 20 could have been used to calculate conditions in region 5e, but it was more convenient and accurate to use a Mollier diagram prepared at Aerospace Corporation since it had much smaller increments of temperature. This Mollier diagram was lent to the author through the courtesy of Dr. Alan F. Klein. By calculating conditions in region 2e and comparing them to the results in reference 20, it was concluded that there is no difference between the two Mollier diagrams.

the conservation equations and a Mollier diagram. The details of the equations used and the calculation procedure are presented in Appendix C.

5.2 Assumptions Concerning Region 6f

In the discussion of figure 7, it was observed that the pressure decrease ($P_{6f} \rightarrow P_{6e}$) just behind the maximum pressure point appeared in every way analogous to the pressure decrease behind the frozen reflected shock front ($P_{5f} \rightarrow P_{5e}$). On the other hand, for these conditions the relaxation time behind the shock S_{4e-6e} should be extremely small, and one should expect to see only the single pressure level P_{6e}. The most reasonable explanation for this is that the cold wall inhibits the relaxation process inside the thermal layer with the result that the gas first reaches equilibrium near the outer edge of the thermal layer. It then takes a finite time for the pressure signal resulting from the relaxation process in the "free stream" to propagate back through the thermal layer and be observed by the pressure gauge on the end wall.

An estimate of the pressure P_{6f} is obtained by making an analysis very similar to that made for the frozen incident shock front reflection, i.e., in a very small region near the end wall the flow is assumed frozen behind the reflected interaction shock. The only difference is that the reflected interaction shock is assumed to move into an equilibrium ionized gas (region 4e). The details of the assumptions made and the equations used to predict P_{6f} are found in Appendix C.

VI. COMPARISON OF THE EXPERIMENTAL AND THEORETICAL RESULTS

6.1 End Wall Pressures

The various end wall pressures in regions 5f, 5e, 6f, and 6e have been calculated using equations (1), (2), and the equations in Appendix C. A comparison of the theoretically predicted pressure levels and those observed experimentally is presented in figure 10. Since the pressure ratios P_{5e}/P_1, P_{6f}/P_1, and P_{6e}/P_1, are weak functions of the initial pressure, P_1, a constant initial pressure of 0.5 mm Hg was used for the theoretical and experimental values shown in this figure. The theoretical and experimental pressure levels for conditions at different initial pressures are summarized in Table I.

The measured values of P_{5f} are as much as 20% below the corresponding predicted values. This is due to heat transfer to the end wall, which produces a negative pressure perturbation. In order to help explain this apparent discrepancy, two different wall pressure histories have been sketched on the next page.

Case A represents a typical wall pressure history for an ideal or nonreacting gas in which the negative pressure perturbation due to heat transfer to the wall persists for a significant time. The time $t_{5\%}$ marked on this pressure history corresponds to the time at which the pressure perturbation has decayed to within 5% of P_{5f}. Baganoff,

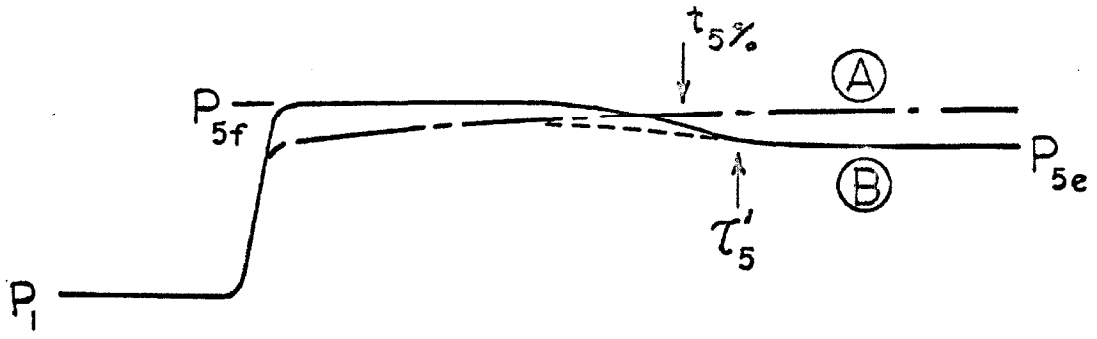

who proposed this definition, gives a convenient formula for computing $t_{5\%}$ in reference 12. He derived this formula from Goldsworthy's boundary layer theory for the end wall thermal layer (Ref. 17).

Trace B is what a wall pressure history for the case of ionizing xenon might look like with an adiabatic end wall. The pressure decrease, $P_{5f} \rightarrow P_{5e}$, results from the ionization relaxation process behind the frozen reflected shock front, reaching equilibrium at $t = \tau_5'$. (Case B also depicts what one would observe for $\tau_5' \gg t_{5\%}$ with a heat conducting wall.) For the conditions in this investigation, $t_{5\%}$ and τ_5' are of the same order of magnitude. Therefore, the beginning of curve A, the dashed line, and the end of curve B depict what is observed experimentally for most of the conditions used in this study in xenon.

Figure 11 shows a comparison between the "relaxation

times", τ_5', measured on the end wall and the time $t_{5\%}$ over a range of incident shock Mach numbers. The time $t_{5\%}$ is computed from Baganoff's (Ref. 12) formula assuming that the coefficient of thermal conductivity k_{5f} varies with the 3/4 power of the frozen temperature T_{5f}. It is clear from figure 11 that for the higher Mach numbers in this investigation, the ideal or frozen gas pressure jump, P_{5f}, will not be observed. On the other hand, for $M_s \lesssim 12.5$ the measured values of P_{5f} do agree with the predicted frozen values (Fig. 10).

Turning now to the equilibrium pressures, the observed values of P_{5e} agree with the theoretical predictions to within $\pm$ 10% for all cases except the two data points at $M_s = 14.0$. A conservative estimate of the uncertainty in the experimentally determined magnitudes of P_{5f} and P_{5e} is $\pm$ 7%. This estimate does not include the $\pm$ 1% uncertainty in the measured incident shock Mach number, M_s, which is noted separately in figure 10, but it does include consideration for the errors made in (1) measuring the initial pressure, (2) determining the calibration constant of the pressure gauge, and (3) measuring the amplitude of the pressure jump from the oscillograms.

The observed values of P_{6f} and P_{6e} (in figure 10 and Table I) are within 10% of the theoretical predictions, the majority of the experimental points lying slightly above the predicted values. The uncertainty in the measured values

is estimated to be less than $\pm$ 5%. The single data point for P_{6f} in figure 10 at $M_s = 13.5$ is more uncertain because it could not be ascertained whether the asymptotic value of P_{6f} had been reached within the dwell time of the pressure gauge. (See the top oscillogram in figure 7.) Also, the values of P_{6e} for the last three cases listed in Table I could not be determined experimentally because the rarefaction R_{6e-7} (see figure 8) arrived at the end wall before the pressure level P_{6e} was established. An example where this almost occurred may be seen in figure 7 for the case $M_s = 16.2$.

In view of the adequate agreement between the predicted and the observed end wall pressures, it may be concluded that the simple models for the ionizing shock structure and the interactions during reflection adequately describe the gross features of the phenomena observed.

6.2 Relaxation Time Data

The preponderance of relaxation time data obtained from shock tubes is the result of measurements made in the relaxation region of the incident shock structure (Refs. 1, 2, 13, 14). The present investigation offered the unique opportunity of measuring relaxation times behind the incident and reflected shock fronts simultaneously. This means that relaxation times are obtained for two different temperatures (and densities) in one experiment. This is made possible, on the one hand, by the measurement of the end wall pressure history, which is more directly related to wave phenomena than, say, temperature history; and on the other hand, by the discontinuous nature of the ionization relaxation process in monatomic gases (frozen region followed by an almost discontinuous ionization front) that permits one to distinguish the two relaxation times from one another. For the case of a continuous relaxation process such as the vibrational relaxation of carbon dioxide (Fig. 1c), Baganoff (Ref. 12) showed that the effects on the end wall pressure history due to relaxation in the incident shock structure can completely mask the effects due to relaxation in the reflected shock structure.

The relaxation times measured in the course of this investigation are shown in figure 12. The bulk of these data was obtained for an initial pressure of 0.5 mm Hg.

The data have been normalized with respect to initial density by multiplying the measured relaxation times by the initial pressure P_1 (in mm Hg). T_1 was nearly always the same ($300^{\circ}K$). The open symbols are values of the "relaxation time" τ_5' observed on the end wall. The solid symbols in figure 12 are the values of the time, τ_2, to reach equilibrium behind the incident shock in laboratory coordinates. The measured values of τ_2' have been used to calculate the relaxation time τ_2, using the equations from section 3 of Appendix C. (Refer to the x-t diagram in figure 8 for the qualitative relationship between τ_2' and τ_2.) For the range of incident shock Mach numbers considered here, τ_2 is approximately 85% of τ_2'.

The ionization relaxation time behind the incident shock in xenon has previously been measured by other investigators (Refs. 13, 14). The maximum incident shock Mach number in any of those investigations was 11.0, so that comparison is difficult. Our values of τ_2 at $M_s = 11.0$, shown in figure 12, are more than a factor of five larger than those reported in reference 13 and more than a factor of two larger than those reported by Turner (Ref. 14). In our investigation the frozen temperatures were varied over a wide range ($15{,}000^{\circ}\,K \leq T_{2f} \leq 37{,}500^{\circ}K$ and $27{,}500^{\circ}K \leq T_{5f} \leq 90{,}000^{\circ}K$). This is a much wider range of temperatures than has been previously reported.

Recently, another technique has been used to measure

relaxation times for xenon behind the incident shock in the GALCIT 6" shock tube. Klein (Ref. 16) used a photomultiplier tube to monitor the onset of radiation behind the frozen incident shock front. This technique has been shown to give the relaxation time in monatomic gases with fairly good accuracy (Ref. 1). Much of Klein's data was obtained on the same runs as the pressure gauge data shown in figure 12. A comparison between the present results for τ_2 and values measured by Klein for an initial pressure $P_1 = 0.5$ mm Hg is shown in figure 13. Also shown in figure 13 are a few relaxation times measured by the author using the same technique that Klein used. The close agreement between the relaxation times measured with a photomultiplier tube and those measured with the pressure gauge serves as further confirmation of the model for the shock reflection process proposed here. (See figure 8 and section 3 of Appendix C.)

6.3 The Effect of Impurities on the Measured Relaxation Times

The scatter in the data in figure 12 and in other results obtained by Klein (Ref. 16) (which are not shown in figure 13) indicate that impurities may affect the relaxation times measured. In using a photomultiplier to determine the onset of radiation behind the frozen incident shock front, Klein was not limited to a small observation time (cf., the 24 μ sec dwell time of the pressure gauge). As a result, he was able to obtain relaxation times over a wider range of initial pressures, particularly for $M_s \lesssim 15$. His data show an "impurity effect", i.e., at the lower incident shock Mach numbers, values of $P_1\tau_2$ for $P_1 = 0.1$ mm Hg are approximately half the values of $P_1\tau_2$ obtained at the same Mach number with $P_1 = 0.5$ mm Hg. Unfortunately, Klein did not measure relaxation times for initial pressures greater than 0.5 mm Hg so that no estimate of an upper bound for the relaxation time measured at any incident shock Mach number can be made from his data.

The relaxation times measured with the end wall pressure gauge in the 6" tube presented in figure 12 show a similar effect, although it is not nearly as pronounced because higher initial pressures and higher incident shock Mach numbers were used (in order that τ_2' be less than the dwell time of the pressure gauge). Note particularly the values of $P_1\tau_2$ for $M_s \simeq 16.0$ and 18.0. However, the fact

that the data points at $M_s \simeq 13.0$ for initial pressures of 1.0 and 1.5 mm Hg fall very close to a curve fitted through the P_1 = 0.5 mm Hg data points (see figure 18 which will be described later) suggests that the relaxation times measured for initial pressures of 0.5 mm Hg or more are independent of impurity effects in the 6" shock tube to within $\pm$ 30%.

The "impurity effect" is not nearly as evident in the measured values of $P_1\tau_5'$ shown in figure 12 because the scatter in the $P_1\tau_5'$ data is larger than it is in the $P_1\tau_2$ data. Two sources of the larger scatter in the $P_1\tau_5'$ data are the following: (1) τ_5' is obtained by locating a small pressure perturbation on the oscillograms. This perturbation (see figures 6 and 7) may be distorted by the "electrical effect" (Sec. 3.1) on the pressure gauge response. (2) Due to the necessity for a sweep speed slow enough to record the entire dwell time of the pressure gauge, some time resolution was sacrificed. A conservative estimate of the uncertainty in the values of τ_5' arising from lack of time resolution is $\pm$ 5%. Furthermore, in the next section it will be shown that the "relaxation time", τ_5', measured behind the frozen reflected shock front must be corrected for the effect of the end wall thermal layer, and this introduces additional uncertainty in these values, particularly for $M_s \geq 16.0$.

6.4 The Effect of the End Wall Thermal Layer

Since the end wall stays at essentially room temperature, a thermal boundary layer develops at the wall behind the reflected frozen shock front. The effect of the thermal layer has been discussed in connection with the end wall pressures measured (Sec. 6.1). Its presence has relatively little effect on the pressure, but, as will be shown, it can greatly affect the "relaxation time" τ_5' observed by the pressure gauge.

The cooler gas in the thermal layer does not ionize as rapidly as the gas that is not affected by the presence of the end wall. The pressure gauge does observe a pressure change associated with the relaxation process, but, since it takes a finite time for the sound wave, carrying the pressure change, to propagate through the thermal layer, there must be a time difference between the time that the gas first ionizes and when it is first observed on the end wall.

An x-t diagram of this phenomenon is shown in figure 14. This diagram was constructed by integrating Goldsworthy's similarity solution (Ref. 17). For this purpose the xenon (in region 5f) is assumed to be an ideal gas, and the coefficient of thermal conductivity, k_{5f}, is assumed to vary with the 3/4 power of the

frozen temperature T_{5f}*.

In figure 14 the line arriving at the end wall at $t = \tau_5'$ is the trajectory of a sound wave. The "relaxation time" that the pressure gauge sees is τ_5', but by following the trajectory of the sound wave to the edge of the thermal layer ($T/T_{5f} \simeq .99$), one can see that the actual relaxation time τ_5 may be considerably less than τ_5'. Therefore, all the experimental data should be reduced by an appropriate factor.

An uncertainty exists as to where, near the edge of the thermal layer, the gas ionizes first and produces the

---

* Goldsworthy's similarity solution is derived by assuming that the coefficient of thermal conductivity varies linearly with temperature in the thermal layer. The solution is then characterized by the thermal conductivity at the edge of the thermal layer. The assumption that the thermal conductivity is proportional to temperature is not a good representation of the actual behavior of xenon. Therefore, a more general assumption

$$k_{5f} = k_1 (T_{5f}/T_1)^{.75} ,$$

is used to calculate k_{5f} at the edge of the thermal layer. This value of k_{5f} is then used in the similarity solution to calculate the x-t diagram. The resulting inconsistency is minimized by the fact that over the largest part of the thermal layer the temperature changes are small. (In figure 14, for example, the temperature decreases by only 25%, from .99 to .74, over 75% of the thermal layer thickness.) Hence, it is more important, for present purposes, to determine accurately the thermal conductivity at the edge of the thermal layer than it is to get the proper behavior inside the thermal layer.

perturbation observed on the end wall. For example, the gas at the 90% temperature point (on the sound wave trajectory) could produce the negative pressure perturbation observed, for, even though the temperature is lower than the "free stream" value, the gas has been at a high temperature for a longer time than, say, the gas at the 99% temperature point. Added uncertainty in determining the proper reduction factor is introduced by lack of knowledge of the coefficient of thermal conductivity at these high temperatures and by the unknown effect of the very slightly ionized gas in region 2f on the relaxation process behind the reflected shock. It is also possible that Goldsworthy's boundary layer theory is not valid for times as short as these after shock reflection. Baganoff's results (Ref. 12) indicate that boundary layer theory correctly predicts the end wall pressure history beginning a few frozen shock front thicknesses after shock reflection, which are small times compared to the relaxation times here. On the other hand, the measurements of Sturtevant and Slachmuylders (Ref. 21) indicate that boundary layer theory does not predict the correct frozen reflected shock trajectory until times of the order $\frac{1}{2}\tau_5'$ have been exceeded; their measurements show that for these short times the reflected shock trajectory is closer to the adiabatic wall trajectory ($x = U_{R_{5f}} t$) than the trajectory calculated from

boundary layer theory. In any event, one can see from figure 14 that even if the adiabatic wall reflected shock trajectory were used, the error in determining the proper reduction factor for τ_5' would be less than 15%.

Therefore, a reasonable assumption which includes all these uncertainties in determining the proper reduction factor for the measured τ_5' data is to assume that the gas first ionizes somewhere between the 90% and 99% temperature points of the thermal layer. Corresponding estimates of the correction needed to determine the relaxation time behind the frozen reflected shock front from the measured values of τ_5' are plotted in figure 15*. The corrected values, τ_5, are shown in figure 16. The ends of the vertical lines correspond to the two curves in figure 15 and denote the uncertainty in the data due to the lack of knowledge of the proper reduction factor.

---

* An average curve drawn through the $P_1\tau_5'$ data in figure 12 was used to give a unique value of $P_1\tau_5'$ for each value of M_s.

6.5 Correlation of the Incident and Reflected Shock Relaxation Time Data

In the past the method used to predict relaxation times behind the reflected shock in monatomic gases was to find an empirical fit to relaxation time data obtained behind the incident shock and extrapolate to the higher temperatures found behind the reflected shock. The present data can be used to evaluate the best method of empirically fitting the incident shock relaxation time data in order to predict relaxation times behind the reflected shock in monatomic gases.

The simplest and most widely used technique (Refs. 6, 8) is to fit the available incident shock relaxation time data with a function of the form

$$P_1 \tau_2 = A \exp(T^*/T_{2f}). \qquad (3)$$

A and T* are constants determined from the fit to the experimental data. The functional form of (3) has been justified by the fact that all the experimental data obtained to date for argon (Refs. 1, 2) and xenon (Refs. 13, 14) fall on a straight line on a semilogarithmic plot of $P_1\tau_2$ versus $1/T_{2f}$. Then, the relaxation time behind the reflected shock is assumed to be given by

$$P_1\tau_5 = A(\rho_{2f}/\rho_1)(\rho_{2f}/\rho_{5f})\exp(T^*/T_{5f}) \qquad (4)$$

where the factor ρ_{2f}/ρ_1 converts τ_2 from laboratory time to

particle time (this assumption is discussed in more detail in the next section), and the factor ρ_{2f}/ρ_{5f} accounts for the increased density behind the frozen reflected shock front.

For the present $P_1\tau_2$ data, the values of $T^* = 65{,}200^{\circ}K$ and $A = .252$ mm Hg-μ sec were obtained by using the method of least squares to fit equation (3). The results of this fit and the corresponding prediction for $P_1\tau_5$, from equation (4) are shown in figure 17. The predicted values of $P_1\tau_5$ agree with the observed values for Mach numbers less than 15, but at $M_s \simeq 18$ the predicted values are a factor of two higher than the experimental ones.

In addition to the lack of agreement between the predicted and experimentally observed values of τ_5 obtained from equations (3) and (4), another disturbing fact is that the temperature T^* does not correspond to any characteristic temperature (or energy level) for the ionization process in xenon. This is also true of similar empirical fits to Petschek and Byron's (Ref. 1) relaxation time data for argon (see reference 8, for example). In an attempt to explain this lack of agreement at the very high temperatures and to resolve the question concerning T^* in equations (3) and (4), a numerical calculation of the incident shock relaxation process was undertaken. The numerical solution was based on theoretical considerations similar to those found in references 1 and 2. The assumptions made and the

details of the calculation procedure are described in Appendix D. From the results of the numerical solution, two aspects of the problem involved in extrapolating incident shock data to conditions behind the reflected shock can be examined (in the next two sections).

6.6 Conversion of Laboratory Time to Particle Time

The time to reach equilibrium behind the incident shock is measured with respect to a stationary observer (laboratory time). This is not the same as the time that an individual gas particle resides in the relaxation region. The relaxation time in coordinates moving with the particle is the physically significant time, so all the incident shock data must be converted from laboratory time to particle time before attempting to predict the relaxation times behind the reflected shock. This conversion is given by

$$\tau_{2_{particle}} = \int_0^{\tau_{2_{lab}}} \rho/\rho_1 \; dt_{lab} \; .$$

If region 2f is truly frozen (implying a discontinuous ionization front), the conversion is simply

$$\tau_{2_{particle}} = (\rho_{2f}/\rho_1) \; \tau_{2_{lab}} \; , \qquad (5)$$

since the conditions across the relaxation region are assumed constant. The numerical solution showed that $\tau_{2_{particle}}$ is underestimated by approximately 10% if one uses equation (5), due to the finite thickness of the ionization front* (P_1 = 1.0 mm.Hg; $12 \leq M_s \leq 20$).

---

* Wong and Bershader (Ref. 2) found that approximately the same error (10%) would be introduced by equation (5) for argon.

6.7 Temperature Dependence of the Relaxation Time

When extrapolating over such a wide range of temperatures, the question arises as to whether or not the simple temperature dependence in equations (3) and (4) is a good approximation. Moreover, one may question whether the atom temperature (T_{2f} and T_{5f}) is the correct temperature to characterize the relaxation process. In principle, one should be able to determine a characteristic time for the relaxation process from the ionization rate equations, and this should yield the correct form of the temperature dependence and the correct temperature to use. Therefore, in the discussion which follows, the dominant ionization mechanisms are examined, and the correct temperature and temperature dependence for the relaxation time is determined from the rate equations.

Ignoring impurities, the two major contributors to the production of electrons are collisions between atoms and collisions between electrons and atoms. A two-step ionization process (i.e., excitation to the first resonance state (8.5 ev), or metastable state (8.3 ev), followed by ionization, the excitation process assumed to be rate determining) during the atom-atom collisional phase of the relaxation process has been observed by Harwell and Jahn

(Ref. 3) and Kelly (Ref. 4)*. It is assumed that the two-step process is also dominant during the electron-atom collisional phase of the relaxation process. The average energy of the electrons ($\simeq$ 1 ev) is so low that this is probably a very good assumption.

Assuming that the atom-atom and electron-atom inelastic cross sections vary linearly with energy

$$(\sigma_{A-A})_{inel.} = B_{A-A}(E_A - E_m) \tag{6a}$$

$$(\sigma_{e-A})_{inel.} = B_{e-A}(E_e - E_m) \text{ ** }, \tag{6b}$$

the rates of electron production may be written as follows (Refs. 22, 1).

---

* From the measurements made to date (Refs. 3, 4, and 5), it is not possible to tell whether excitation to the long-lived metastable state, excitation to the lowest resonance state with subsequent radiation trapping, or a combination of the two is the dominant mechanism. Therefore, in the ensuing discussion (and Appendix D) the term "first resonance state" and "lowest metastable state" are used synonymously. The energy of the lowest metastable state, 8.3 ev, is used in the rate equations because the average of Kelly's data (Ref. 4) yielded this value. However, the energy of the first resonance state, 8.5 ev, is within his experimental uncertainty.

** Refer to Appendix D for the manner in which the values of the constants B_{A-A} and B_{e-A} have been determined. A brief discussion of the functional form of (6a) and (6b) is also found there.

$$\left[\frac{dn_e}{dt}\right]_{A-A} = 2\sqrt{\frac{E_m^3}{m_A \pi}}\; n_A^2\; B_{A-A}\; \frac{\left[\frac{E_m}{kT_A} + 2\right] \exp\left\{-\frac{E_m}{kT_A}\right\}}{\left[\frac{E_m}{kT_A}\right]^{3/2}} \qquad (7a)$$

$$\left[\frac{dn_e}{dt}\right]_{e-A} = 4 n_e n_A \sqrt{\frac{E_m^3}{2\pi m_e}}\; B_{e-A}\; \frac{\left[\frac{E_m}{kT_e} + 2\right] \exp\left\{-\frac{E_m}{kT_e}\right\}}{\left[\frac{E_m}{kT_e}\right]^{3/2}} \qquad (7b)$$

where E_m is the energy of the lowest metastable state, 8.3 ev, E_A is the energy of the atoms, E_e is the energy of the electrons. Also, n_A, T_A, m_A, n_e, T_e, m_e are the atom number density, temperature, and mass and electron number density, temperature and mass, respectively. The total rate of production is the sum of (7a) and (7b). Thus, an empirical fit of the form in equation (3) can be justified by the rate equations only if the atom-atom collision process is the dominant process over most of the total relaxation time, and if, in addition $E_m/kT_A \geq 7$. For the present conditions neither of these criteria is met. The numerical solution shows that the electron-atom process becomes dominant after 15-20% of the total relaxation time has elapsed. (Wong and Bershader (Ref. 2) found that the atom-atom process is dominant in the first third of the relaxation region for argon, but they used a

slightly different atom-atom inelastic cross section.) Hence, if any characteristic time is to be obtained from the rate equations, equation (7b) rather than (7a) should be used, and so the temperature to use should be that of the electrons and not the atoms and ions.

If we assume that the electron temperature, T_e, and the atom number density, n_A, are constant in the relaxation region, we can obtain a characteristic time from the rate equation (7b). (The numerical solution shows that this is a very good assumption.) Equation (7b) may be written

$$\frac{dn_e}{n_e} \sim n_A \frac{\left(\frac{E_m}{kT_e} + 2\right) \exp\left(-\frac{E_m}{kT_e}\right)}{\left(\frac{E_m}{kT_e}\right)^{3/2}}$$

or

$$n_e \sim \exp\,(t/\tau)\ , \tag{8}$$

where

$$\tau \sim \frac{\left(\frac{E_m}{kT_e}\right)^{3/2} \exp\left(\frac{E_m}{kT_e}\right)}{n_A \left(\frac{E_m}{kT_e} + 2\right)}\ . \tag{9}$$

Since

$$n_A \simeq n_{A_{2f}} = (\rho_{2f}/\rho_1) n_1 \simeq 4P_1/kT_1 = \text{const. } P_1, \tag{10}$$

$$P_1\tau_2 = \frac{A\left(\frac{E_m}{kT_e}\right)^{3/2} \exp\left(\frac{E_m}{kT_e}\right)}{\left(\frac{E_m}{kT_e} + 2\right)} , \qquad (11)$$

where A is a constant determined from the experimental data.

In practice, fitting the data with a function of this form is somewhat undesirable since the determination of the electron temperature, T_e, is a very complicated calculation and requires knowledge of the inelastic, electron-atom cross section. However, the equilibrium temperature, T_{2e}, is approximately equal to the electron temperature behind the frozen incident shock front. (This is best seen in figure 26 where the calculated atom and electron temperatures are plotted as functions of time behind the incident frozen shock front.) Therefore, the equilibrium temperatures T_{2e} and T_{5e} can be used instead of the electron temperature in the relaxation time equations.

The use of the equilibrium temperatures introduces an undesirable initial pressure dependence into consideration. (T_{2e} and T_{5e} are weak functions of initial pressure.) Since the bulk of these data was obtained for P_1 = 0.5 mm Hg, no conclusion about this initial pressure dependence can be ascertained. Furthermore, it is probably smaller than the effect of impurities. The values of T_{2e} and T_{5e} used here are for P_1 = 0.5 mm Hg.

The constant A in equation (11) was determined from the measured values of τ_2 ($A = 6.15 \times 10^{-5}$ mm Hg-μ sec). The equation

$$P_1\tau_5 = (1.1)\left(\frac{\rho_{2f}}{\rho_1}\right)\left(\frac{\rho_{2f}}{\rho_{5f}}\right)\frac{A\left(\frac{E_m}{kT_{5e}}\right)^{3/2}\exp\left(\frac{E_m}{kT_e}\right)}{\left(\frac{E_m}{kT_e}+2\right)} \qquad (12)$$

was then used to predict the values of $P_1\tau_5$. The factor 1.1 has been added to equation (12) for the laboratory-to-particle time conversion discussed in section 6.6 (This factor is derived from the numerical solution and is <u>not</u> an empirical correction.) A comparison between the experimental results for $P_1\tau_5$ and those predicted by equation (12) is shown in figure 18. The agreement for this fit over the entire range of incident shock Mach numbers is much better than that obtained with equations (3) and (4) (see figure 17). Equations (11) and (12) have the added advantage that only one unknown constant needs to be determined from the experimental data. Therefore, this method of using the electron (equilibrium) temperature provides the most self-consistent and accurate method of predicting, from incident shock data, the relaxation times for the higher temperatures behind the reflected shock. This procedure may not be as successful for argon since the atom-atom electron production is dominant for a greater

portion of the total relaxation time; but the electron temperature and atom number density are almost constant (Ref. 2) so that the assumptions made in deriving equations (11) and (12) still hold.

VII. THE SHOCK REFLECTION PROCESS FOR TIMES LARGER THAN THE RELAXATION TIME τ_2

Ultimately, the reflected shock must recede from the wall with a constant velocity $U_{R\infty}$ leaving a region with uniform particle velocity, $u = 0$, and pressure, $P = P_{R\infty}$, behind. $U_{R\infty}$ and $P_{R\infty}$ can be calculated from equations (2) by replacing η_{2f} with $\eta_{2e} = \rho_{2e}/\rho_1$. This condition is approached only asymptotically, but, for all practical purposes, the reflection process should be complete within a few shock thicknesses. (See, for example, the x-t diagrams sketched in figures 1b and 1c.)

For the present shock reflection process, we can, in principle, extend the calculation on the pressure-velocity diagram for the various interactions in order to determine if, indeed, the shock reflection process is complete within a few shock thicknesses. On the next page an x-t diagram and a pressure-velocity diagram of the reflection process are sketched for times greater than τ_2.

It is difficult to calculate the locus of R_{6e-7} on the pressure-velocity diagram because this expansion fan propagates into an equilibrium ionized gas. However, we note from the oscillograms at the bottom of figure 7 that the pressure change across R_{6e-7} is small ($\sim 10\%$) so that we know the approximate location of the point 7, 8e on the pressure-velocity diagram, i.e., $P = .9P_{6e}$, $u \leqslant 0$.

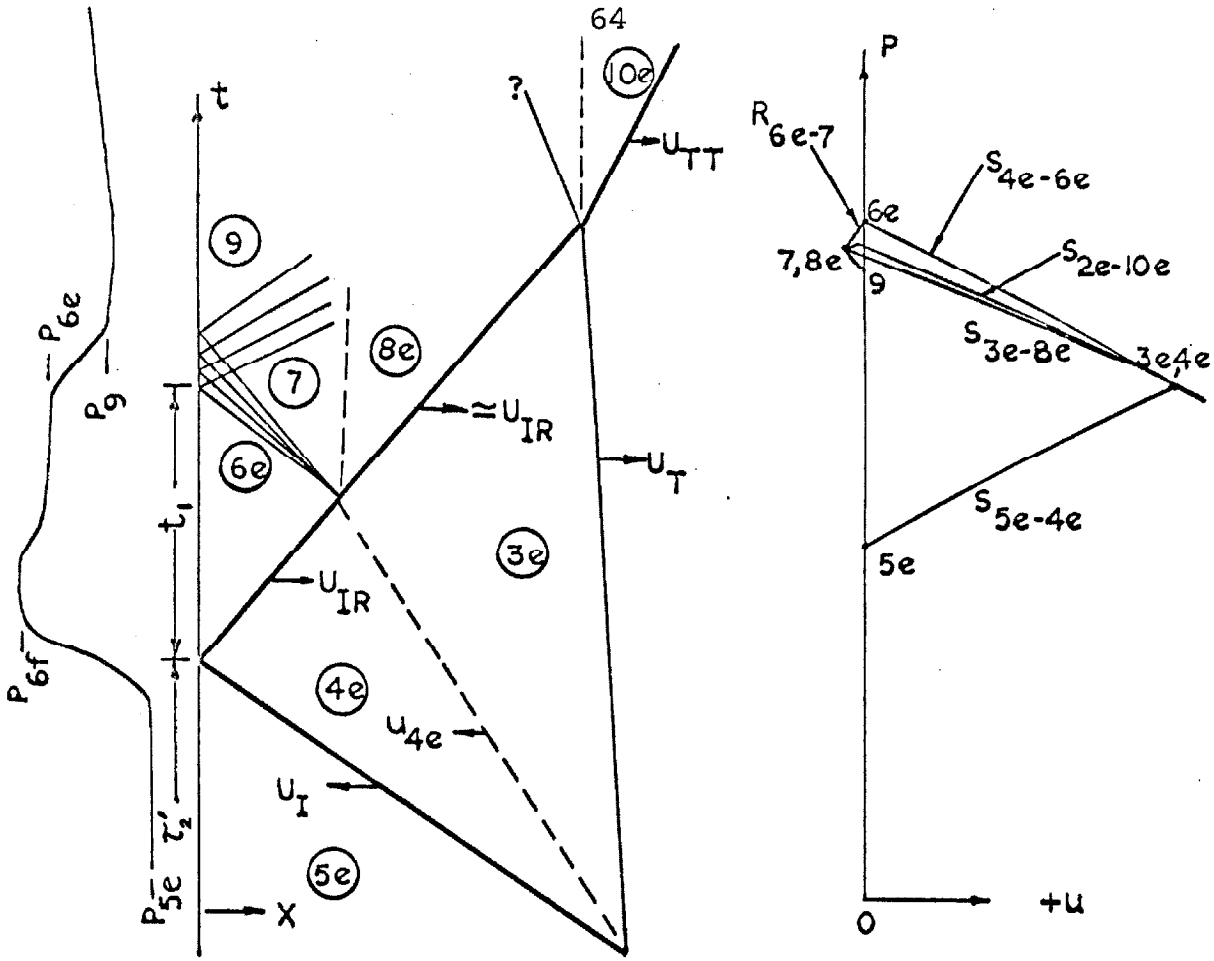

Furthermore, this implies that the velocity of S_{3e-8e} is approximately equal to U_{IR}. From the x-t diagram we can see that this means that S_{3e-8e} overtakes S_{2e-3e} at the time $t \simeq 2\tau_2$.

The interaction between S_{3e-8e} and S_{2e-3e} produces a shock (S_{2e-10e}) which propagates into region 2e with velocity U_{TT} (moving away from the wall). On the pressure-velocity diagram it is difficult to determine whether the locus for S_{2e-3e} lies above or below the locus for S_{3e-8e}. (The difference between these two locii on the pressure-velocity diagram is less than the errors accumulated in making the

"real" gas calculations for regions 2e, 3e, 4e, 5e, and 6e, i.e., 1 to 2%.) If S_{2e-3e} lies above S_{3e-8e}, as it is shown in the above sketch, a very weak shock propagates into region 8e. On the other hand, if S_{2e-3e} lies below S_{3e-8e}, a very weak rarefaction propagates into region 8e. In either case, the wave propagating into region 8e, resulting from this interaction, is so weak that the particle velocity, u_{10e}, is approximately zero, and with $u_{10e} \simeq 0$, $U_{TT} \simeq U_{R\infty}$ and $P_{10e} \simeq P_{R\infty}$. The shock reflection process is then, for all practical purposes, complete at the time $t \simeq 2\tau_2$, or, in other words, it is complete after a time approximately equal to two incident shock thicknesses has elapsed.

In the discussion of figure 7, the pressure level P_9 (at $t \geq \tau_2' + t_1$) was not mentioned. It turns out that for all the cases in which P_9 was observed, $P_9 \simeq P_{R\infty}$ (within experimental error, $\pm$ 5%). It may be that this is already the equilibrium pressure $P_{R\infty}$. On the other hand, this may be coincidence since there is a further rise in pressure, after P_9, indicated by the pressure gauge. This pressure rise seems too large to be the result of further interaction, since the strength of successive interactions tends to cascade downward (approaching the point $P = P_{R\infty}$, $u = 0$ on the pressure velocity diagram). It is not possible to settle this question by calculation from our simplified

model because the effects are small and hardly bigger than the accumulated error.

In any case, it is clear that the shock S_{2e-10e} has approximately the asymptotic velocity $U_{R\infty}$ by the time $t \geq 2\tau_2$ and that all the other waves are very weak, indeed.

APPENDIX A

THE GALCIT 6" SHOCK TUBE

The GALCIT 6" shock tube is designed to complement the performance of the GALCIT 17" shock tube (Ref. 23). The 6" tube retains the simplicity and repeatability of a cold gas driver, but with the addition of hydrogen to the possible driver gases used, much higher shock Mach numbers may be achieved in the 6" facility.

The shock tube was designed with a view toward investigating various reaction rate phenomena, producing highly ionized plasmas, and studying radiation effects. The following incident shock Mach numbers have been achieved for some representative test gases at an initial pressure of 0.1 mm Hg, with a hydrogen driver:

xenon	$M_s = 20.5$
nitrogen	$M_s = 13.0$
argon	$M_s = 14.0$

(The condition listed for xenon yields a slug of test gas that is approximately 15 cm in length at the end wall of the shock tube. The relaxation region is approximately 0.7 cm long, and the equilibrium degree of ionization is 0.50. The cost for a run in xenon at an initial pressure of 0.1 mm Hg, including diaphragm, driver gas, and test gas is less than $2.00.)

The basic dimensions, vacuum characteristics, and controls for the 6" shock tube are described in the following discussion. Also, a detailed description of the method used to clamp two tube sections together and the method used to clamp the diaphragm is given. These two design features are unique and represent an improvement over previous designs in that they are simpler and more economical in construction and use.

A.1 Description of the Basic Tube

The GALCIT 6" shock tube consists of a conventional cold-gas driver section, a diaphragm-transition section assembly, and a 36' long driven (test) section. The entire assembly is suspended from a central "H" beam which in turn is supported by a series of five inverted "U" frames of welded "I" beam construction bolted to the floor. The centerline of the shock tube is approximately 6.5' above the floor leaving the space below available for pumps, control panel, oscilloscopes, work benches, and other equipment.

The tube is suspended at 6' intervals from the main "H" beam with a commercially available pipe clevis assembly which is relatively inexpensive. A typical clevis assembly is shown in figure 19. The entire tube may be completely assembled by two men with the aid of a quarter-ton hoist in a few hours.

The basic driver tube is a 6' long piece of 6.520" I.D., type 321 stainless steel, seamless tubing with a wall thickness of 0.5". Connected to this is a 10" long transition section. (The transition section is described in detail later in connection with the diaphragm clamping mechanism.) The driver section assembly has been hydraulically tested to a pressure of 2200 psig without failure of seals or joints.

A picture of the driver section assembly is shown in figure 20. The driver tube is suspended from the central "H" beam on movable trolleys so that when changing diaphragms the entire driver is rolled back. The hydraulic pump visible in the figure (suspended from the driver tube) is described later.

The driver vacuum pump line, the pressure gauge line for monitoring the driver pressure, and the driver gas inlet and exhaust lines are connected to the driver end wall by means of flexible metal tubing. The driver (or after a run has been made, the entire tube) may be vented to the atmosphere by a line which runs from the driver end wall through the roof of the building. When hydrogen is used for the driver gas, the shock tube is vented first to the atmosphere through this vent line, then when the pressure drops to one atmosphere, through a mechanical vacuum pump which also exhausts through the roof.

The driven section consists of a transition section

and three 12' lengths of type 321 stainless steel, seamless tubing with a nominal wall thickness of 0.5". This and the driver tubing are available from standard commercial stock; this substantially reduces material costs compared to a design that requires specially formed tubing. The internal surface of these sections (as well as that of the driver tube) was honed to a surface finish of 10 to 20 micro-inches by a Los Angeles firm, Industrial Hydraulics, Inc. Before machining the ends, the honed sections were selected so as to minimize the step between any two adjoining sections. The internal diameter of the tube is 6.021 $\pm$ .002 inches with a maximum step height at any joint less than 0.002".

The method of connecting one tube section to another is unique in that no bolts or welds are employed. This eliminates the need for large flanges, welding, etc. Assembly time is also reduced. A cross sectional view of a typical joint is drawn to scale in figure 21. The driver end wall and the test section end wall are attached to the tube in a similar fashion (see figure 3). The snap rings are stock items. The beveled rings are machined from stainless steel forgings. The split-ring clamps are machined from annealed, 1040 carbon steel forgings, cut in half, and nickel plated to minimize corrosion. Because the latter forgings were annealed initially and then machined slowly, no loss of tolerance due to warping was

measured when the rings were cut in half. The force required to compress the O-ring in order to seal the joint (Fig. 21) is provided by a stainless steel "Marman" band clamp (Aeroquip Corp.).

The instrument ports were designed to give a maximum aperture within the allowable wall thickness required for strength. The minimum wall thickness is approximately 3/8". Each port consists of a one inch (.935") diameter access hole through the wall and a 2-1/8" diameter flat milled into the shock tube outer surface. The milled flat provides a surface for an O-ring seal. Four blind-tapped holes located on the periphery of the flat are used to bolt the instrumentation plugs to the shock tube. Two such ports are located 20 cm and 70 cm (centerline) from the downstream end of two tube sections. In the third 12' section which is used for most testing conditions (Fig. 3), there are six instrumentation ports - three pairs diametrically opposed. The distance from the end wall to the centerline of the three pairs is 10 cm, 20 cm, and 70 cm. The pair located at the 10 cm position has its axis rotated 90^{o} from the other two pairs. This pair of ports may be used for optical studies upon the insertion of optical grade glass windows or may be used to trigger oscilloscopes, etc., when the incident shock approaches the end wall.

The 50 cm distance between the ports on the upstream tube section and between two of the three pairs of ports

in the downstream section permits measurement of shock speeds with less than 1% error. (Normal procedure is to use a Beckman tenth-microsecond counter in conjunction with platinum thin film resistance gauges or piezoelectric gauges to measure the transit time of the incident shock over the 50 cm distance.)

Presently, one of the ports 70 cm from the test section end wall is used for connecting the driven section pressure gauge manifold to the shock tube. A specially designed, manually operated, flush fitting valve is used to seal the manifold off from the shock tube. The valve is designed to seal tighter when the driven section pressure is above one atmosphere, a condition that exists after each run. A glass McLeod gauge with a .01 - 100 μ Hg scale and a .1 - 5 mm Hg scale, a 0 - 1 mm Hg Hastings-Raydist thermocouple gauge, and a vacuum - 100 psig bourdon tube pressure gauge are connected to the manifold.

A.2 The Shock Tube as a Vacuum System

The tube was designed to have good vacuum characteristics. The stainless steel wall material and the honed internal surface enhance its vacuum capability. There are no welds or bolt holes exposed to vacuum in the entire assembly, eliminating them as a source of leaks or outgassing. Neoprene O-rings are used for seals in all the tube joints, instrumentation ports, and the various

Worchester ball valves used in the pumping system. The latter were selected because they offer good vacuum characteristics while retaining high pressure capability (at a relatively low cost). Presently these valves are all manually operated, but they could be converted to remote control by using air actuated pistons with solenoid valving.

With the present pumping system, described below, the driven section may be evacuated to a pressure of .03 μ Hg in half an hour. After pumping with a liquid nitrogen trapped, oil diffusion pump for half an hour, the initial combined leak and out-gassing rate is less than 3.0 μ Hg per hour. An ultimate pressure of .007 μ Hg can be attained with three hours of diffusion pumping with a corresponding initial leak-out-gassing rate of 1.7 μ Hg per hour.

A.3 The Pumping System

Three vacuum pumps are presently employed on the GALCIT 6" shock tube. Two mechanical vacuum pumps (a Kinney, Model KC 46 and a Welch, Model 1397B) are used to rough pump the driver and driven sections. (The Kinney pump, which has a larger pumping capacity than is needed for the shock tube, is also used on a central vacuum system which serves the rest of the laboratory.) The Welch pump is also used as a fore pump for a liquid nitrogen

trapped, six-inch, oil diffusion pump. The actual aperture of the diffusion pump is only 1.5" because a Worchester ball valve which is used to isolate this pump from the shock tube has a 1.5" diameter opening. The location of the test section pump ports is shown in figure 22. These ports were placed as close to the diaphragm as possible to minimize flow disturbance.

A.4 The Diaphragm Clamp and Transition Section Assembly

A number of methods for retaining the diaphragm while the driver is being pressurized were investigated during the design of the shock tube. Considerations for the clamping mechanism, in order of importance,were as follows:

1. It must be capable of retaining a diaphragm loaded to a differential pressure of 2000 psi, and it should be capable of holding diaphragms up to .125" thick.
2. It must be safe and simple enough for one-man operation, and it should be relatively inexpensive to build, assemble, and maintain. Also, the design should make it possible to change diaphragms quickly, to reduce cycling time.
3. If possible, it should be designed so that no machining of the diaphragms is necessary. This feature would reduce operating costs.

The present design meets all these criteria. A cut-away, scale drawing of the diaphragm-transition section assembly is shown in figure 22. The clamping of the diaphragm is accomplished by inserting pressurized hydraulic fluid between the driver transition section and the hydraulic pressure ring. This force is counteracted by the clamp (a ring cut in half; hinged at the top and latched at the bottom) which has a "U"-shaped cross section with vertical sides so that friction keeps the clamp from moving outward radially. The clamp is suspended from above on a window-sash type of counter balance arrangement so that it may be swung up and out of the way effortlessly when diaphragms are changed (see also the top of figure 23).

The hydraulic fluid is pressurized by means of an air operated, differential area pump (SC Hydraulic Engineering Corp. Model #40-500-4) which is mounted directly on the driver tube (see figure 20). Leather back-up rings in conjunction with standard Neoprene O-rings seal the oil. Note that in the event of seal failure no oil would enter the vacuum system. Air pressure of 85 psig produces a pressure of 5500 psig in the hydraulic fluid which provides an axial clamping force of 125 tons. A pressure of 2500 psig has been found sufficient to plastically deform the originally planar diaphragm between the two crimping rings (Fig. 22) and to retain and seal the diaphragm at burst pressures up to 1000 psia. The relative importance of the

double crimp in retaining the diaphragm has not been assessed. The crimp rings are separate stainless steel inserts so that in the event of damage, they can be removed from their respective transition sections.

With this system, it takes less than a minute to release the hydraulic clamping force, remove the broken diaphragm, insert and clamp a new diaphragm, and begin vacuum pumping.

The diaphragms need not be turned down to perfectly circular shape, have holes drilled in them or be pre-crimped prior to their use in the shock tube. It is sufficient to cut them into roughly circular shape (10.5" to 11.0" diameter) on a band saw from sheet stock.

Also, it is not necessary to scribe the diaphragms. A set of knife blades similar to those described in references 23 and 24, mounted in the driven transition section cut the diaphragm as it bulges under pressure. Only one of the mounting slots for the knife blades is shown in figure 22; the photograph in figure 23 shows the knife blades mounted in the driven transition section. Two blade curvatures are used. One set of blades is flat and provides a burst pressure that is roughly 50% of the free burst pressure for a given diaphragm. The other set is curved, providing a burst pressure that is roughly 80% of the free burst pressure. The burst pressure for the various diaphragm materials and thicknesses used to date

are repeatable to within 3 psia or less, providing very good shock Mach number repeatability. The burst pressures may be varied in approximately equal (percentage increase) steps from 50 psia to 985 psia by using the present selection of three diaphragm materials, five thicknesses, and the two sets of knife blades. Of course, continuous shock Mach number variation may be obtained by using mixtures of the nitrogen, helium, and hydrogen driver gases normally used.

Squaring plates are also shown in figure 23. These plates make the diaphragm section approximately square on the downstream side. By providing a "hinge line" for the diaphragm metal to bend on, it eliminates loss of petals after burst and protects the walls of the driven transition section from damage by impact of the petals. No petal loss has occurred with any of the diaphragms used, but occasionally small particles from the diaphragm, less than 0.1" in length, are found at the end of the test section. These are produced by either the impact of the petals on the squaring plates or by the petals flopping back and forth past the knife blades in response to shock reflection and re-reflection; thus, small pieces could be sheared off by the blades.

A.5 Controls

Other than the various valves used to isolate the vacuum pumps from the shock tube, all the controls are mounted in a panel beneath the shock tube near the test section end wall. The driver controls include a Matheson regulator (Model #3, 0 to 1500 psig delivery pressure) and a Circle Seal toggle valve (Model T900, vacuum to 6000 psig) which permit pressurizing the driver at virtually any convenient rate. The pressure in the driver may be read on any one of four pressure gauges. The ranges are such that the driver pressure may be determined with an error of 2% or less.

The pressure gauges used to measure the test section pressure were described at the end of section A.1.

The various bottles of test gas used in the shock tube are connected to a manifold which is in turn connected to a small volume mounted on the control panel. This volume, including lines, has been calibrated so that it has 1/200 of the volume of the shock tube. A bellows type Wallace and Tiernan pressure gauge with a range of 0 - 50 mm Hg is used to measure the pressure in the calibrated volume. The gas in this small volume may be "dumped" into the shock tube driven section through a 1" diameter copper line. The resulting pressure in the driven section is 1/200th of the pressure in the calibrated volume. The driven section pressure may also be measured directly with the .01 μ Hg -

5.0 mm Hg McLeod gauge.

Also mounted on the control panel are safety lights which show whether the various valves isolating the vacuum pumps and pressure gauges are open or closed and whether the diaphragm clamp is open or closed. (The diaphragm clamping mechanism is also designed so that no driver gas may be introduced when the clamp is not activated.)

A Beckman, Model #7370, tenth-microsecond counter and four transistorized, three stage, one megacycle band-pass amplifiers are also mounted on the control panel. The amplifiers resulted from the modification of a similar device designed by Dr. David Russell at the Jet Propulsion Laboratory. They were used in conjunction with thin film resistance gauges or piezoelectric pressure gauges and the Beckman counter to measure the incident shock velocity.

The design of the thin film resistance gauges and the instrumentation pads in which they are mounted is very similar to that shown in figure 6 of reference 23.

APPENDIX B

THE PRESSURE GAUGE CIRCUITRY AND THE TIME MARKER TECHNIQUE

The basic pressure gauge circuit, which is similar to that employed by Baganoff (Ref. 25), is presented in figure 24. The pressure gauge is represented by a variable capacitor in the figure. In order to eliminate loss of sensitivity from parasitic capacitance in connecting cables and to increase the input impedance to the point where R-C decay of the signal can be ignored, Baganoff designed and built the cathode follower circuit shown in the figure. It is attached to the pressure gauge with a twelve inch length of coaxial cable to eliminate parasitic capacitance. The input impedance is approximately 8 meg Ω so that the R-C decay time is two orders of magnitude longer than the dwell time (the dwell time is defined at the end of section 2.5) of the pressure gauge. The cathode follower has a gain of .98 and a rise time of better than .1 μ sec.

The magnitude of charging voltage to the pressure gauge could be varied by varying the input voltage to a 15 kV power supply (Del Electronics Corp., Model 15-1-6). By adding a switch to the output of this power supply, the polarity of the charging voltage could be reversed. This was necessitated by the electrical effect from the ionized gas on the pressure gauge (Sec. 3.1). The initial voltage on the pressure gauge was monitored with an

electrometer volt meter (Keithley Instruments, Model 600 A) using a 1000:1 divider probe (Keithley Instruments, Model 6103 A).

The output from the pressure gauge-cathode follower circuit was recorded on a Tektronix, Model 555, dual-beam oscilloscope. In order to expand the 24 μ sec dwell time of the pressure gauge as much as possible while retaining the entire pressure history on a single sweep, the oscilloscope sweep speed was set at approximately 3.0 μ sec/div for all the runs shown here. The 3.0 μ sec/div sweep speed is not calibrated on the Model 555 Tektronix oscilloscope so some other means of accurately indicating time on the oscillograms was required. A square-wave generator (Hewlett-Packard, Model 214A) with negative output voltage connected to the CRT cathode terminals on the back of the oscilloscope increases the intensity of the beam during each pulse from the square-wave generator. In this investigation a pulse repetition rate of 333 kc with a .3 μ sec pulse width was used to produce a bright spot on the oscillograms every 3.0 μ sec. The repetition rate was calibrated with a ten-megacycle counter (Beckman Instruments, Model 7370).

APPENDIX C

CALCULATION PROCEDURE FOR THE SHOCK REFLECTION PROCESS

C.1 Calculation of Equilibrium Conditions in Regions 3e, 4e, and 6e

To calculate the conditions in regions 3e and 4e (refer to the x-t diagram in figure 8), the gas in regions 2e and 5e is assumed to be in a uniform, equilibrium state, and the shocks S_{5e-4e} and S_{2e-3e} are assumed to move with constant velocity. The conditions in 2e and 5e are known. Under these assumptions the equations to compute the shock locii for S_{5e-4e} and S_{2e-3e} for the pressure-velocity diagram (figure 9) are as follows:

$$\frac{P_{4e}}{P_1} = \frac{P_{5e}}{P_1} + \gamma_1 \left(\frac{U_I}{a_1}\right)^2 \frac{\rho_{5e}}{\rho_1}\left(1 - \frac{\rho_{5e}}{\rho_{4e}}\right) \qquad \text{a)}$$

$$\frac{h_{4e}}{h} = \frac{h_{5e}}{h_1} + \frac{\gamma_1 - 1}{2}\left(\frac{U_I}{a_1}\right)^2 \left(1 - \left(\frac{\rho_{5e}}{\rho_{4e}}\right)^2\right) \qquad \text{b)} \qquad \text{(C1)}$$

$$\frac{u_{4e}}{a_1} = \frac{U_I}{a_1}\left(1 - \frac{\rho_{5e}}{\rho_{4e}}\right) \qquad \text{c)}$$

and

$$\frac{P_{3e}}{P_1} = \frac{P_{2e}}{P_1} + \gamma_1 \left(\frac{U_T + u_{2e}}{a_1}\right)^2 \left(\frac{\rho_{2e}}{\rho_1}\right)\left(1 - \frac{\rho_{2e}}{\rho_{3e}}\right) \qquad \text{a)}$$

$$\frac{h_{3e}}{h_1} = \frac{h_{2e}}{h_1} + \frac{\gamma_1 - 1}{2}\left(\frac{U_T + u_{2e}}{a_1}\right)^2\left(1 - \left(\frac{\rho_{2e}}{\rho_{3e}}\right)^2\right) \qquad b) \qquad (C2)$$

$$\frac{u_{3e}}{a_1} = \frac{\rho_{2e}}{\rho_{3e}} u_{2e} - \frac{U_T}{a_1}\left(1 - \frac{\rho_{2e}}{\rho_{3e}}\right) \qquad c)$$

where P, ρ, h, u, a_1, γ_1 are, respectively, the symbols for pressure, density, specific enthalpy, velocity, the speed of sound in region 1, and the ratio of specific heats in region 1 (5/3). The best way to compute the shock locii is to pick a value of U_1/a_1 (U_T/a_1), hold it fixed, assume a value of ρ_{5e}/ρ_{4e} (ρ_{2e}/ρ_{3e}) and calculate P_{4e} and h_{4e} (P_{3e} and h_{3e}) from equations (a) and (b). These values of pressure and enthalpy define the temperature and degree of ionization on the Mollier diagram. The computed pressure with the corresponding temperature and degree of ionization are used to calculate a new value of the density ratio ρ_{5e}/ρ_{4e} (ρ_{2e}/ρ_{3e}). Using the new density ratio to compute the pressure and enthalpy again, the process can be repeated until the assumed density ratio agrees with the computed value. In practice, only two or three iterations are required. By assuming two or three values of U_I/a_1 (U_T/a_1), the shock locii may be constructed on the pressure-velocity diagram (Fig. 9). The intersection of these two curves determines the pressure and fluid velocity P_{4e} and u_{4e}. The corresponding values of the shock speeds U_I and U_T may be determined from the momentum equations(written in

a different form than (C1a) and (C2a) above),

$$\frac{P_{4e}}{P_1} = \frac{P_{3e}}{P_1} = \frac{P_{5e}}{P_1} + \gamma \frac{\rho_{5e}}{\rho_1}\left(\frac{U_I}{a_1}\right)\left(\frac{u_{4e}}{a_1}\right) \tag{C3}$$

$$\frac{P_{4e}}{P_1} = \frac{P_{3e}}{P_1} = \frac{P_{2e}}{P_1} + \gamma\left(\frac{\rho_{2e}}{\rho_1}\right)\left(\frac{U_T + u_{2e}}{a_1}\right)\left(\frac{u_{2e} - u_{4e}}{a_1}\right) \tag{C4}$$

Then, with these values of U_I/a_1 and U_T/a_1, the values of ρ_{4e} and ρ_{3e} can be determined from equations (C1c) and (C2c). The temperature and degree of ionization are determined from the Mollier diagram using P_{4e} and the appropriate enthalpy.

The conditions in region 6e are determined in a similar manner, but the fact that the fluid velocity $u_{6e} = 0$ greatly simplifies the calculation. The shock-jump conditions across S_{4e-6e} are given by

$$\frac{P_{6e}}{P_1} = \frac{P_{4e}}{P_1} + \gamma\left(\frac{\rho_{4e}}{\rho_1}\right)\left(\frac{u_{4e}}{a_1}\right)^2\left(\frac{\sigma}{\sigma-1}\right) \qquad \text{a)}$$

$$\frac{h_{6e}}{h_1} = \frac{h_{4e}}{h_1} + \frac{\gamma-1}{}\left(\frac{u_{4e}}{a_1}\right)^2\left\{1 + \frac{2}{\sigma-1}\right\} \qquad \text{b)} \tag{C5}$$

$$\frac{U_{IR}}{a_1} = \frac{u_{4e}}{a_1}\left(\frac{1}{\sigma-1}\right) \qquad \text{c)}$$

where σ is the density ratio ρ_{6e}/ρ_{4e}. The procedure is to guess σ and, using the values of P_{6e} and h_{6e} calculated with (a) and (b) above, determine the temperature and degree of ionization on the Mollier diagram; with these values a new value of σ is computed. The procedure is

repeated until it converges.

C.2 Calculation of Conditions in Region 6f

C.2.1 The x-t Diagram and General Equations for "Frozen" Flow

In section 5.2, it was postulated that the maximum pressure observed on the end wall pressure histories

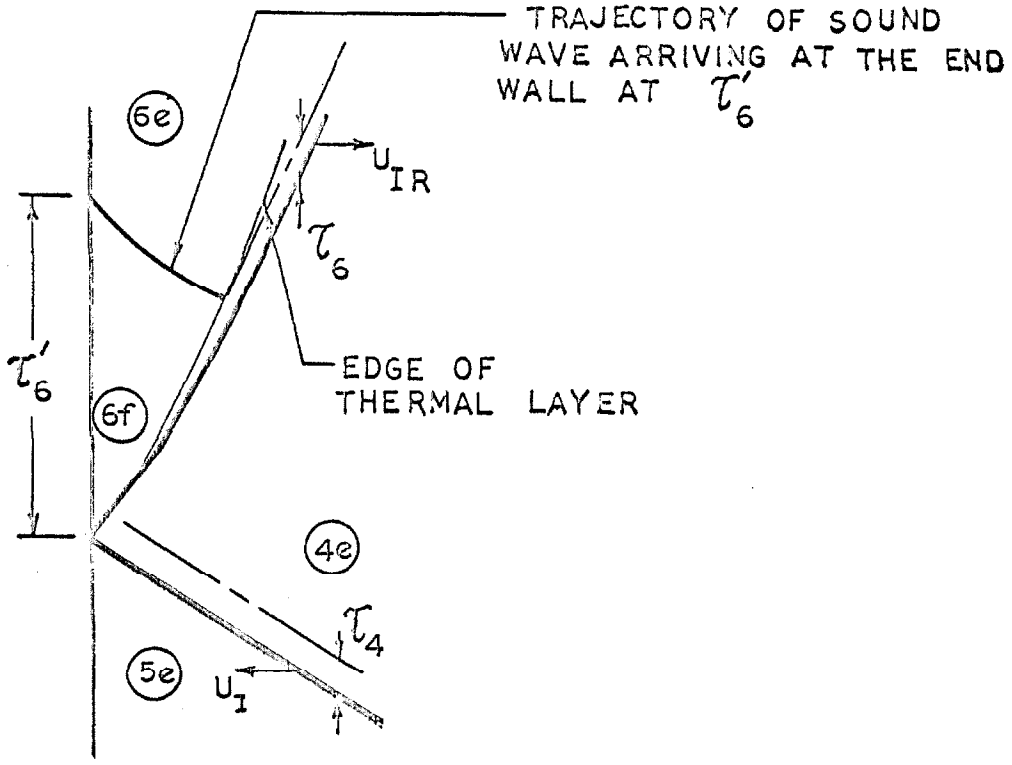

corresponds to a "frozen" pressure jump. An enlarged x-t diagram showing qualitatively only the reflection of the interaction shock from the wall is shown below. τ_6' is a few microseconds and τ_6 and τ_4 are a few tenths of a microsecond. The x-t diagram depicts the flow within

approximately one millimeter of the wall. The presence of a thermal layer in region 5e is ignored, and the velocity of the interaction shock S_{5e-4e} is its equilibrium value calculated by the procedure described in the preceding section. It is assumed that there is no reaction across the shock S_{4e-6f} next to the wall, but the fact that S_{4e-6f} is assumed to move into an equilibrium, ionized gas requires that further assumptions be made in order to calculate conditions in region 6f.

Consider the steady flow across the shock shown below

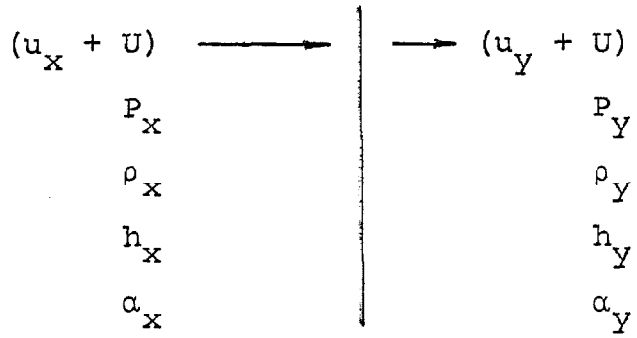

where the gas upstream is in an equilibrium ionized state. The conservation equations are in the familiar form:

$$\rho_x (u_x + U) = \rho_y (u_y + U) \tag{C6}$$

$$P_y = P_x + \rho_x (u_x + U)(u_x - u_y) \tag{C7}$$

$$h_x + \frac{(u_x + U)^2}{2} = h_y + \frac{(u_y + U)^2}{2} \tag{C8}$$

The energy associated with the atoms, ions, and

electrons must be accounted for in (C8). It is assumed that

$$h = \sum_i \frac{\rho_i}{\rho} h_i = \frac{\sum n_i m_i h_i}{\sum n_i m_i} \qquad (C9)$$

where

$$h_A = c_{pA} T_A \; ; \quad h_I = c_{pA} T_I + h^*_I ; \quad h_e = c_{pe} T_e \qquad (C10)$$

for the atoms, ions, and electrons respectively. h_I^* is the ionization potential per unit mass of the ions. The gas is assumed to be singly ionized ($n_e = n_I$) which is a very good assumption for the present experimental conditions in xenon.

Since the upstream gas is assumed to be in equilibrium,

$$h_x = (1 + \alpha_x)\, C_{P_A}\, T_x + \alpha_x\, h_I^* \qquad (C11)$$

The downstream enthalpy h_y may be written

$$h_y = \frac{1}{(n_{Ay} + n_{Iy})} \left\{ n_{Ay} C_{PA} T_{Ay} + n_{Iy} \left(C_{PA} T_{Iy} + h_I^*\right) + n_{ey} C_{PA} T_{ey} \right\} \qquad (C12)$$

It is reasonable to assume that the atom and ion temperatures are equal and that the atoms and ions are compressed equally across the shock, i.e.,

$$T_{Ay} = T_{Iy} \quad , \quad n_{Ax}/n_{Ay} = n_{Iy}/n_{Iy}. \qquad (C13)$$

Also, if the atom-atom free path ahead of the shock, λ_x, is crudely estimated from viscosity data for our conditions in xenon, it is found to be at least 200 to 300 times greater than the Debye length, $\lambda_{Dx} = (kT_x/4\pi n_{ex}e^2)^{\frac{1}{2}}$. This means that there can be no substantial charge separation across the shock and

$$n_{ex}/n_{ey} = n_{Ix}/n_{Iy} = n_{Ax}/n_{Ay} \tag{C14}$$

The simplest assumption that can be made regarding the electron temperature T_{ey} is that it is equal to the atom temperature T_{Ay}. There is no justification for this assumption other than the fact that the shock S_{4e-6f} is so weak that the temperature ratio T_{6f}/T_{4e} is very close to unity. With (C13), (C14), and $T_{ey} = T_{Ay}$, equation (C12) becomes

$$h_y = C_{PA}T_{Ay}\ (1 + \alpha_x) + \alpha_x\ h_I^* \tag{C15}$$

and (C8) then becomes

$$(1 + \alpha_x)\ C_{PA}T_x + \frac{(u_x + U)^2}{2} = C_{PA}T_{Ay}\ (1 + \alpha_x) + \frac{(u_y + U)^2}{2} \tag{C16}$$

Equations (C6), (C7), and (C16) describe the jump conditions for a shock moving into an equilibrium ionized gas; they are equivalent to having assumed that we have an inert mixture of atoms, ions, and electrons

with a modified gas constant

$$R' = (1 + \alpha_x)R_A \tag{C17}$$

C.2.2 Calculating Conditions in Region 6f

The conditions in region 4e are assumed known from the procedure discussed in section C.1 of this Appendix. Since the particle velocity must be zero at the wall, the strength of S_{4e-6f} is such that the velocity change across the shock is equal to u_{4e}. The pressure ratio P_{6f}/P_{4e} may be determined from the implicit equation

$$\frac{\Delta u}{a_{eff}} = \frac{\Delta u/a_1}{a_{eff}/a_1} = \frac{u_{4e}/a_1}{\sqrt{(1+\alpha_{4e})\frac{T_{4e}}{T_1}}} = \frac{\frac{1}{\gamma}\left(\frac{P_{6f}}{P_{4e}} - 1\right)}{\sqrt{1+\frac{\gamma+1}{2\gamma}\left(\frac{P_{6f}}{P_{4e}} - 1\right)}} \tag{C18}$$

which is nothing more than the equation for the locus of the shock S_{4e-6f} on a pressure-velocity diagram under our assumption that the gas may be treated as an inert mixture of atoms, ions, and electrons. By plotting the left hand side of equation (C18) versus the right hand side, the value of P_{6f}/P_{4e} for any specific values of u_{4e}, α_{4e}, and T_{4e} can be found easily.

For the purpose of constructing the x-t diagram (Fig. 8) and for calculating the value of τ_2 from the measured values of τ_2', the shock S_{4e-6f} (or S_{4e-6e} away from the wall) is assumed to move at its equilibrium velocity U_{IR}. This introduces little error and implies

that other conditions (i.e., density, temperature, etc.) across the shock S_{4e-6f} need not be calculated.

C.3 Determining τ_2 from τ_2'

In section 4.3 it was pointed out that the x-t diagram for the shock reflection process in figure 8 can not be constructed without using the experimentally observed times t_1 and τ_2' because the trajectory of the reflected shock S_{2f-5e} is not known. However, with the times t_1 and τ_2' and the values of U_I, U_{IR}, u_{4e}, and a_{6e}, calculated following the procedure described earlier in this Appendix, we can construct the trajectories of the shocks S_{5e-4e} and S_{4e-6e}, the leading edge of the centered rarefaction R_{6e-7}, and the contact surface C_{3e-4e}. The intersection of the shock S_{5e-4e} and the contact surface C_{3e-4e} gives the location of the interaction point. The distance from the end wall to the interaction point is given by the following equation:

$$X_I = \frac{U_I}{U_I - u_{4e}} \left[u_{4e} + \frac{U_{IR}\,(a_{6e} - u_{4e})}{U_{IR} + a_{6e}} \right] t_1 \quad . \tag{C19}$$

Knowing X_I, we can calculate the relaxation time τ_2,

$$\tau_2 = \tau_2' - X_I \left(\frac{1}{U_I} - \frac{1}{U_s} \right) \quad . \tag{C20}$$

For the conditions in this investigation, τ_2' is approximately 15% greater than τ_2. This correction is less than the run-to-run scatter of the data for τ_2'. Nevertheless, since all the data are shifted by approximately 15% and since the location of the interaction point was calculated for each case in order to construct the x-t diagram, the corrected values (τ_2) are presented in figures 12, 13, 16, 17, and 18. (Also, the agreement between the relaxation times measured with the photomultiplier tube and those measured with the pressure gauge (Fig. 13) is improved by this 15% correction.)

APPENDIX D

A NUMERICAL CALCULATION OF THE GAS PROPERTIES IN THE INCIDENT SHOCK RELAXATION REGION

Since the flow behind the incident shock is steady with respect to shock-fixed coordinates, the relaxation region there is easier to describe than the region behind the reflected shock. Following an approach similar to that in references 1, 2, and 26, all the flow variables in the nonequilibrium region behind the incident frozen shock front may be calculated. Comparing these results to the experimentally determined values of τ_2 (Fig. 25), one is able to determine an approximate value for the inelastic, electron-atom, excitation cross section. Also, the relative thickness of the ionization front and the relative importance of the atom-atom and electron-atom processes in the production of electrons can be assessed.

D.1 Assumptions

The assumptions made in this analysis are listed below.

1. The flow is steady and is described by the inviscid conservation equations, a two-temperature equation of state, and an energy balance equation for the elastic collisions between electrons and ions and atoms and the inelastic collisions between electrons and atoms.

2. The gas is singly ionized.

3. Electrons are produced by collisions between atoms and other atoms or between electrons and atoms. The ionization process proceeds in two steps, i.e., the atom is first excited to the first metastable state* (8.3 ev) and subsequently ionized. The excitation process is the rate determining step.

The two-step atom-atom process in xenon has been observed experimentally (Refs. 3, 4). Weymann (Ref. 27), assuming excitation to the first excited state* and trapping of resonance radiation, showed theoretically that the two-step process is more efficient. The two-step, electron-atom process has been used successfully in analyses for argon ionization relaxation (Refs. 1, 2), and it is reasonable to assume that this process is dominant in the xenon reaction. (The probability that an electron will ionize an atom in a single collision is much smaller than the corresponding probability for excitation.)

4. The atoms and ions are in equilibrium with one another. The electrons are also described by a Maxwellian distribution, but their average temperature, T_e, is much lower than the average temperature of the atoms and ions, T_A. The lower

* See the footnote on the bottom of page 57.

electron temperature results from the fact that the electrons acquire energy by elastic collisions with the heavier species very slowly while they lose energy through inelastic collisions with atoms very rapidly. T_e may be found as a function of T_A and the specie number densities by equating the elastic energy transfer to the inelastic energy transfer (Ref. 1).

5. The effects of recombination and radiation may be neglected. Wong and Bershader (Ref. 2) found experimentally and theoretically that for the purpose of determining the total relaxation time and the state of the gas for all but the last 10% of the relaxation region (near equilibrium), this assumption would introduce little error in their investigation of argon. The effect of this assumption on the present investigation is to under-estimate the total relaxation time slightly; the calculated ionization front is thinner than would be observed experimentally.

6. Both the atom-atom and the electron-atom inelastic cross sections vary linearly with energy.

$$(\sigma_{A-A})_{inelastic} = B_{A-A} (E_A - 8.3) \qquad (6a)$$

$$(\sigma_{e-A})_{inelastic} = B_{e-A} (E_e - 8.3) \qquad (6b)$$

Harwell and Jahn (Ref. 3) and Kelly (Ref. 4) assumed the functional form in equation (6a) to determine values of B_{A-A} for xenon. Kelly's value for xenon,

$$B_{A-A} = 1.8 \times 10^{-20} \pm \text{cm}^2/\text{ev} \quad ,$$

is used in this analysis*.

---

* Wong and Bershader (Ref. 2) used a different functional form for the atom-atom, inelastic cross section for argon. They used the experimentally determined fact that

$$(dn_e/dt)_{A-A} \sim \exp(E'/kT_A)$$

(where E' = 11.5 ev) to derive the functional form. They found that

$$\sigma_{A-A} = B'_{A-A} \frac{(E_A/E' - 1)^{5/2}}{E_A/E'}$$

B'_{A-A} was determined by fitting their computed total relaxation time to their experimental results. Since their interferometer technique was not sensitive to the small density changes which occur during the initial portion, the atom-atom dominated portion, of the relaxation process, they could not evaluate the validity of their "derived" functional form for this cross section. Moreover, since either functional form for the cross section (the one above or the one in equation (6a)) produces a practically straight line on a semilog plot of $(dn_e/dt)_{A-A}$ versus $1/T_A$ over the range of temperatures investigated in references 3 and 4, the experimental data (Refs. 3, 4) can not be used to confirm the validity of either expression for the atom-atom, inelastic cross section exclusive of the other.

The functional form of the electron-atom inelastic cross section is suggested by the use of a similar functional form for argon (Ref. 1). However, no measurements of this excitation cross section for xenon could be found in the literature so B_{e-A} is an unknown constant in the calculation. By comparing the computed total relaxation times τ_2 with the experimental results, B_{e-A} can be determined approximately. An order of magnitude estimate for B_{e-A} was obtained before making the numerical calculation by comparing the total (elastic plus inelastic) electron-atom cross section measured by Ramsauer (see reference 28, page 9, for example) to the elastic, electron-atom cross section*. This procedure yielded a value of $\sim 5 \times 10^{-16}$ cm^2/ev for B_{e-A}. (The comparison between the calculated relaxation times (τ_2) and the measured values yields a value for B_{e-A} that is approximately the same as this crude approximation, i.e., 5×10^{-16} cm^2/ev.)

---

* Curves of relative intensity versus scattering angle for elastic, electron-atom collisions in xenon are presented in reference 28 on pages 91, 92, and 125. By numerically integrating these curves, the elastic cross section can be determined to within an unknown constant. The unknown constant is obtained by equating the elastic cross section to the total cross section for electron energies of one or two electron volts.

D.2 The Equations Describing the Relaxation Region

The variables of the problem are n_e, T_A, T_e, α, ρ, P, and u, which are, respectively, the electron number density, the atom and ion temperature, the electron temperature, the degree of ionization, the mass density, the pressure, and the fluid velocity in shock-fixed coordinates. The constants in the following equations are k, m_A, E_m, and E_{ion} which are, respectivcly, Boltzmann's constant, the atomic mass of xenon, the energy of the first metastable (excited) state in xenon (8.3 ev), and the ionization energy (12.13 ev).

$$P = n_e(kT_A/\alpha + kT_e) \tag{D1}$$

and an energy balance equation for the collisions between electrons and atoms and ions

$$(Q_{e-A})_{\text{inelastic}} = (Q_{e-I})_{\text{elastic}} + (Q_{e-A})_{\text{elastic}} \tag{D2}$$

are needed. The rate of energy loss for the electrons due to inelastic collisions with atoms is given by:

$$(Q_{e-A})_{\text{inelastic}} = \left[\frac{dn_e}{dt}\right]_{\text{total}} (5/2\ kT_e + E_{ion}) \tag{D3}$$

where

$$\left[\frac{dn_e}{dt}\right]_{\text{total}} = \left[\frac{dn_e}{dt}\right]_{A-A} + \left[\frac{dn_e}{dt}\right]_{e-A}$$

which are given by equations (7a) and (7b). The electrons gain energy by elastic collisions with ions and atoms. The contribution from collisions with ions is (Ref. 29)

$$(Q_{e-I})_{elastic} = \frac{n_e^2 e^4}{m_A}\left(\frac{8\pi m_e}{kT_e}\right)^{\frac{1}{2}}\left(\frac{T_A - T_e}{T_e}\right)\ell n\left[\frac{9(kT_e)^3}{8\, n_e e^6}\right] \qquad (D4)$$

and from the atoms is

$$(Q_{e-A})_{elastic} = \frac{m_e^2}{m_A}\left(\frac{T_A}{T_e} - 1\right) n_e^2 \left(\frac{1-\alpha}{\alpha}\right) S_{e-A} \qquad (D5)$$

S_{e-A} is a function of the electron temperature. The following form is derived in reference 1,

$$S_{e-A} = \frac{8\pi}{\sqrt{2}(\pi m_e kT_e)^{3/2}} \int \epsilon^2 c_{e-A}(\epsilon)\, \exp(-\epsilon/kT_e)\, d\epsilon$$

where ϵ is the energy of the electrons. S_{e-A} was obtained by integrating numerically over the elastic, electron-atom cross section data for xenon given in reference 28.

By solving the conservation equations, equation (D1), and equation (D2) simultaneously and integrating step by step, the flow variables in the relaxation region behind the incident frozen shock front may be determined. It is also of interest to plot the variation of the flow quantities in terms of laboratory time (all the integrations being carried out in particle time). Laboratory time is related to particle time by the integral

$$t_{lab} = \int \rho/\rho_1 \, dt_{particle}$$

This integration was performed numerically.

D.3 Results of the Numerical Calculation

The results for the incident shock relaxation times in laboratory coordinates are shown in figure 25 for various assumed values of B_{e-A}. The results show two things.

(1) The total relaxation time is not very dependent upon the electron-atom, inelastic cross section since in this figure B_{e-A} has been varied by a factor of three with little effect on the calculated relaxation times.

(2) The value of B_{e-A} is approximately that predicted by crudely comparing the elastic cross section data with the curve for the total electron-atom cross section. (Refer to the discussion under assumption 6 in section D.1 of this Appendix.)

Figure 26a shows the calculated variation of the degree of ionization as a function of laboratory time. The vertical line marks the point at which the production of electrons by electron-atom collisions is equal to the production by atom-atom collisions. This occurs within the first 15% of the total relaxation time for all the calculated conditions. Hence, it can be deduced that the electron-atom process is the rate determining one. As mentioned above, the thinness of the ionization front is

exaggerated since the effects of recombination have been ignored. However, even if the ionization front is doubled in thickness, the predicted total relaxation time is increased by less than 10%.

Figure 26b shows the variation of the atom and electron temperatures with laboratory time for a typical condition. One can see that the assumption that the equilibrium temperature serves as an approximate value for the electron temperature is very good. This approximation is used in comparing the relaxation times behind the reflected shock to those behind the incident shock (cf., the discussion in section 6.7).

REFERENCES

1. Petschek, H. E., and Byron, S., Ann. Phys. 1, 270 (1957).

2. Wong, H., and Bershader, D., J. Fluid Mech. 26, 459 (1966).

3. Harwell, K. E., and Jahn, R. G., Phys. Fluids 7, 214 (1964); also erratum 7, 1554 (1964).

4. Kelly, A. J., J. Chem. Phys. 45, 1723 (1966); also Ph.D. Thesis, California Institute of Technology (1965).

5. Johnston, H. S. and Kornegay, W. M., Trans. Faraday Soc. 57, 1563 (1961); also Kornegay, W. M. and Johnston, H. S., J. Chem. Phys. 38, 2242 (1963).

6. Camac, M., and Feinberg, R. M., J. Fluid Mech. 21, 673 (1965).

7. Camac, M., and Feinberg, R. M., "Thermal Conductivity of Argon at High Temperatures", Avco Everett Research Report #168 (1963).

8. Friedman, H. S. and Fay, J. A., Phys. Fluids 8, 1968 (1965).

9. Baganoff, D., Rev. Sci. Instr. 35, 288 (1964).

10. Baganoff, D., Proc. 5th International Shock Tube Symposium, Silver Spring, Md., April, 1965.

11. Blackman, V., J. Fluid Mech. 1, 61 (1956).

12. Baganoff, D., J. Fluid Mech. 23, 209 (1965).

13. Roth, W., and Gloerson, P., J. Chem. Phys. 29, 820 (1958).

14. Turner, E. B., Ph.D. Thesis, U. of Michigan (1956); also ASTIA Document No. AD 86309.

15. Weymann, H. D., Phys. Fluids 3, 545 (1960).

16. Klein, A. F., Ph.D. Thesis, California Institute of Technology (1967).

17. Goldsworthy, F. A., J. Fluid Mech. 5, 164 (1959).

REFERENCES (cont.)

18. Liepmann, H. W , and Roshko, A., Elements of Gas Dynamics, Wiley, New York (1957).

19. Mueller, J. N., "Equations, Tables, and Figures for Use in the Analysis of Helium Flow at Supersonic and Hypersonic Speeds", NACA-TN 4063 (1957).

20. Arave, R. J., "Thermodynamic and Normal Shock Properties of the Inert Gases in Ionization Equilibrium", Boeing Report D 2-22291 (October, 1963).

21. Sturtevant, B., and Slachmuylders, E., Phys. Fluids 1, 1201 (1964).

22. Chapman, S., and Cowling, T. C., The Mathematical Theory of Non-Uniform Gases, Cambridge University Press (1960).

23. Liepmann, H. W., Roshko, A., Coles, D., Sturtevant, B., Rev. Sci. Instr. 33, 625 (1962).

24. Roshko, A., and Baganoff, D., Phys. Fluids 4, 1445 (1961).

25. Baganoff, D., Ph.D. Thesis, California Institute of Technology (1964).

26. Morgan, E. J., and Morrison, R. D., Phys. Fluids 8, 1608 (1965).

27. Weymann, H. D., "On the Mechanism of Thermal Ionization behind Strong Shock Waves", U. of Maryland Tech. Note BN-144 (1958).

28. Massey, H. S. W., and Burhop, E. H. S., Electronic and Ionic Impact Phenomena, Oxford University Press, London (1956).

29. Landau, L., Physik. Z. Sowjetunion 10, 154 (1936).

Table I SUMMARY OF PRESSURE GAUGE MEASUREMENTS FOR $P_1 \neq 0.5$ mm Hg

M_s	P_1 mm Hg	$\left[\frac{P_{5f}}{P_1}\right]_{th}$	$\left[\frac{P_{5f}}{P_1}\right]_{exp}$	$\left[\frac{P_{5e}}{P_1}\right]_{th}$	$\left[\frac{P_{5e}}{P_1}\right]_{exp}$	$\left[\frac{P_{6f}}{P_1}\right]_{th}$	$\left[\frac{P_{6f}}{P_1}\right]_{exp}$	$\left[\frac{P_{6e}}{P_1}\right]_{th}$	$\left[\frac{P_{6e}}{P_1}\right]_{exp}$
12.6	1.500	1200	1100	925	1030	2100	2400	1940	2230
13.3	1.000	1320	1220	1010	1110	2675	2960	2450	2760
13.9	.750	1440	1440	1095	1160	3250	3600	2920	3330
16.5	.250	2030	1860	1520	1440	6720	6820	6100	6010
16.9	.200	2120	2040	1590	1400	7300	7670	6720	6200*
18.3	.100	2470	2310	1850	1850	9750	10400		*
20.4	.100	3100	2770	2300	2020	14500	15100		*

* Rarefaction R_{6e-7} arrived at the end wall before pressure decreased to P_{6e}, i.e., no plateau present on oscillograms.

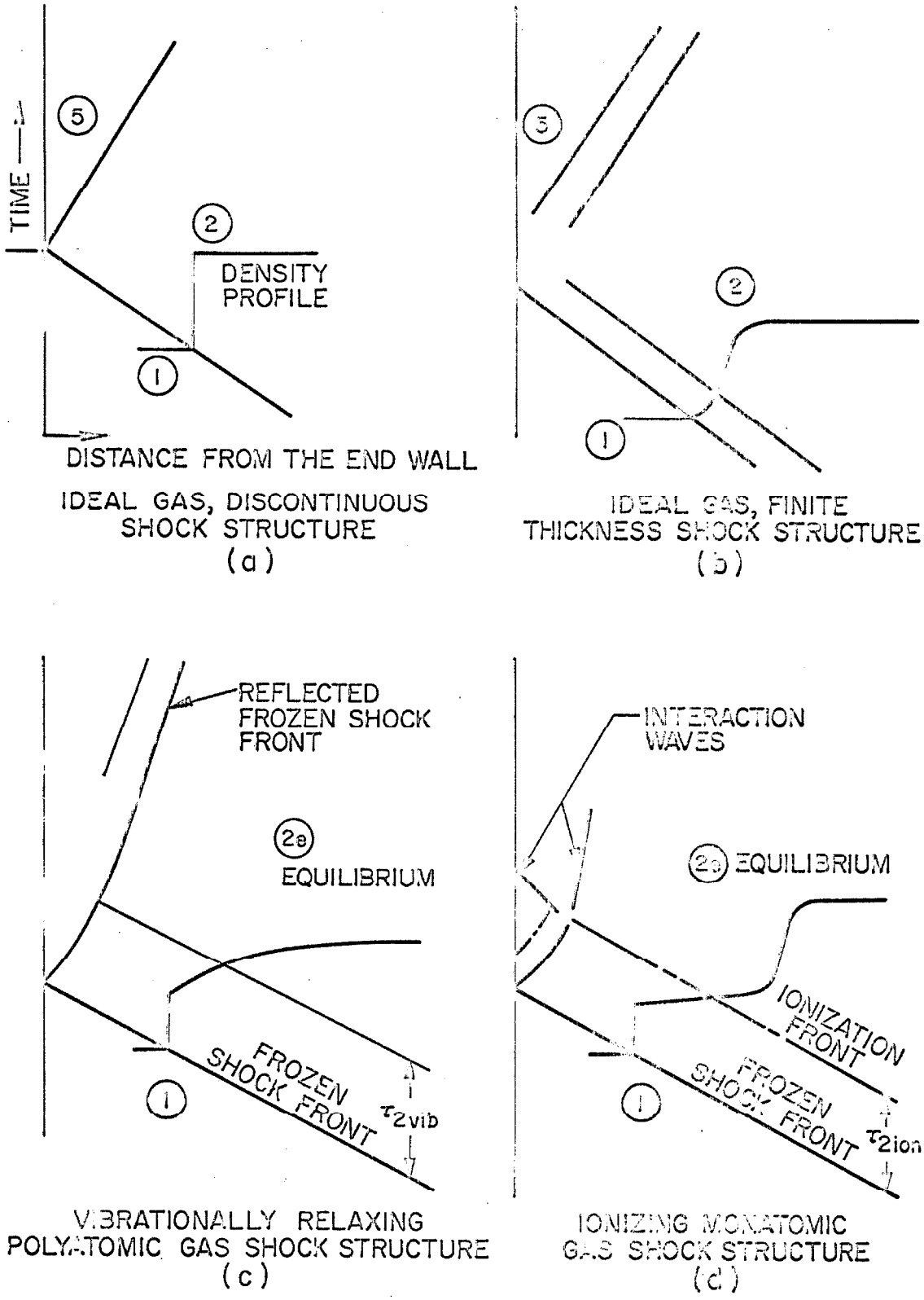

Figure 1 SHOCK REFLECTION PROCESSES FOR VARIOUS INCIDENT SHOCK STRUCTURES

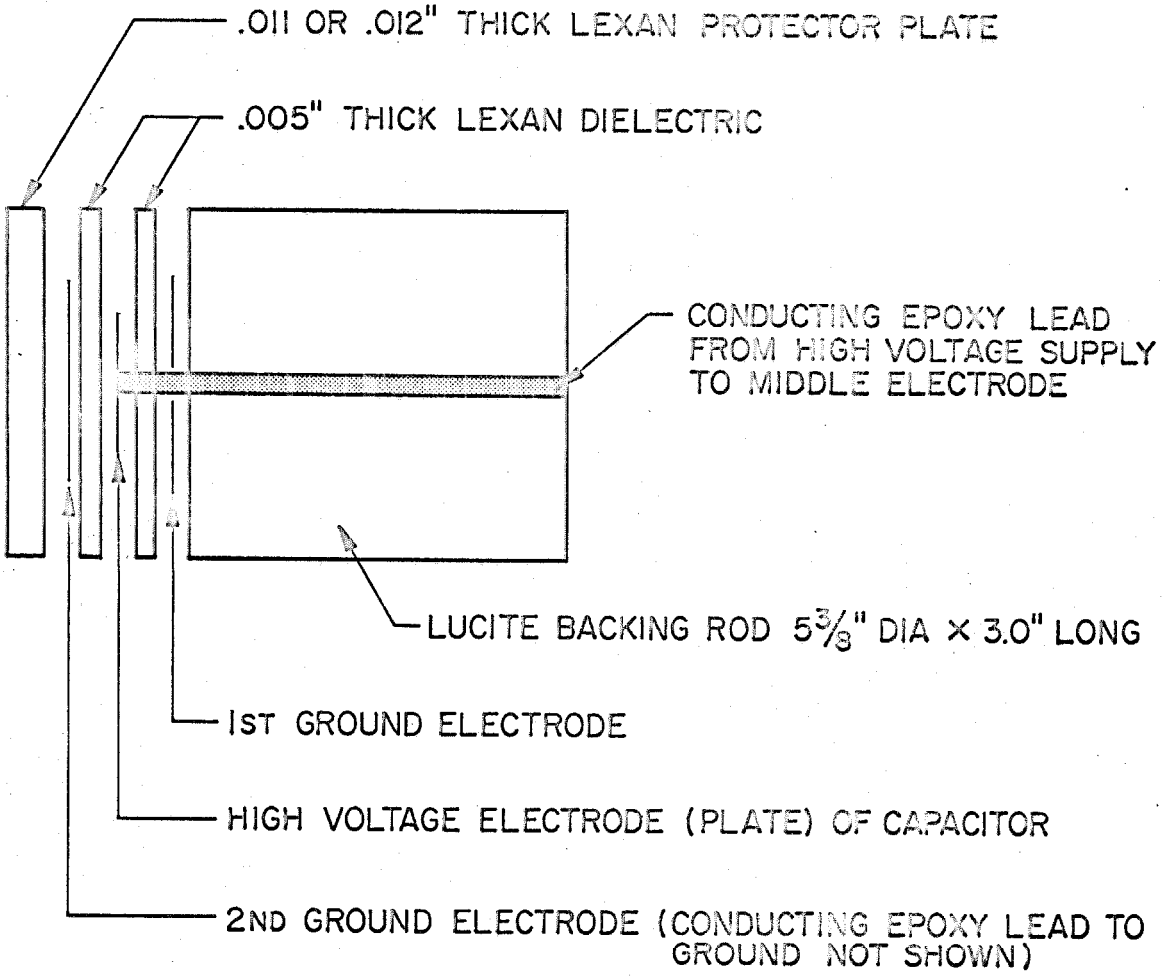

Figure 2 SCHEMATIC OF PRESSURE GAUGE DESIGN

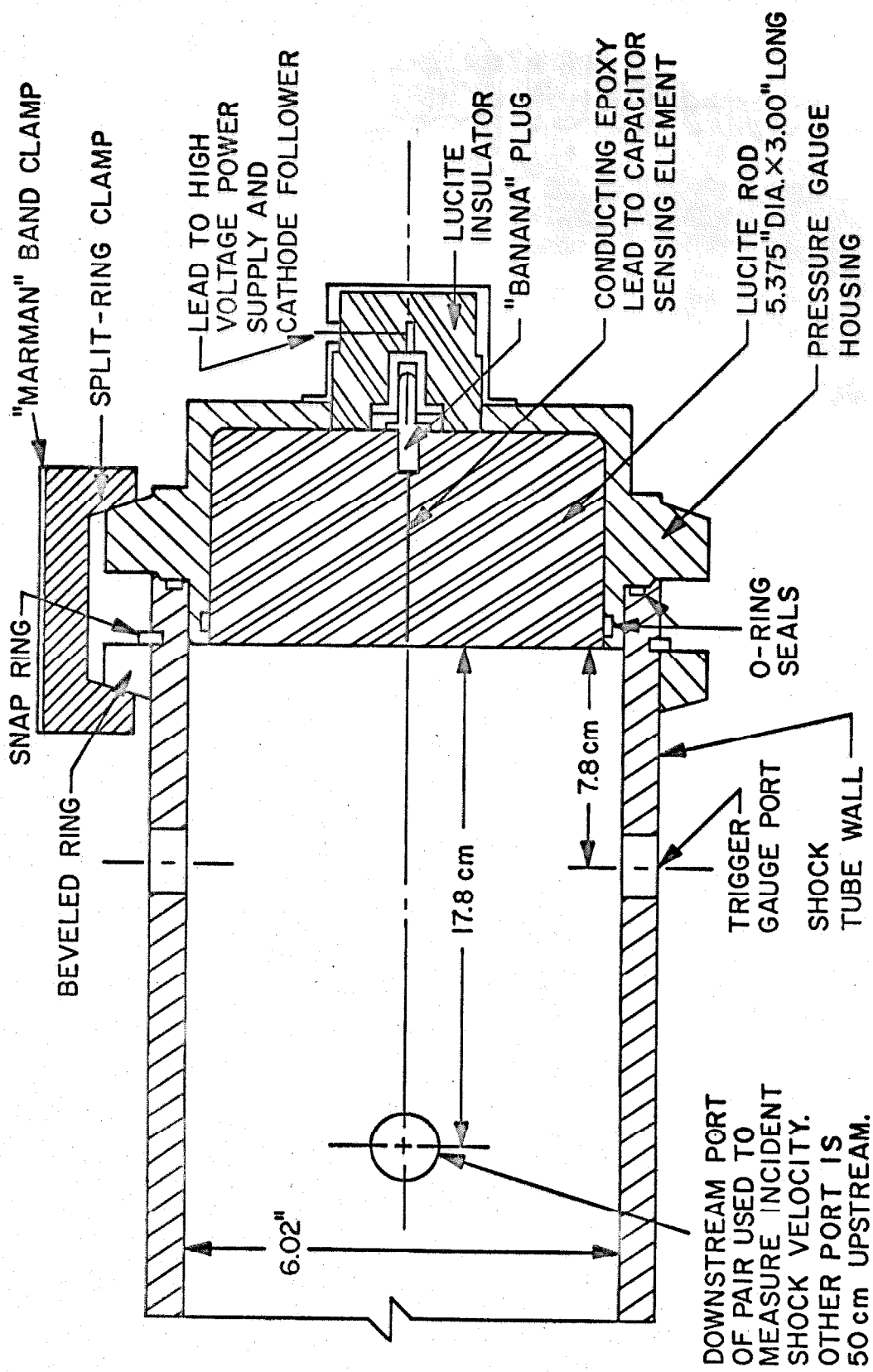

Figure 3 SECTIONAL VIEW OF END WALL PRESSURE GAUGE IN THE GALCIT 6" SHOCK TUBE

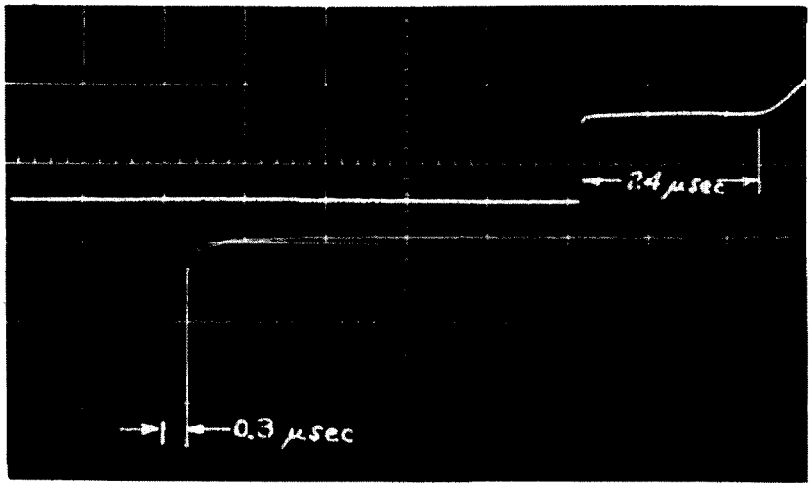

M_s = 3.15 P_1 = 5.0 mm Hg NITROGEN

UPPER BEAM: 10 μsec/div; 20 mv/div

LOWER BEAM: 1 μsec/div; 10 mv/div

RISETIME = .3 μsec

DWELL TIME = 24 μsec

SENSITIVITY = 29.8 μv/mm Hg/Kv CHARGING VOLTAGE

FIGURE 4 RESULTS OF TYPICAL PRESSURE GAUGE CALIBRATION RUN

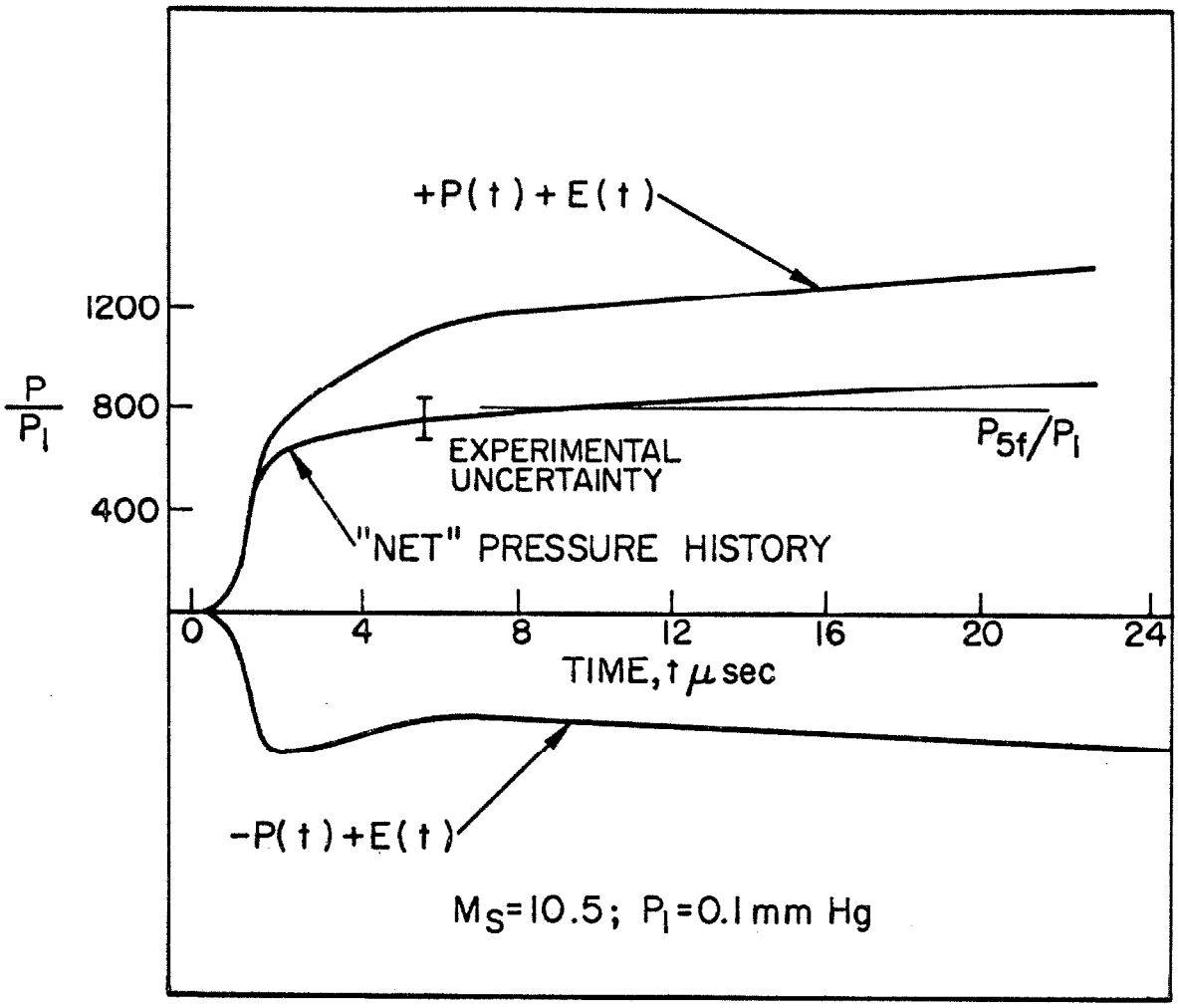

Figure 5 PAIR OF RUNS SHOWING EXTREME "ELECTRICAL EFFECT" AND THE RESULTANT "NET" PRESSURE HISTORY

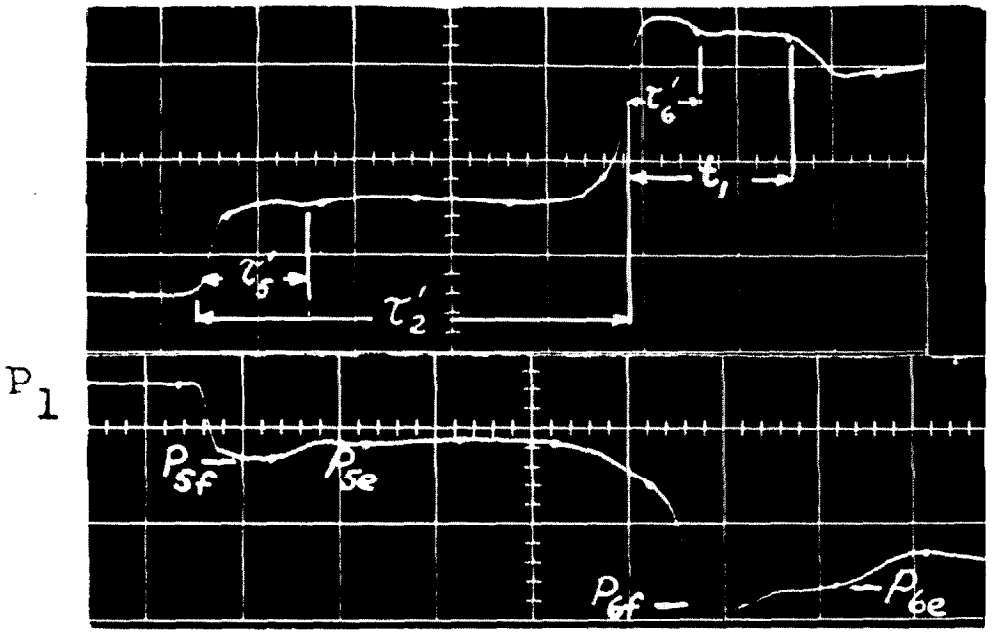

$M_s = 15.1$ $P_1 = 0.5$ mm Hg

SWEEP SPEED $\simeq$ 3.0 μsec/div

SENSITIVITY = 50 mv/div

TIMING MARKS ARE 3.0 μsec APART

FIGURE 6 TYPICAL PAIR OF RUNS SHOWING END WALL PRESSURE HISTORY IN XENON

Figure 7 A SERIES OF END WALL PRESSURE HISTORIES IN XENON; P_1 = 0.5 mm Hg TIMING MARKS ARE 3.0 μsec APART

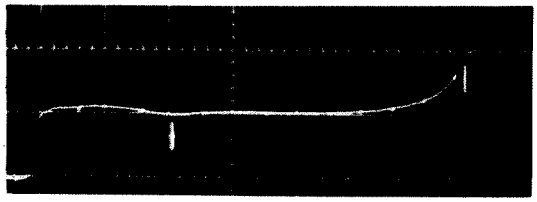

M_s = 13.5

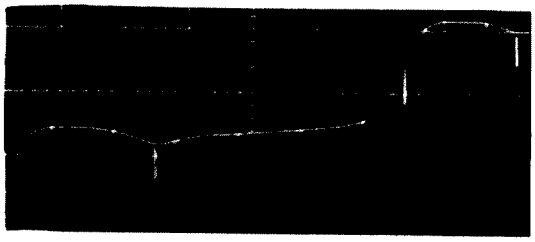

M_s = 14.0

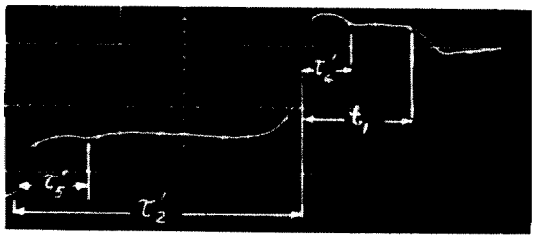

M_s = 15.1

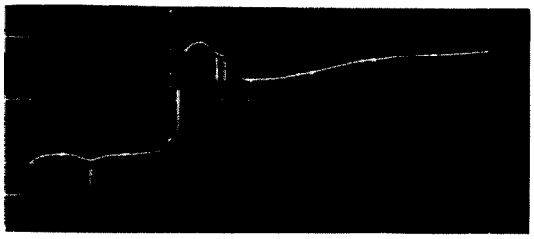

M_s = 16.2

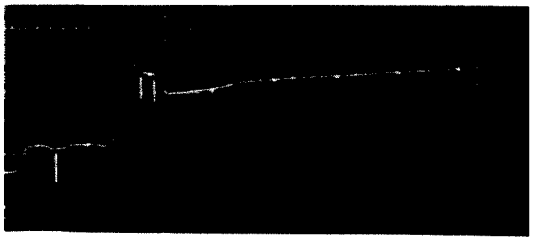

M_s = 17.9

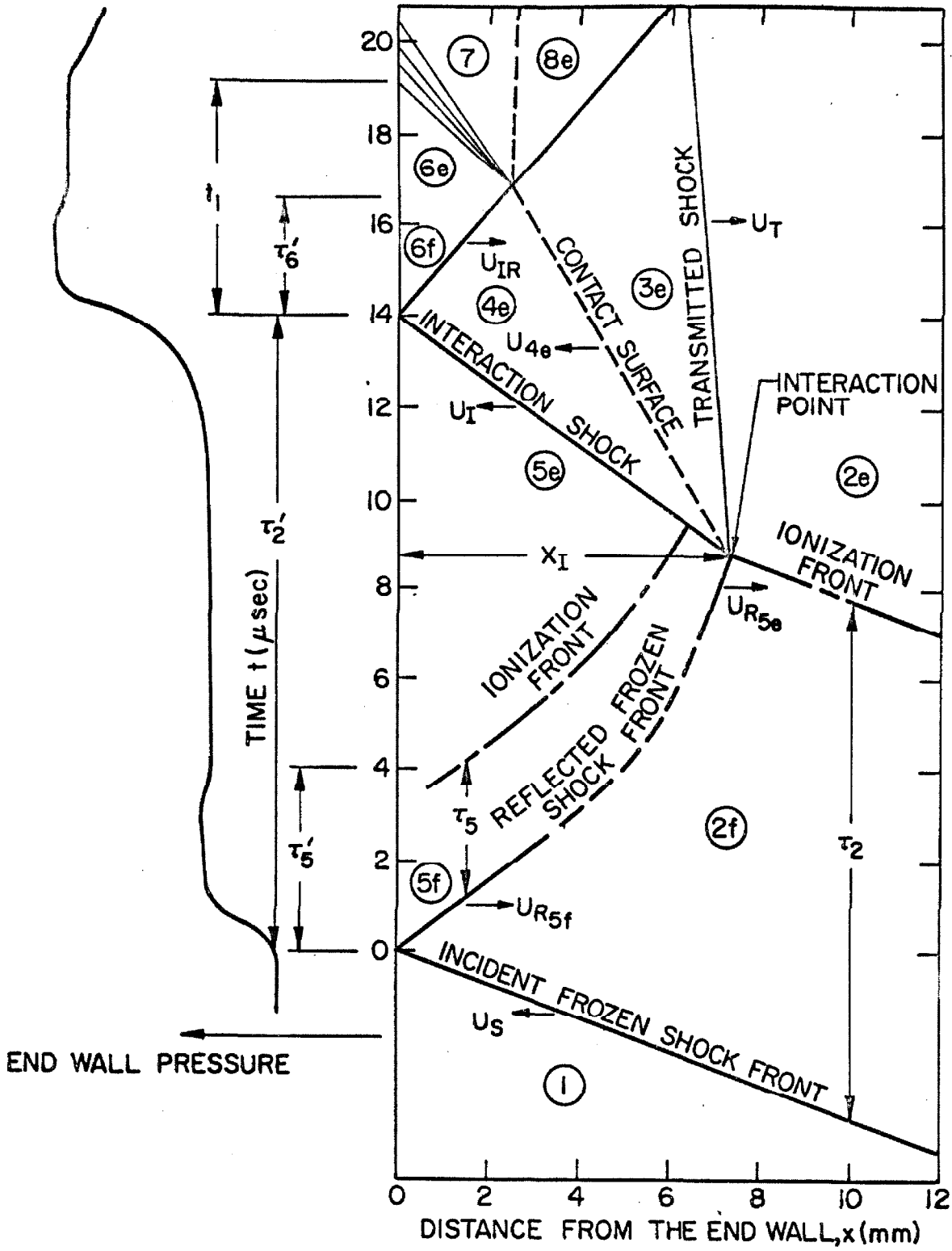

Figure 8 x-t DIAGRAM FOR SHOCK REFLECTION PROCESS IN XENON; M_S=15.1, P_1=.5 mm Hg

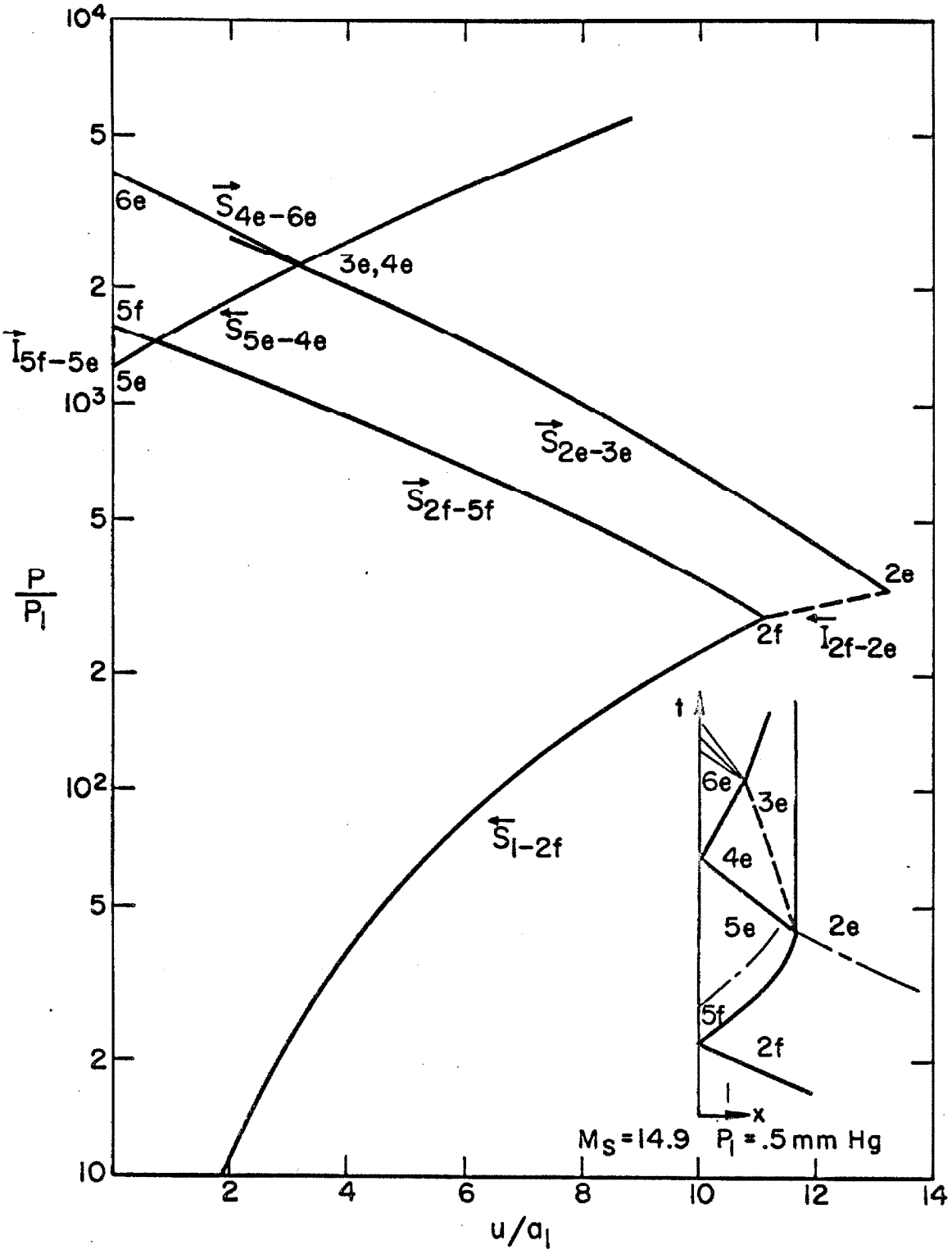

Figure 9 PRESSURE-VELOCITY DIAGRAM FOR THE SHOCK REFLECTION PROCESS IN XENON

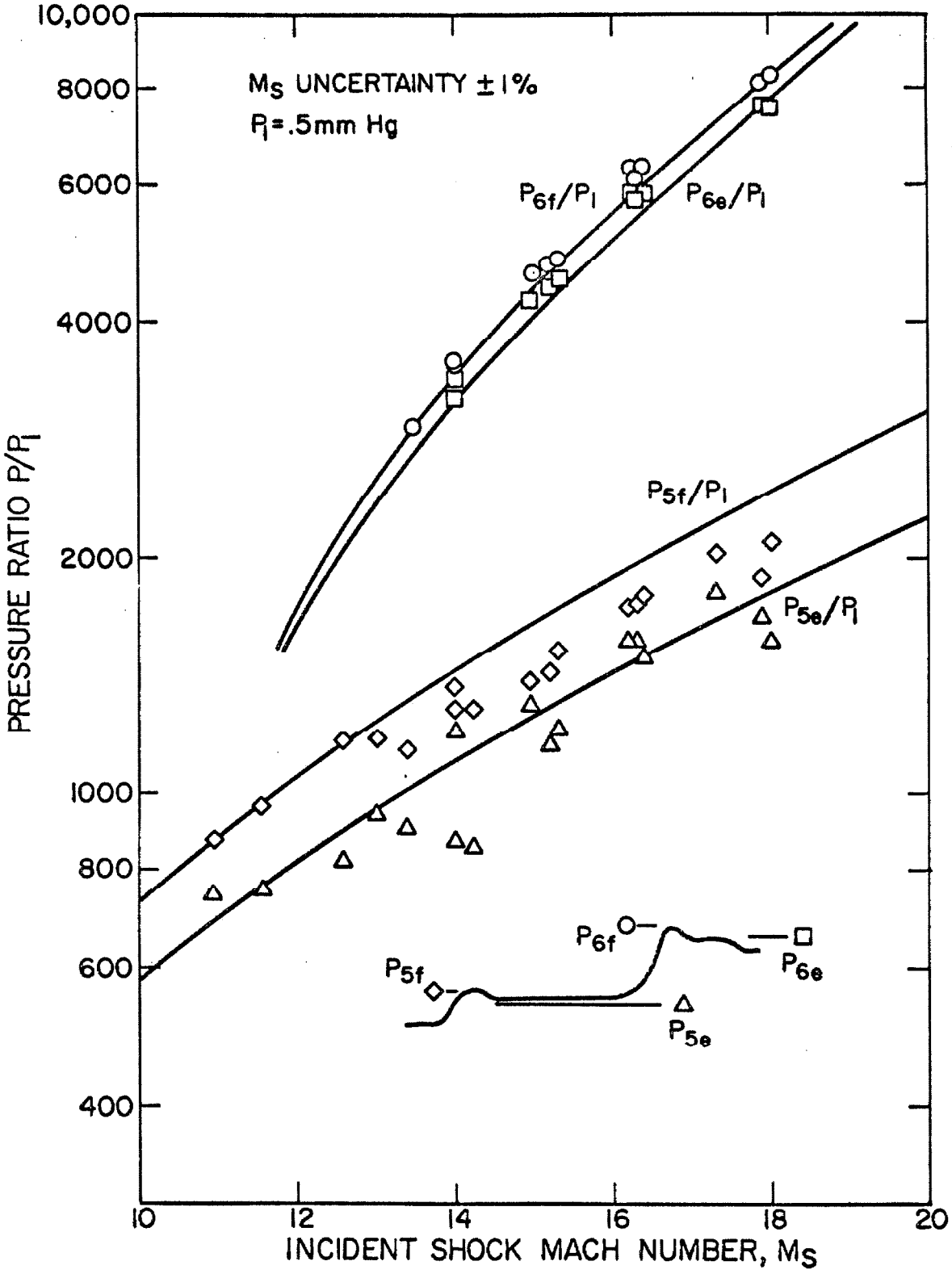

Figure 10 SUMMARY OF END WALL PRESSURE DATA

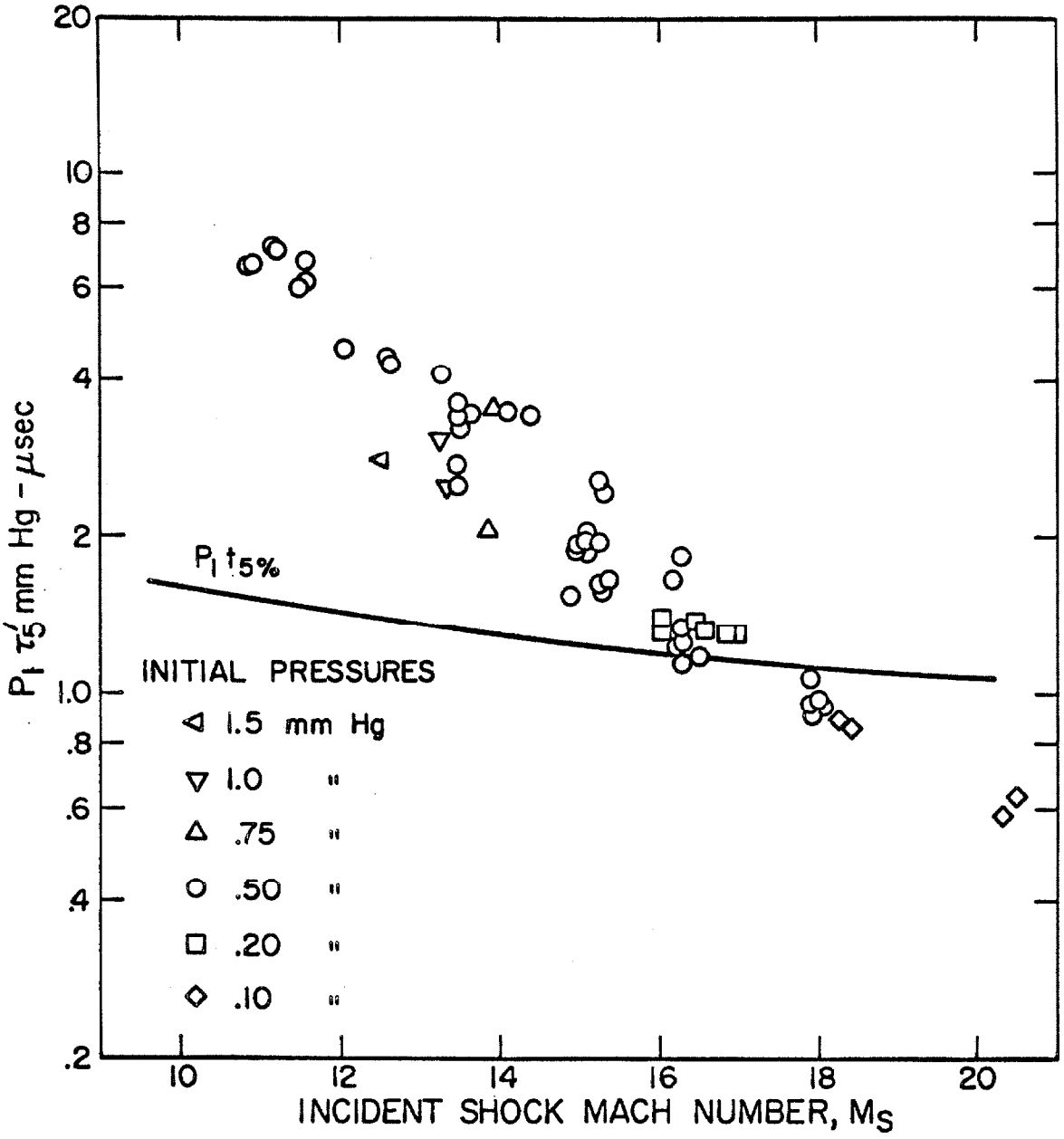

Figure 11 COMPARISON BETWEEN RELAXATION TIME τ_5' AND DURATION OF END WALL HEAT TRANSFER EFFECT ON MEASURED PRESSURES

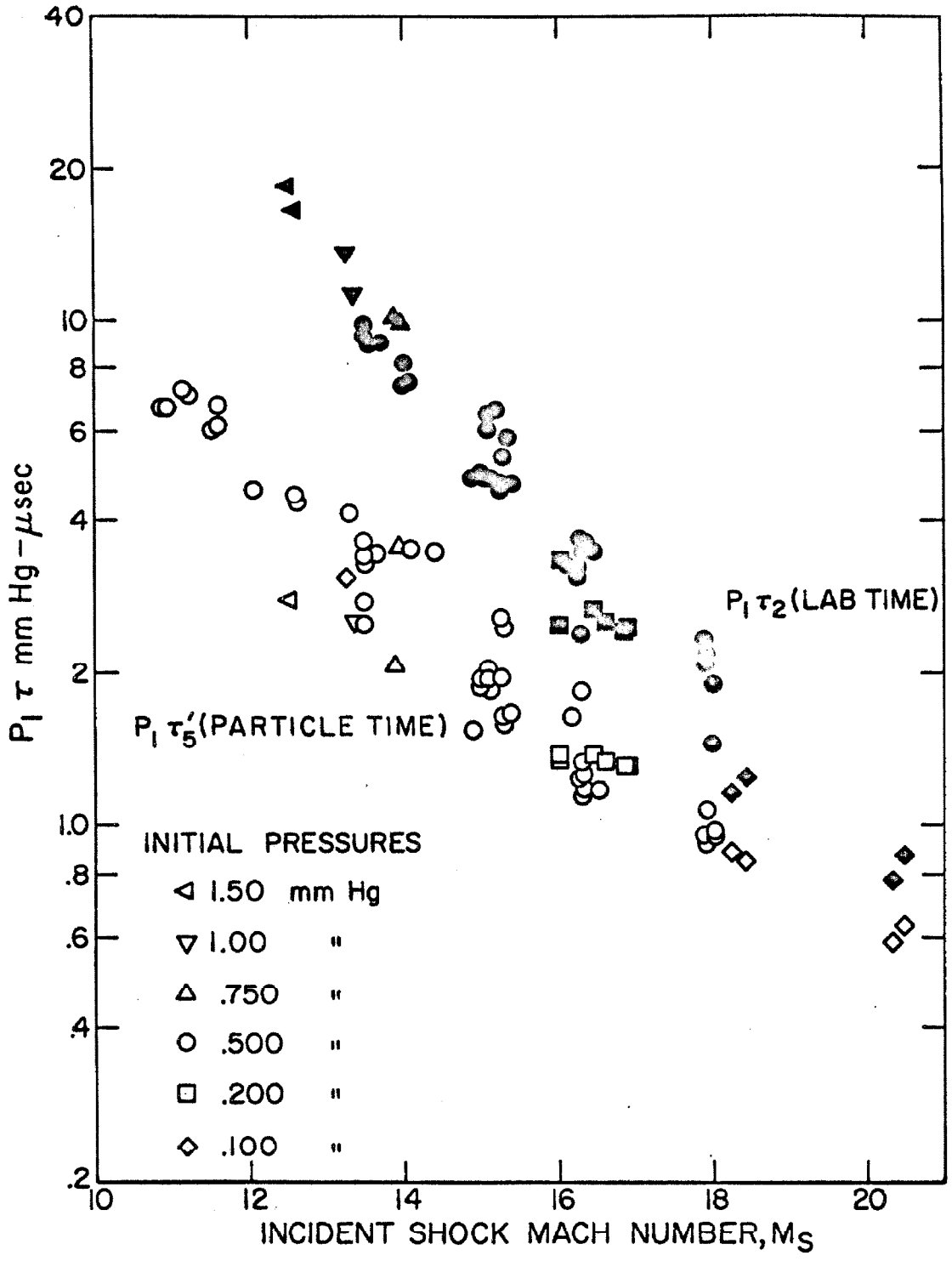

Figure 12 SUMMARY OF RELAXATION TIME DATA $P_1\tau_2$ AND $P_1\tau_5'$ VERSUS INCIDENT SHOCK MACH NUMBER

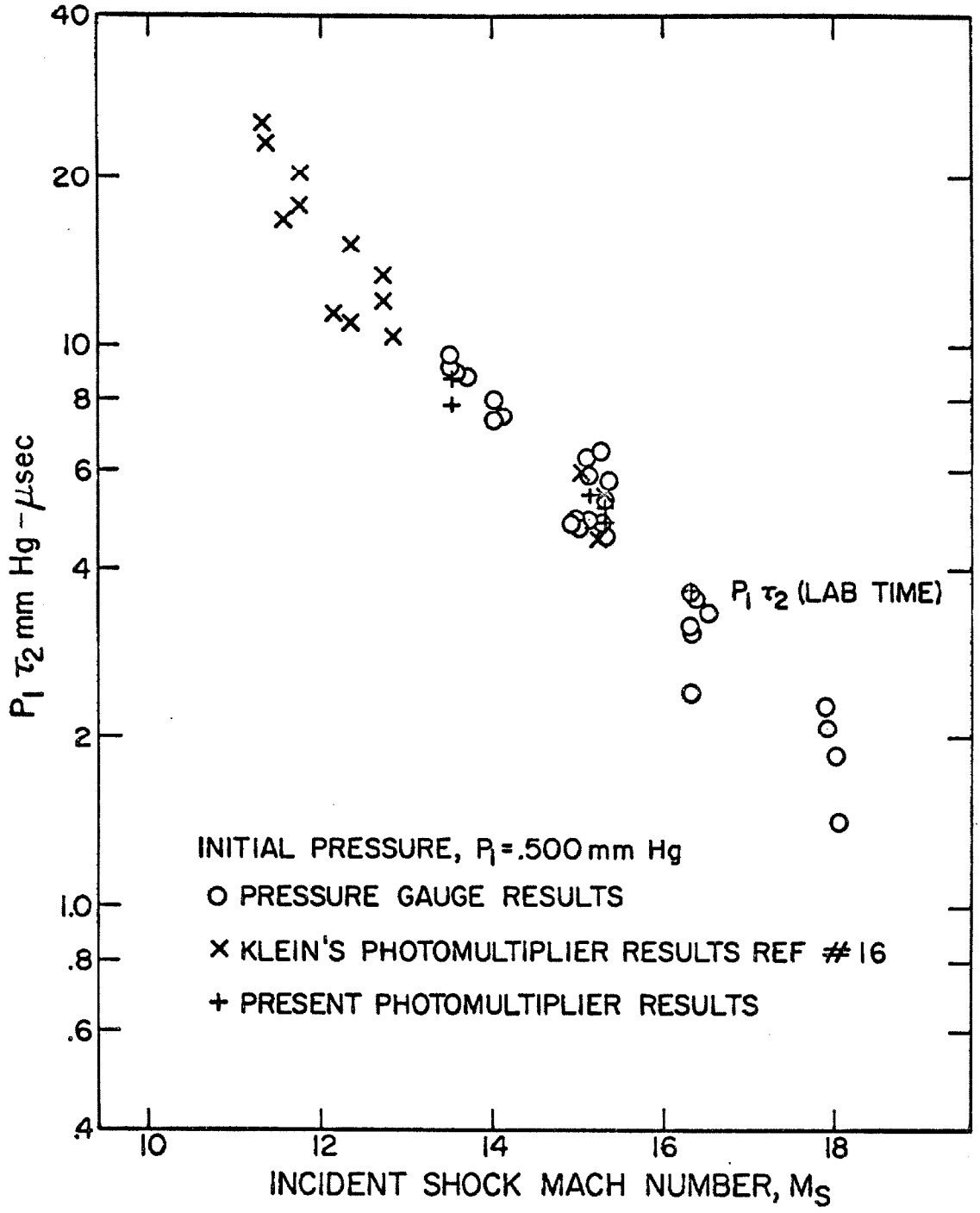

Figure 13 COMPARISON OF RELAXATION TIMES MEASURED WITH PHOTOMULTIPLIER AND WITH PRESSURE GAUGE

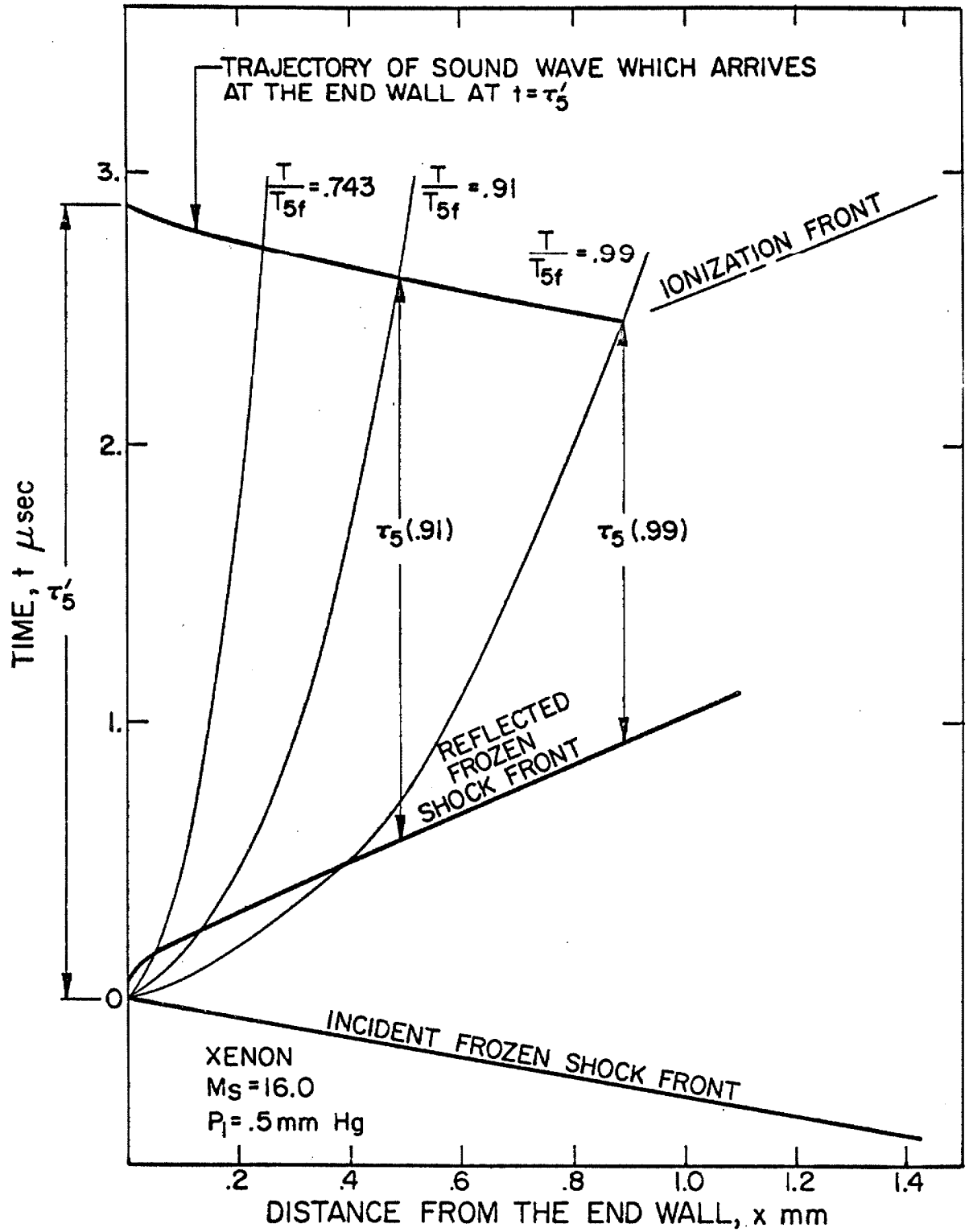

Figure 14 x–t DIAGRAM SHOWING THE EFFECT OF THE END WALL THERMAL LAYER ON THE MEASURED RELAXATION TIME τ_5'

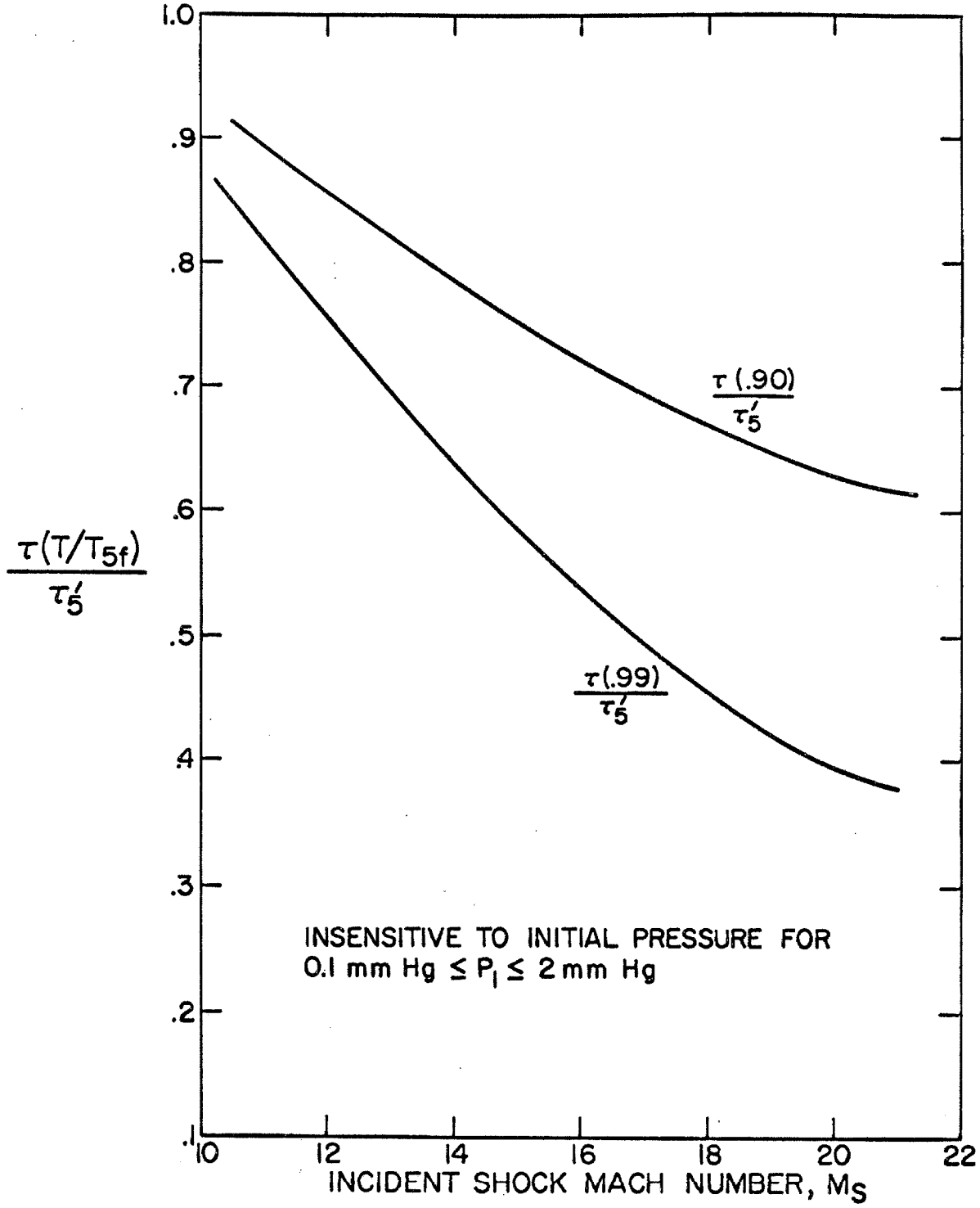

Figure 15 REDUCTION FACTOR FOR MEASURED RELAXATION TIME, τ_5', DUE TO END WALL THERMAL LAYER

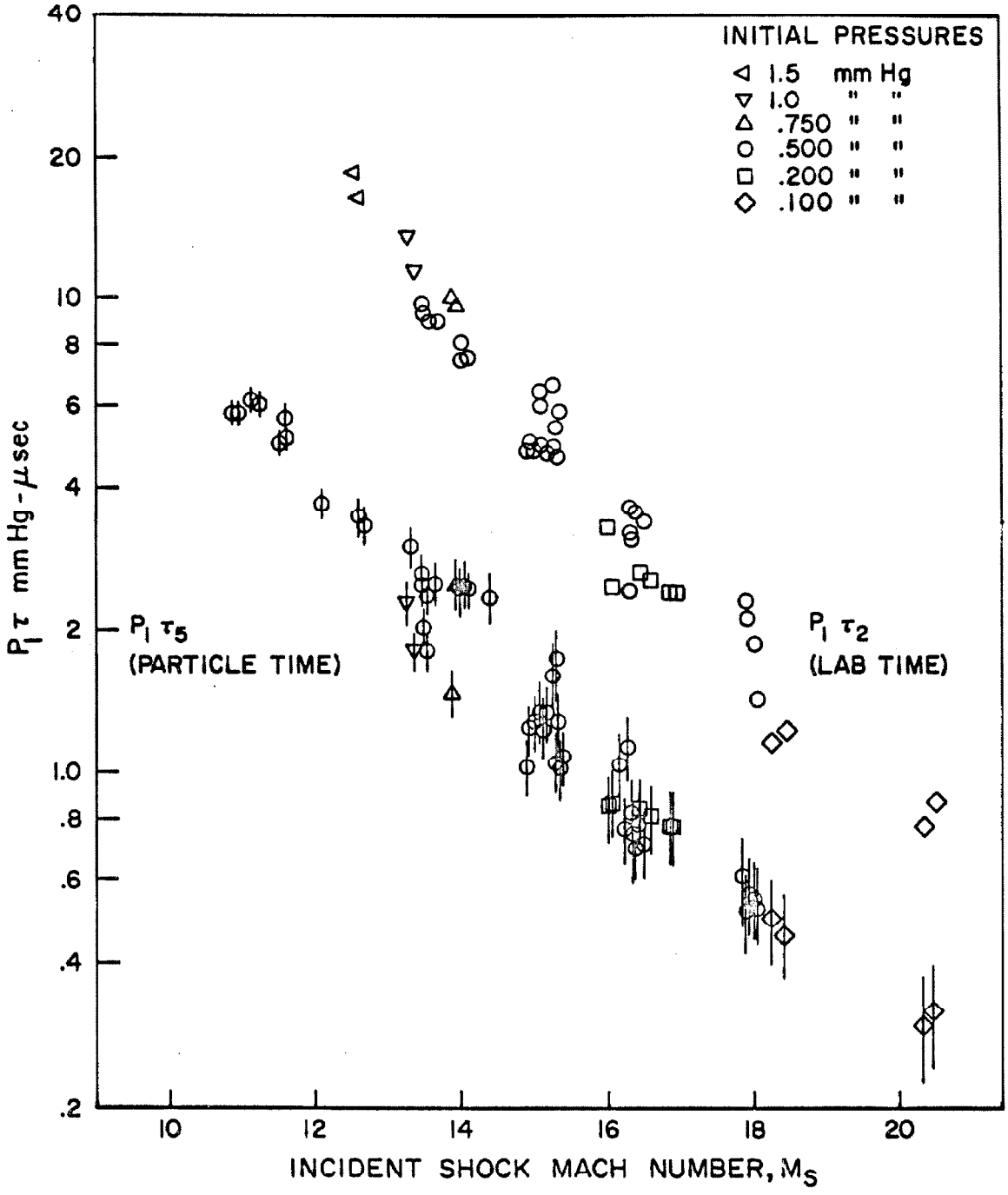

Figure16 SUMMARY IONIZATION RELAXATION TIME DATA FOR XENON

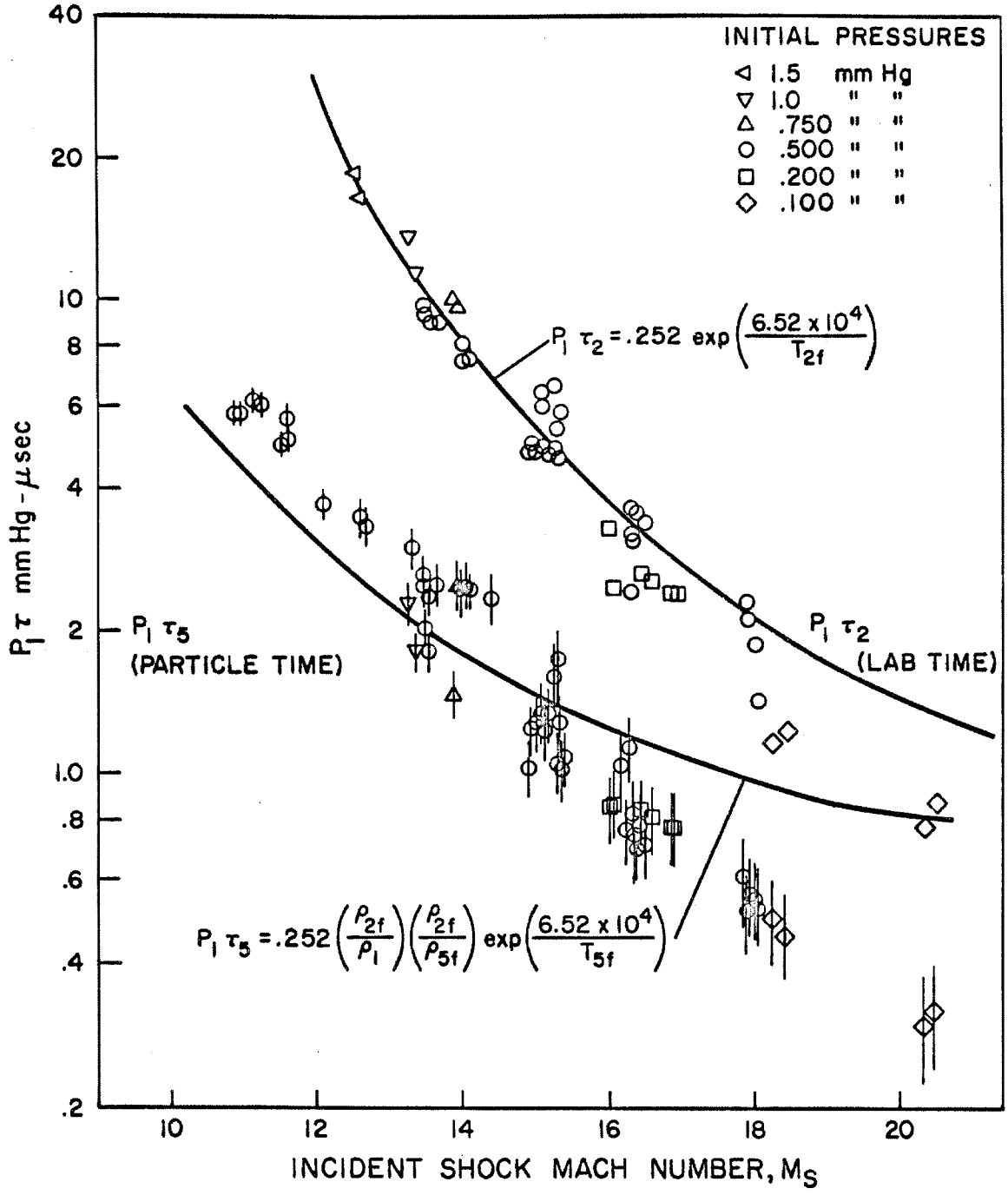

Figure 17 COMPARISON BETWEEN EXPERIMENTAL RESULTS AND PREDICTED VALUES OF $P_1 \tau_5$ USING EQUATION 4

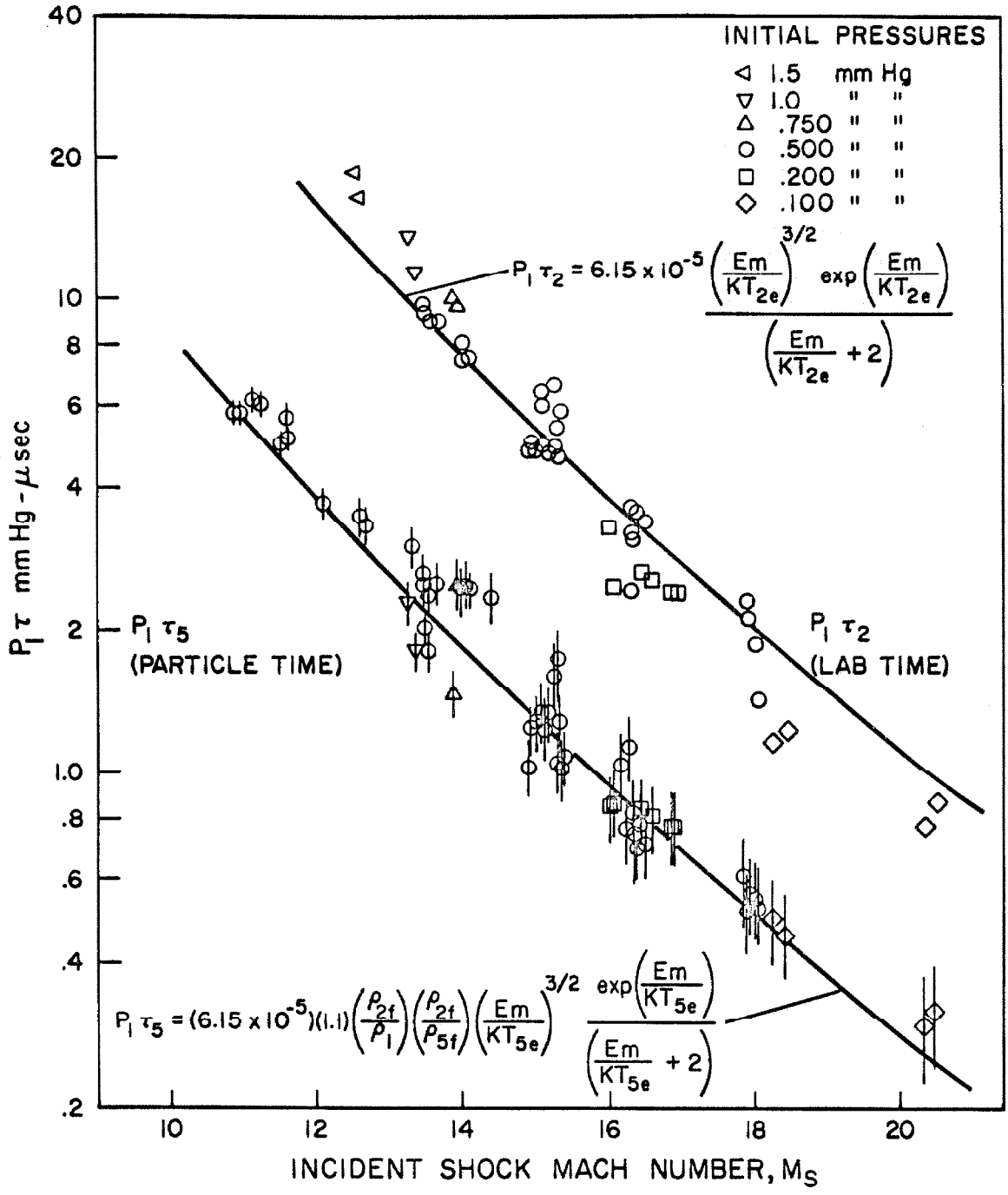

Figure 18 COMPARISON BETWEEN EXPERIMENTAL RESULTS AND PREDICTED VALUES OF $P_1\tau_5$ USING EQUATION 12

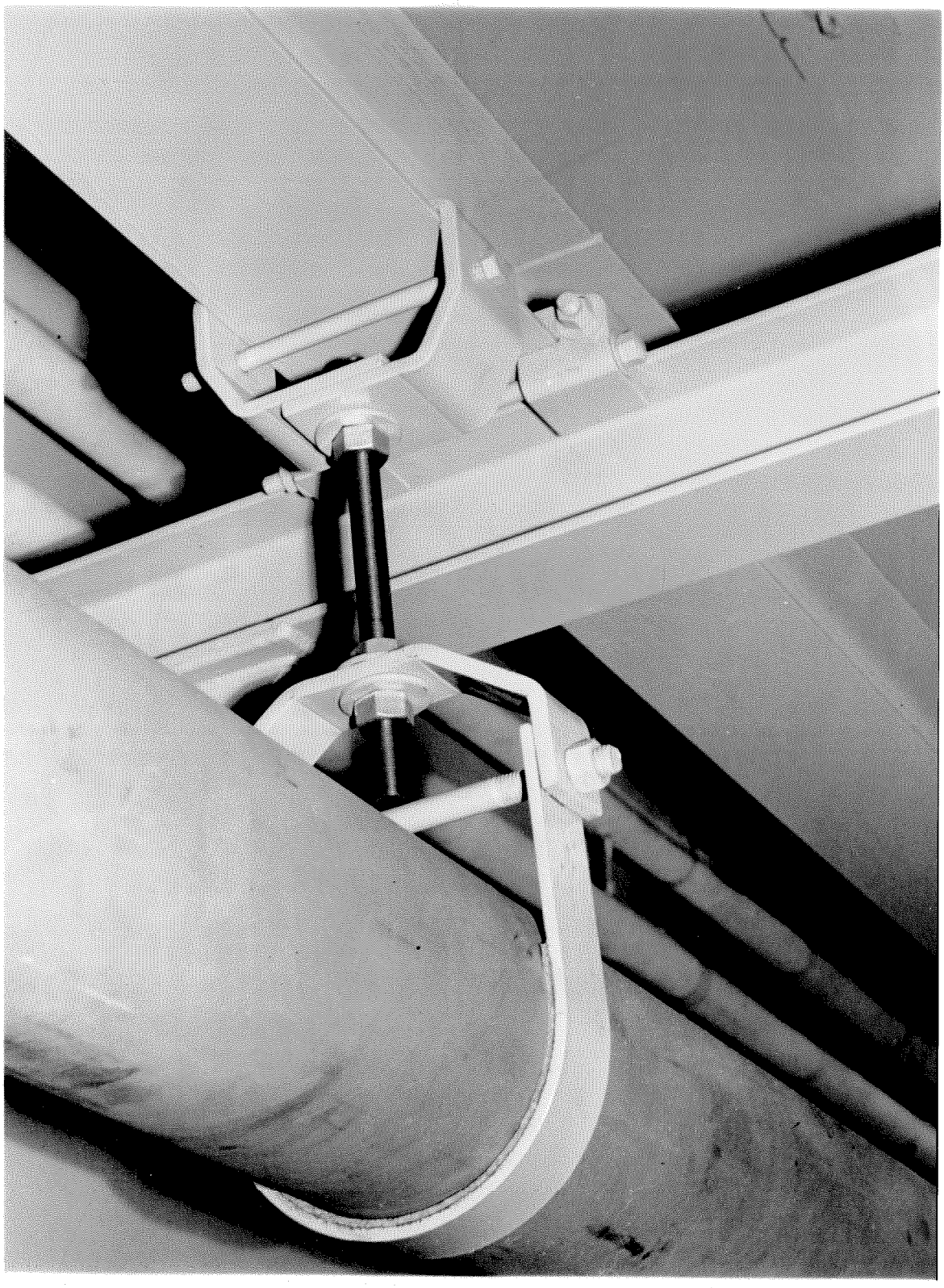

Figure 19 TYPICAL PIPE CLEVIS HANGER ASSEMBLY

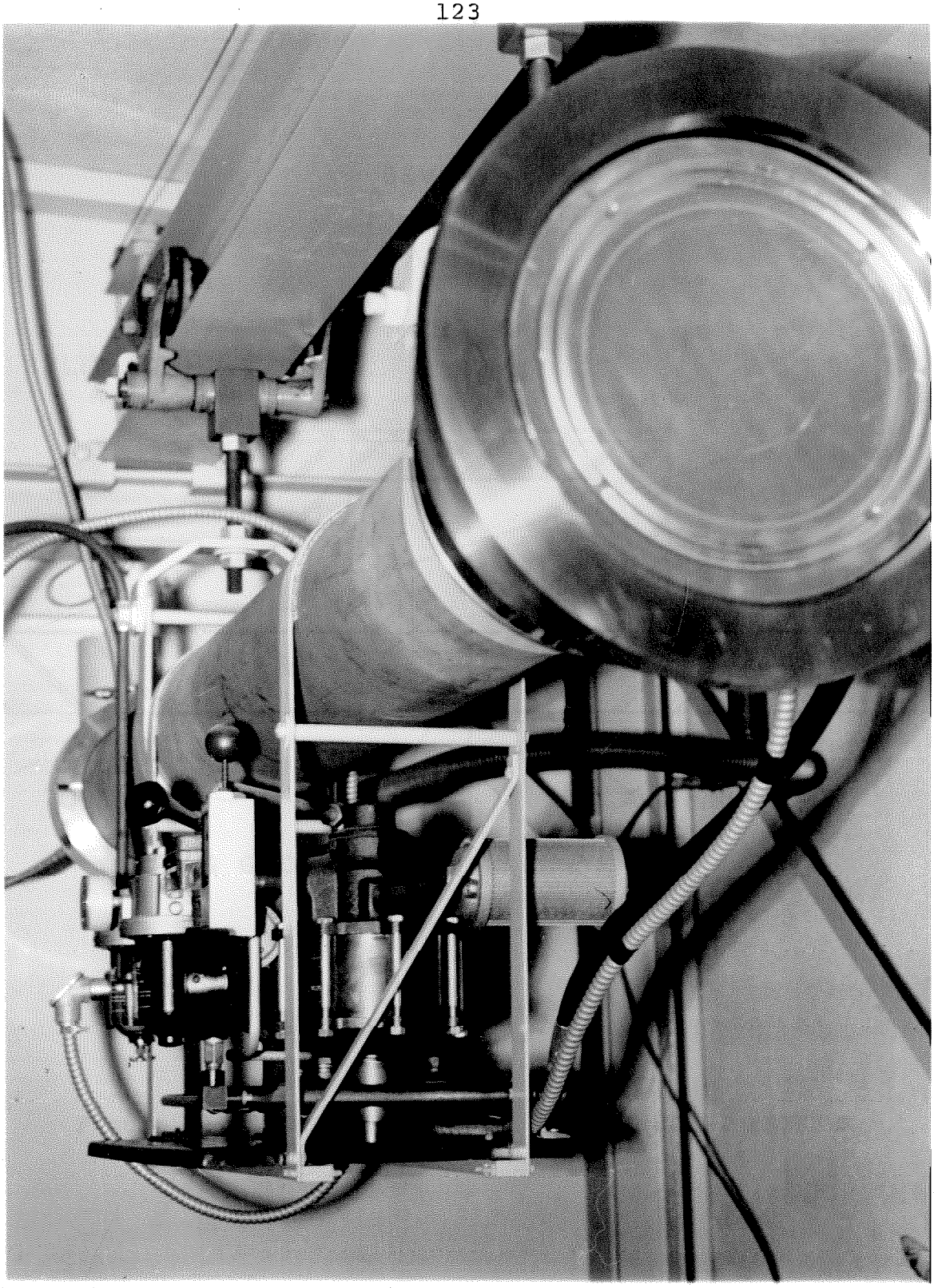

Figure 20 DRIVER SECTION AND HYDRAULIC PUMP ASSEMBLY

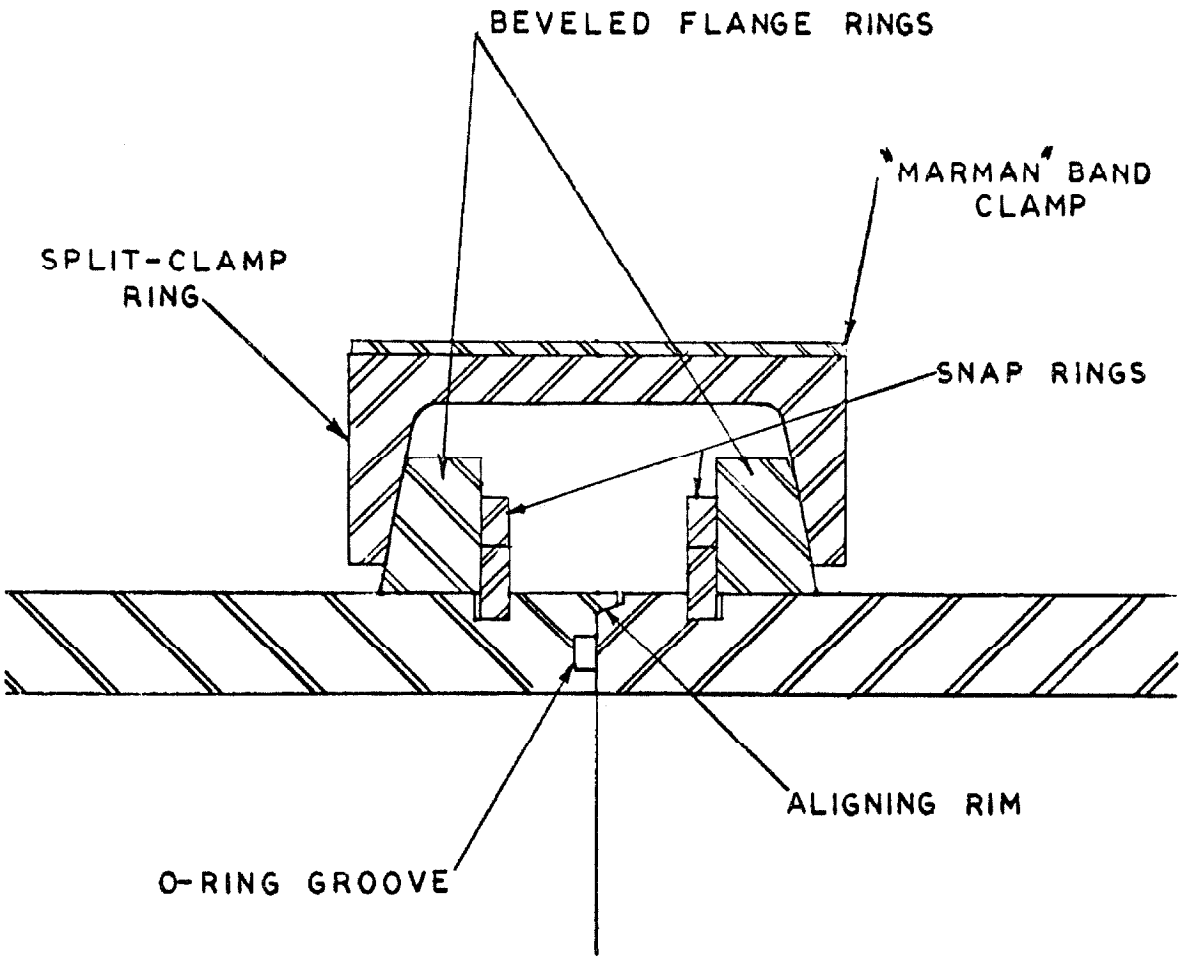

Figure 21 SECTIONAL VIEW OF TYPICAL JOINT BETWEEN TWO SHOCK TUBE SECTIONS

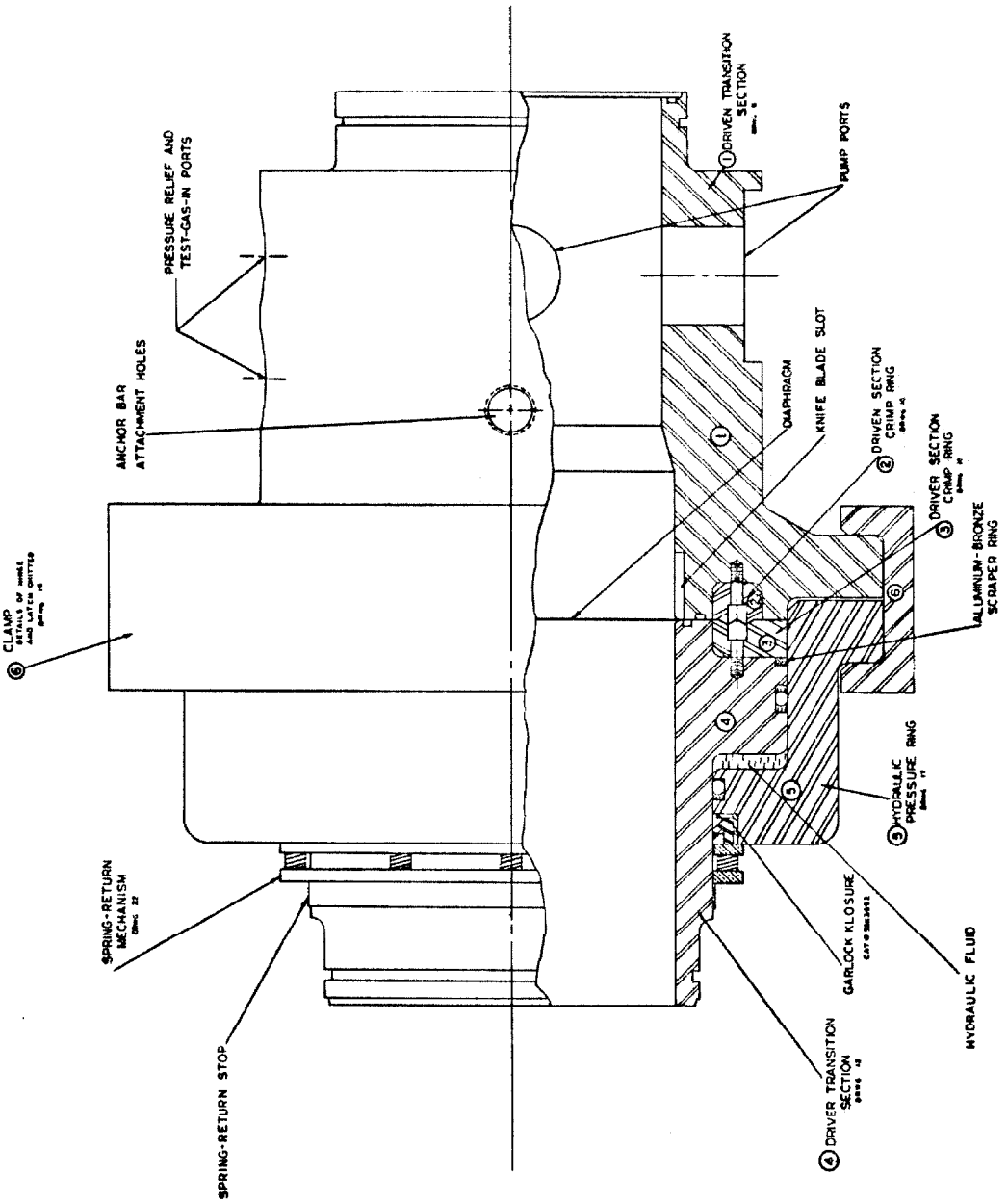

Figure 22 DIAPHRAGM-TRANSITION SECTION ASSEMBLY

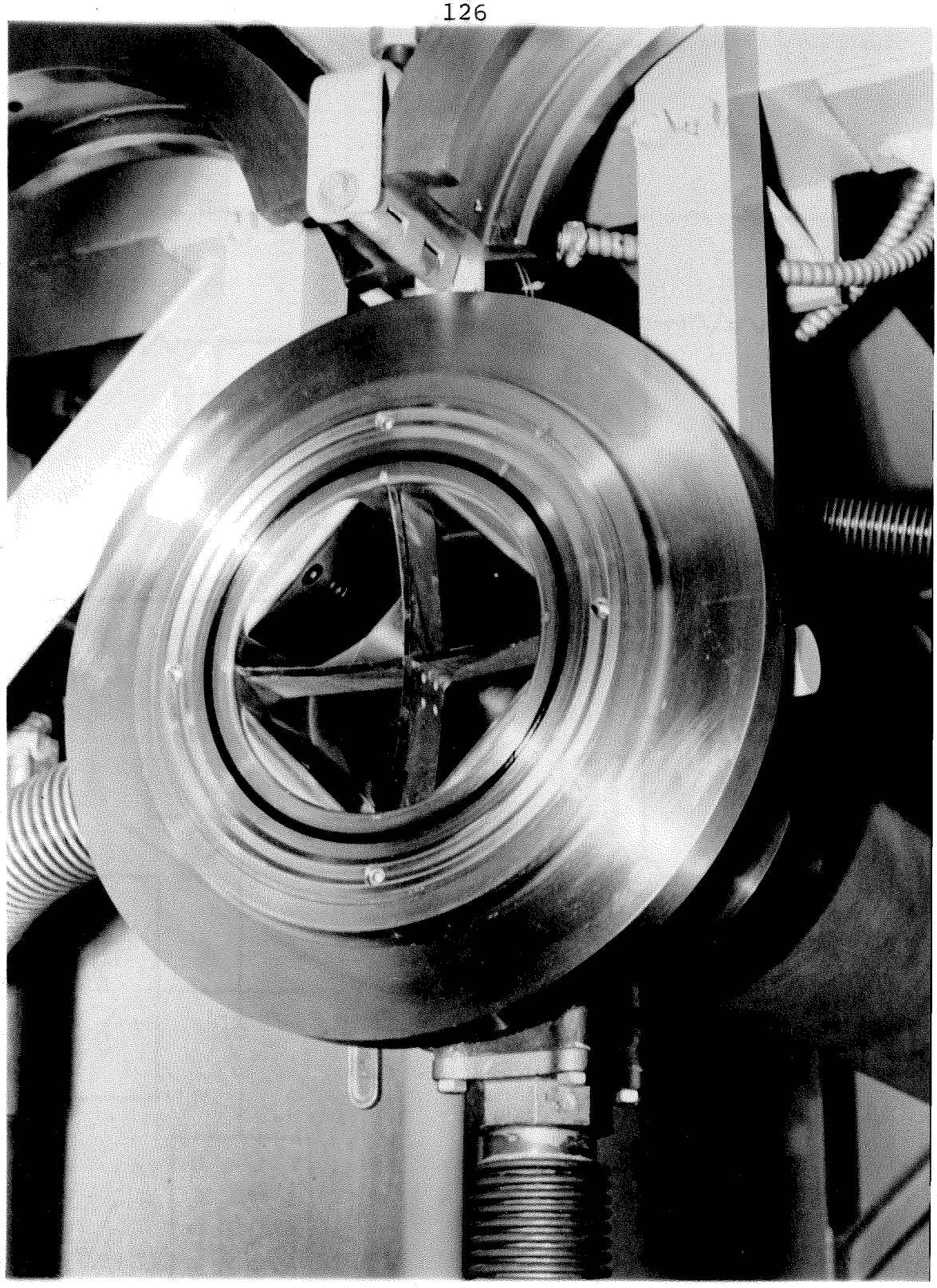

Figure 23 END VIEW OF DRIVEN TRANSITION SECTION SHOWING KNIFE BLADES, SQUARING PLATES AND CLAMP

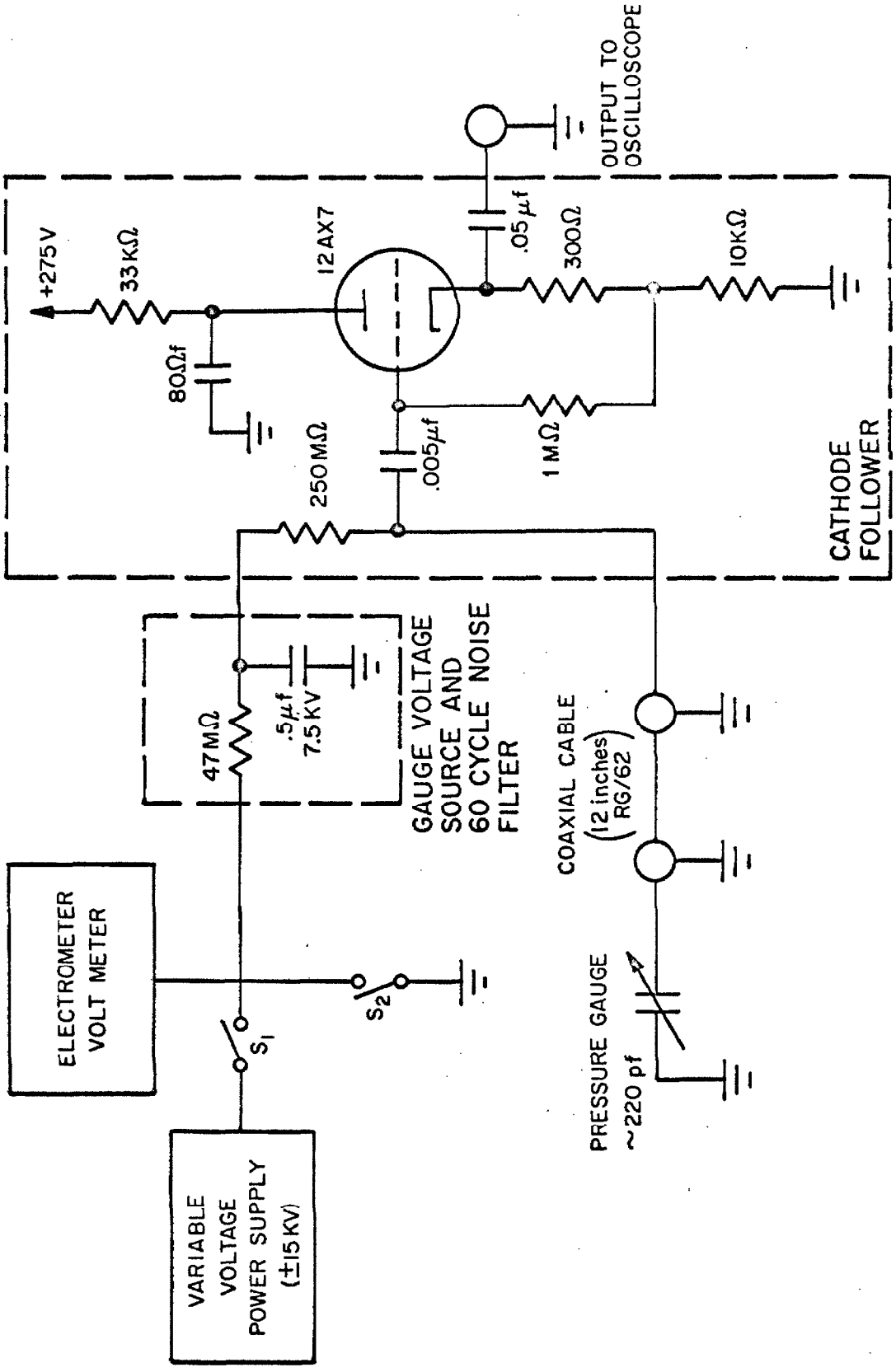

Figure 24 PRESSURE GAUGE CIRCUIT

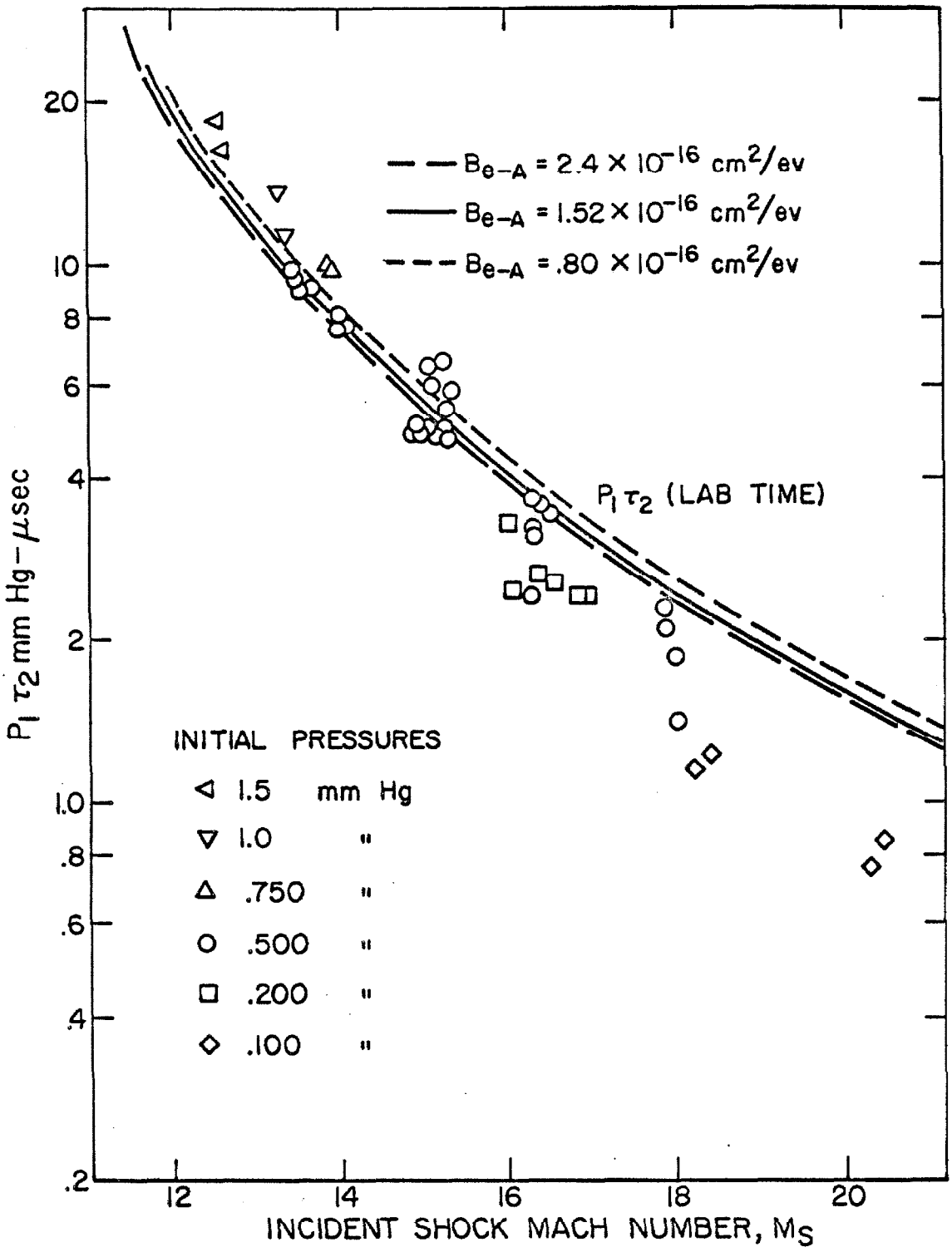

Figure 25 THE EFFECT OF VARYING THE ELECTRON-ATOM INELASTIC CROSS SECTION ON PREDICTING THE RELAXATION TIME τ_2 IN XENON

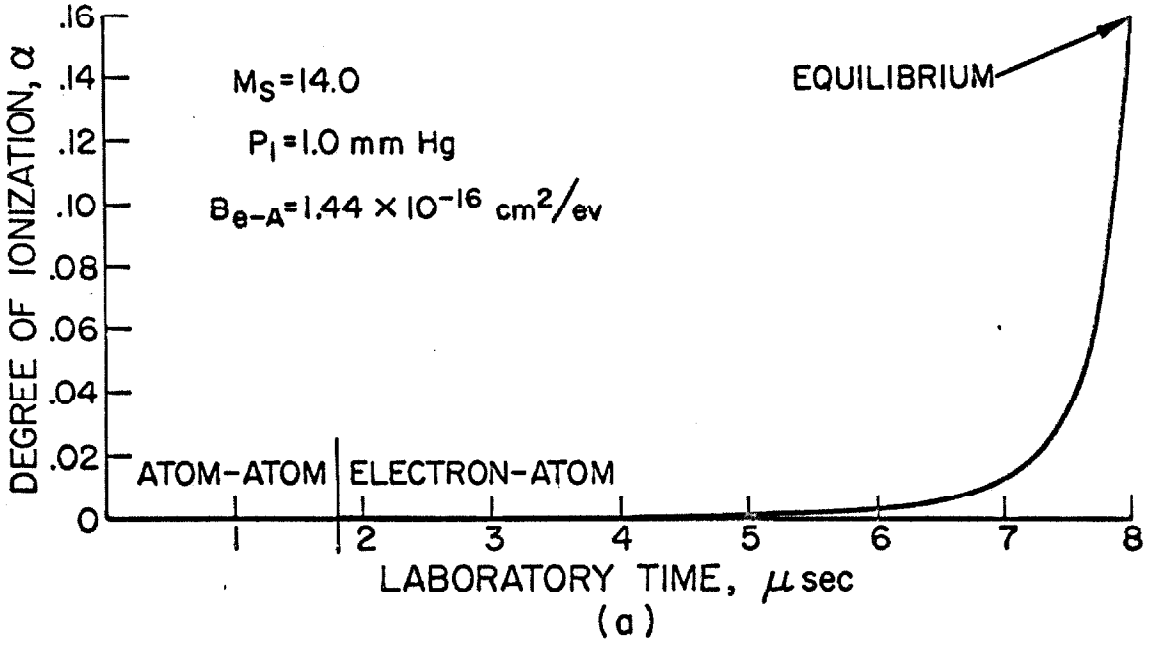

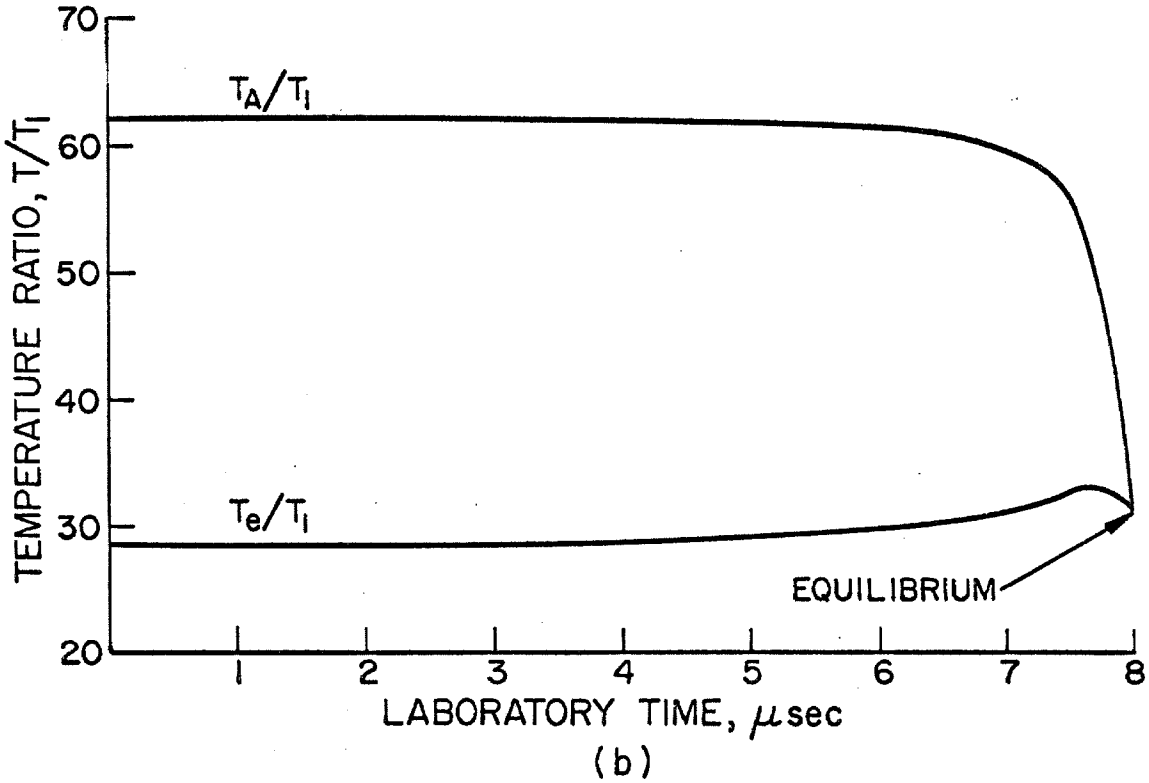

Figure 26 CALCULATED DEGREE OF IONIZATION AND TEMPERATURE PROFILES FOR THE INCIDENT SHOCK STRUCTURE IN XENON